GAS EVOLUTION AND GAS-LIQUID SEPARATOR MODELING

By

ALDEN BRACK DANIEL

Bachelor of Science in Chemical Engineering
Florida State University
Tallahassee, FL
2013

Submitted to the Faculty of the
Graduate College of the
Oklahoma State University
in partial fulfillment of
the requirements for
the Degree of
DOCTOR OF PHILOSOPHY
December, 2018

GAS EVOLUTION AND GAS-LIQUID

SEPARATOR MODELING

Dissertation Approved:

Dr. Clint P. Aichele

Dissertation Advisor

Dr. James R. Whiteley

Prof. Robert J. Agnew

Dr. David M. Lavenson

ACKNOWLEDGMENTS

I would like to thank my advisor, Dr. Clint Aichele, for his insight and guidance throughout my time at Oklahoma State University. I am also grateful for the sage council provided by my committee chair, Dr. Rob Whiteley. Additionally, I would like to thank my other committee members, Dr. David Lavenson and Prof. Rob Agnew, for their continual support and advice. I would like to express my gratitude to Dr. Sayeed Mohammad and Dr. Michael Miranda for their assistance throughout my research project. I would also like to thank Dr. Aniruddha Kelkar for his unique modeling insights and Dr. Gene Kouba for his support and guidance.

I am grateful for our industrial collaborations sponsoring my research. Financial support was initially provided by Chevron Energy Technology Company. In 2017, the Fluid Phase Kinetics (FPK) Joint Industry Project was founded at Oklahoma State University which continued funding for my research. Member companies include Chevron Energy Technology Company, ExxonMobil Upstream Research Company, and Anadarko Petroleum Corporation.

Finally, I would like to thank my family. My mother and father have been a great source of support throughout the years. They are responsible for catalyzing my interest in the sciences in the first place. My brother, Conner, has served as a continual source of inspiration. Most of all, I would like to thank my ever-supportive wife, Rhea. Without her love and encouragement, this work would not have been possible.

Acknowledgments reflect the views of the author and are not endorsed by committee members or Oklahoma State University.

Name: ALDEN BRACK DANIEL

Date of Degree: DECEMBER, 2018

Title of Study: GAS EVOLUTION AND GAS-LIQUID SEPARATOR MODELING

Major Field: CHEMICAL ENGINEERING

Abstract: Gas-liquid separation is a critical unit operation for oil and gas production. While there has been a large number of studies investigating the removal of liquid droplets from the gas phase, relatively little attention has been paid to the separation of gas bubbles from the liquid phase. Understanding the liquid degassing process is critical as oil and gas production is pushed towards more extreme operating conditions, particularly those involving heavy oil and high pressure environments. Current degassing guidelines rely on overly simplistic assumptions and field experience. Additionally, the entering gas and liquid phases are assumed to be in thermodynamic equilibrium with one another. Any pressure drop experienced by the multiphase stream prior to entering the separator will result in excess solution gas evolving out of solution. If the separator liquid residence time is less than the time required to re-establish equilibrium, the exiting liquid stream will then contain excess dissolved gas that will evolve out of solution further downstream. The aim of this study was twofold: construct a new experiment capable of measuring gas evolution at high pressures and develop a modeling framework for degassing within a horizontal gas-liquid separator incorporating the experimental gas evolution findings. A reference hydrocarbon system of methane and n-dodecane was used for the gas evolution experiments. Both rates of absorption and desorption were measured using the same process conditions, confirming that both mass transfer coefficients were symmetric within the experimental error. The surface renewal theory in the form of the small eddy model was found fit the data with an average error of 12.3 %. Using the separator degassing model, separation performance of entrained gas was found to be driven primarily by the liquid viscosity as well as the overall size of the initial bubble distribution. New entrained gas separation guidelines were developed using the separator model. Removing significant amounts of excess solution gas was found to be challenging using inlet conditions that also favored entrained gas separation. As more bubbles are separated from the liquid, the interfacial area available for mass transfer along with the net mass transfer rate also decrease.

TABLE OF CONTENTS

Chapter Page

Chapter Page

Chapter Page

LIST OF TABLES

Table Page

LIST OF FIGURES

Figure Page

Figure Page

Figure Page

Figure Page

Figure Page

NOMENCLATURE

A ..... Surface area [m^2]
a ..... Volumetric interfacial area [m^2/m^3]
C ..... Concentration [mol/L]
C_D ..... Drag coefficient
D ..... Diffusion coefficient [m^2/s]
d ..... Diameter [m]
d_e/d_h .... Bubble shape factor
f ..... Frequency [1/s]
g ..... Gravitational acceleration [m/s^2]
H ..... Henry's law constant [Pa]
h ..... Height [m]
J ..... Flux [$mol/(m^2 \cdot s)$]
k ..... Mass transfer constant [m/s]
K_s ..... Souders-Brown coefficient [m/s]
L ..... Length [m]
M ..... Morton number
MW .... Molecular weight [g/mol]
N ..... Number frequency
n ..... Moles [mol]
N_p ..... Power number
P ..... Pressure [Pa]
p ..... Partial pressure [MPa]
P_d ..... Probability density
Q ..... Volumetric flow rate [m^3/s]
R ..... Ideal gas constant [$J/(mol \cdot K)$]
r ..... Radius [m]
Re ..... Reynolds number
Sc ..... Schmidt number
SG ..... Specific gravity
Sh ..... Sherwood number
T ..... Temperature [K]
t ..... Time [s]
Ta ..... Tadaki number

V ..... Volume [m^3]
v ..... Velocity [m/s]
W ..... Work [J]
x ..... Mole fraction
x_{eg} ..... Entrained gas fraction

Subscripts/Superscripts
$*$ ..... Equilibrium condition
0 ..... Initial condition
ave ..... Average
b ..... Bulk
c ..... Critical value
g ..... Gas phase
i ..... Vertical vessel indexing (through space)
int ..... Interface
j ..... Horizontal vessel indexing (through time)
k ..... Element-wise indexing for a given (i, j) position
l ..... Liquid phase
m ..... Mode
r ..... Residence
s ..... Stirred tank
σ ..... Variability
t ..... Terminal settling
ves ..... Vessel

Greek Symbols
δ ..... Film thickness [m]
ϵ ..... Energy dissipation rate [m^2/s^3]
μ ..... Dynamic viscosity [$Pa \cdot s$]
ν ..... Kinematic viscosity [m^2/s]
ω ..... Mixing speed [s^{-1}]
ρ ..... Density [kg/m^3]
σ ..... Surface tension [N/m]
θ ..... Angle [rad]
ξ ..... Supersaturation ratio

CHAPTER I

INTRODUCTION

1.1 Gas-Liquid Separation

Gas-liquid separation is a critical unit operation in crude oil production. Flow from a petroleum reservoir results in a complex mixture of gases and liquids with a range of different physical properties. Typically, in upstream oil and gas operations, the gases and liquids in the multiphase stream must be first separated from one another before any additional processing can be done. Separating these multiphase fluids present numerous challenges, where any issues in design and operation of the separators creates bottlenecks requiring equipment adjustments downstream. These alterations add operating costs, increase downtime and/or reduced throughput, all of which result in lost value. Properly designing separators in the first place is of great importance since the cost of making repairs to a poorly functioning separator can often far exceed the initial cost of the separator itself (Bymaster et al., 2011).

Gas-liquid separators are tasked with separating both gases from the liquids and liquids from the gases. Poor phase separation can thus be classified into two distinct categories. Liquid droplets present in the exiting gas stream is termed liquid carry-over (LCO). On the other hand, gas bubbles present in the exiting liquid stream is known as gas carry-under (GCU) (Lavenson et al., 2016). A properly designed gas-liquid separator will ensure adequate separation of both gas and liquid phases while minimizing the total size requirement of the separator itself. An example of poor phase separation, specifically gas carry-under, can be seen in Figure 1.1. If the entering multiphase stream is not given enough time within the separator, the

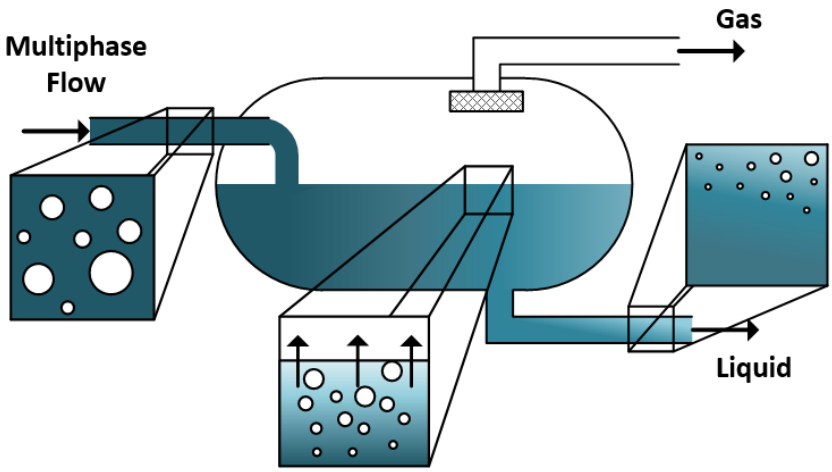

Figure 1.1: Example of gas carry-under in a horizontal separator

entrained gas phase in the liquid will not sufficiently separate. The resulting flow through the liquid outlet will then contain undesirable gas bubbles.

1.1.1 Challenges in Gas-Liquid Separation

As oil exploration and production ventures into more extreme conditions, gas-liquid separation is made more challenging. New developments in subsea processing, heavy oil production, and high-pressure separation require a more thorough understanding of how this separation process occurs.

Subsea processing refers to the active handling and treatment of produced fluids at the seabed (McClimans et al., 2006; Fantoft et al., 2004). The aspects of subsea processing that have received the most attention for their potential value proposition include: multiphase boosting, liquid pumping, gas compression, and gas-liquid separation. By performing the fluid processing at the seabed instead of on an offshore platform, operating costs from pumping and/or compressing can be saved. Performing the gas-liquid separation at subsea conditions also has the potential to mitigate the risk of hydrate formation by avoiding the thermodynamic envelope where they may be formed (Di Silvestro et al., 2011). The rigors of technical designs required

to capture these opportunities necessitate a quantitative understanding of each subsea unit operation. Gas-liquid separation is one of the first bottlenecks in subsea processing and merits a critical assessment.

Increasingly, compact separation technologies are seen as the most viable solution for subsea separation. The smaller design reduces manufacturing, transportation, and installation costs (Baker et al., 1990; Bymaster et al., 2011; Gomez et al., 1999; Kristiansen et al., 2016; Rosa et al., 2001). Conventional separation vessels must be made thicker and heavier in order to sustain subsea pressures, while installation and loading requirements dictate further limitations on size and weight. The retrievability of the unit becomes a large concern as well. For example, the first subsea separation unit for water reinjection placed at the Troll oil field in the North Sea was so large that retrieving the unit in the case of malfunction would not be possible (Horn et al., 2003). While these concerns may not completely disqualify a larger conventional design, the project economics may point more favorably towards smaller designs. Moreover, in typical offshore facilities, compact technologies are attractive due to minimal space requirements. Additionally, compact separators are also advantageous in retrofit applications. The lack of moving parts also adds to the simplicity of the design. The compact architecture results in reduced liquid residence times in the separator, thereby making it challenging to ensure that these separators meet specifications regarding gas carry-under with the liquids and liquid carry-over with the gas needed for safe downstream processing.

Heavy oil production represents another area where gas-liquid separation is being pushed to its extreme. Heavy oils are by definition highly viscous, typically defined as having an API gravity less than 20° (Zaba et al., 1988). Degassing these heavy oils has been shown to pose a larger challenge compared to conventional crude oils (Lavenson et al., 2016). Overly conservative separator designs can result in excessively large separator costs. Reducing the separator footprint and optimizing separators already

in place are key in order for heavy oil production to remain competitive.

1.1.2 Gaps in Current Understanding

While gas-liquid separation is considered a mature technology in many realms, there are still important unanswered questions regarding the performance of separators. There has been substantial work to understand how liquid carry-over affects separation performance and how these concerns can be addressed and modeled (Chirinos et al., n.d.; Mantilla, 2008; Paras and Karabelas, 1991; Viles, 1993). Gas carry-under, however, has been largely neglected in the literature, though the consequences downstream are no less important than those related to liquid carry-over.

Traditionally, sizing gas-liquid separators requires the use of either the Souders-Brown approach or droplet settling theory to ensure that droplets present in the overhead gas phase have sufficient time to settle within the limits of a separators residence time, thus minimizing liquid carry-over (Bothamley, 2013*a*,*b*,*c*). Designing separators to minimize gas carry-under, on the other hand, is largely left to simple rules of thumb and field experience. For example, the American Petroleum Institute's design criterion for gas-liquid separators, known as API 12J, recommends different liquid retention times based on the API gravity of the oil (API, 2009). These design guidelines can be seen in Table 1.1. Similar application-based approaches to separator retention time recommendations are also presented in the 12th edition of GPSA Engineering Data Book (GPSA, 2004), although these recommendations have been removed in the most recent edition (GPSA, 2016).

Table 1.1: API 12J degassing guidelines (API, 2009)

Oil Gravity [°API]	Retention Time [min]
35	1
20 – 30	1 – 2
10 – 20	2 – 4

While the above degassing recommendations may work for simple, well-understood

systems, these guidelines are much too simplistic for many cases, especially when performing separation with viscous oils. As liquid viscosities increase, bubble velocities decrease making it more challenging to achieve good separation and minimize gas carry-under. Traditionally, only entrained bubbles are considered as a source of gas carry-under; however in viscous systems, the role of solution gas potentially contributing to gas carry-under should also be considered (Lavenson et al., 2017).

Increased liquid viscosities are often associated with lower mass transfer coefficients (Lockemann and Schilünder, 1995; Song et al., 2014). If a viscous gas-liquid multiphase dispersion experiences a pressure drop prior to entering a gas-liquid separator, there is a possibility that mass transfer rates will not be fast enough for the fluid to attain equilibrium within the separator's residence time. As such, the solution exiting the liquid stream may still be supersaturated with gas. This excess dissolved gas will eventually evolve out of the liquid phase downstream of the separator and present itself as unexpected gas carry-under. The mass transfer due to excess solution gas is also known as gas evolution.

Gas evolution out of a supersaturated solution can significantly contribute to gas carry-under in gas-liquid separators if not properly accounted for. The problem of gas carry-under due to gas remaining dissolved in the liquid is expected to become magnified with either increasing liquid viscosities and/or smaller separator residence times. The higher the operational pressure of a gas-liquid separator, the more potential there is for the evolution of solution gas to become a problem. This is due to the fact that more gas is solubilized in the liquid as the pressure of the system increases. All gas-liquid separator design criteria to date, implicitly assume that the entering fluid is in equilibrium with the gas and the time required for separation is only needed to account for the rise of entrained bubbles out of the liquid.

There have been few studies investigating the rate of gas evolution out of hydrocarbon systems from a macroscopic perspective. Of the few studies found,

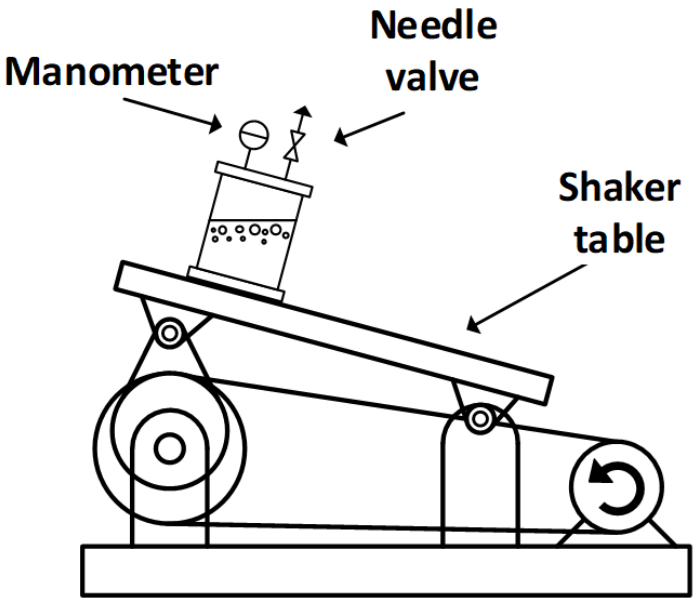

Figure 1.2: Schweitzer and Szebehely's experimental setup, adapted from Schweitzer and Szebehely (1950)

Schweitzer and Szebehely were the first to measure the rate of gas evolution out of liquids of different kinematic viscosities, including lubricating oils and other hydrocarbons (Schweitzer and Szebehely, 1950). Their experimental apparatus, shown in Figure 1.2, consisted simply of a pressure vessel mounted on a shaker table.

Starting with a saturated liquid at some initial saturation pressure, the overhead gas is slowly leaked out in order to avoid bubble nucleation before the supersaturated state is reached. Once the supersaturated solution is established, the container is closed and the shaker table is turned on. The agitated liquid disrupts the pseudo-equilibrium of the supersaturated solution. The gas then evolves out of solution and reestablishes a new equilibrium in the overhead volume. They measured pressure changes in the bulk vapor using a manometer connected to the overhead vapor space. As bubbles form in solution, the volume of the liquid phase increases, compressing the bulk vapor and thereby increasing pressure. Moreover, as the gas reaches the gas-liquid interface, it will add moles of gas to the overhead vapor space resulting in a pressure increase until a new equilibrium is established.

Schweitzer and Szebehely found that the time required for gas evolution increased roughly with increasing liquid kinematic viscosity (Schweitzer and Szebehely, 1950). While simple in design, the experiment suffered from several shortcomings. Gas evolution was performed at atmospheric pressure and neither the supersaturation ratio (i.e. driving force) or the gas-liquid interfacial area during the mixing were quantified. By only measuring the rate of pressure change and not accounting for how much gas was initially dissolved in solution, it is not possible to distinguish whether an increase or decrease in the gas evolution rate was due to an increased driving force or the different liquid properties mediating the rate of mass transfer. Finally, only air was used as the gas phase. The choice of the gas phase is important since different species have the potential to impact the rate of gas evolution one way or another.

Hunt also experimentally studied the evolution of gas out of hydrocarbon systems (Hunt, 1995). In her thesis work, Hunt used a custom piston rig to perform gas evolution tests in a manner similar to Schweitzer and Szebehely, though with a few key differences. A simplified schematic of the piston rig used in her studies can be seen in Figure 1.3. Instead of slowly depressurizing the liquid, followed by initiating the gas evolution with mechanical agitation, the piston is quickly drawn back using hydraulic fluid, simulating a more instantaneous pressure drop. The rapid change in pressure initiates the gas evolution and the pressure recovery back to equilibrium is recorded.

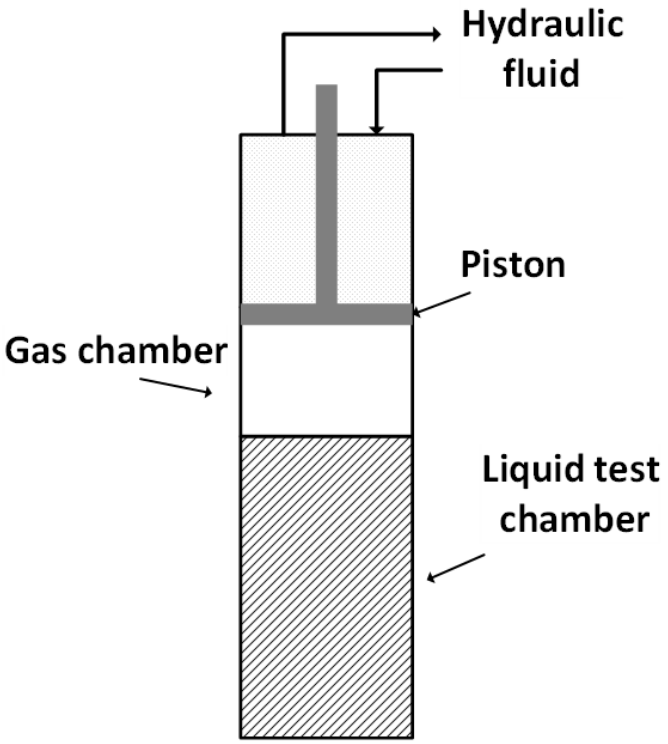

Figure 1.3: Simplified experimental diagram of Hunt's piston rig, adapted from Hunt (1995)

The advantage of using of a piston to perform the depressurization instead of allowing the gas to escape through a valve is that the experiment avoids having to deconvolute gas evolution from any transience associated with potential choked flow through a valve. The disadvantage, however, is that the maximum pressure the internal volume can withstand is limited by the piston's seal. While Hunt performed experiments using different hydrocarbon gases and liquids, fluid agitation within the vessel was only possible using pulsed liquid jets on the side of the vessel. Furthermore, the experiments were limited to a maximum pressure of 435 psia (3.0 MPa).

1.2 Research Goals

The primary goal of this research is to develop a new gas evolution experiment capable of measuring the rates of solution gas leaving a supersaturated solution at

high pressures and different rates of liquid mixing. The experiment must be capable of using hydrocarbons in both the gas and liquid phases. Using a reference hydrocarbon system of n-dodecane as the liquid phase and methane as the gas phase, a theoretical mass transfer model is validated for the system.

The second goal of this research is to use the experimentally validated mass transfer model and develop a horizontal separator modeling framework to allow for degassing predictions at different process conditions. The horizontal separator degassing model must allow for the prediction of gas carry-under due to both entrained gas and excess solution gas in the liquid inlet. Using the horizontal separator model, the effect of gas evolution on separation performance is evaluated.

1.3 Dissertation Organization

The first chapter in this dissertation provides the motivation for the study of gas evolution and its relation to separator degassing. Chapter 2 provides an overview of separator technology to date. Background of bubble dynamics and gas-liquid mass transfer are provided in Chapters 3 and 4, respectively. Chapter 5 goes over the gas evolution experimental development and gas evolution results are presented in Chapter 6. By further refining the experimental procedure, both rates of absorption and desorption are measured using a reference hydrocarbon system and presented in Chapter 7. The horizontal separator model development and results are presented in Chapter 8. Finally, the study conclusion and recommendations are summarized in Chapters 9 and 10.

CHAPTER II

GAS-LIQUID SEPARATORS

Gas-liquid separators are used to separate a multiphase stream into gaseous and liquid components. The separation process is two-fold: gases are separated from the liquids and liquids are separated from the gases. A well designed separator should be able to separate both phases from one another within the desired specifications. Gas-liquid separators are generally categorized as either two-phase or three-phase separators. Two-phase separators are responsible for separating a single gas phase from a single liquid phase. Three-phase separators, on the other hand, are tasked with separating a single gas phase as well as two immiscible liquids from one another. Within the oil and gas industry, three-phase separators are commonly used when an inlet stream consists significant amounts of gas, oil, and water.

If there is a high ratio of gases to liquids in the stream being separated, these separators are sometime called gas scrubbers. Gas-liquid separators are also referred to as traps when the fluid being handled comes directly from the wellhead. Other names for gas-liquid separators include: stage separator, knockout vessel, expansion vessel, amongst others (Lake and Arnold, 2007). Though the conditions under which separation is performed vary from one case to another, the general design considerations for these separators remains the same.

2.1 Conventional Gas-Liquid Separators

Conventional gas-liquid separators rely on gravity to separate phases of different densities. As the multiphase stream flows through the separator, buoyancy

propels bubbles of entrained gas towards the overhead gas phase while the weight of liquid droplets in the gas phase drives them towards the bulk liquid. With enough time, both phases will completely separate from one another.

Conventional separators generally contain three distinct sections responsible for the separation: an inlet conditioning section, gravity settling section, and a mist extraction section (Stewart and Arnold, 2008). The inlet conditioning section generally consists of a device placed at the separator inlet that preconditions the flow, often performing the bulk of the separation. The gravity settling section is required to allow both the gas and liquid phases to stratify as they flow through the separator. Here, the droplets fall out of the gas overhead and the entrained bubbles rise out of the bulk liquid. Prior to exiting the separator, the gas phase usually passes through a mist extraction section as well. The mist extractor is tasked with removing smaller droplets that did not have the chance to re-enter the liquid during its time in the gravity settling section (Arnold and Stewart, 1998). Gas-liquid separators are usually designed in three different configurations: horizontal, vertical and spherical.

2.1.1 Horizontal Separators

A schematic of a horizontal gas-liquid separator is presented in Figure 2.1. The multiphase stream enters the separator at the inlet and passes through the inlet conditioning device, shown here as a diverter plate. The stream flows through the gravity settling section where the liquid accumulates at the bottom and the gas at the top. Within this section, the liquid is given time to rid itself of any entrained or dissolved gas present within the liquid. This process is known as degassing. The time the overhead gas phase remains in the gravity settling section gives liquid droplets a chance to fall out of the gas stream. As it exits, the gas passes through the mist extractor. Mist extractors are usually composed of wire mesh, plates or vanes used to enhance coalescence of smaller droplets still present in the gas stream. Separators

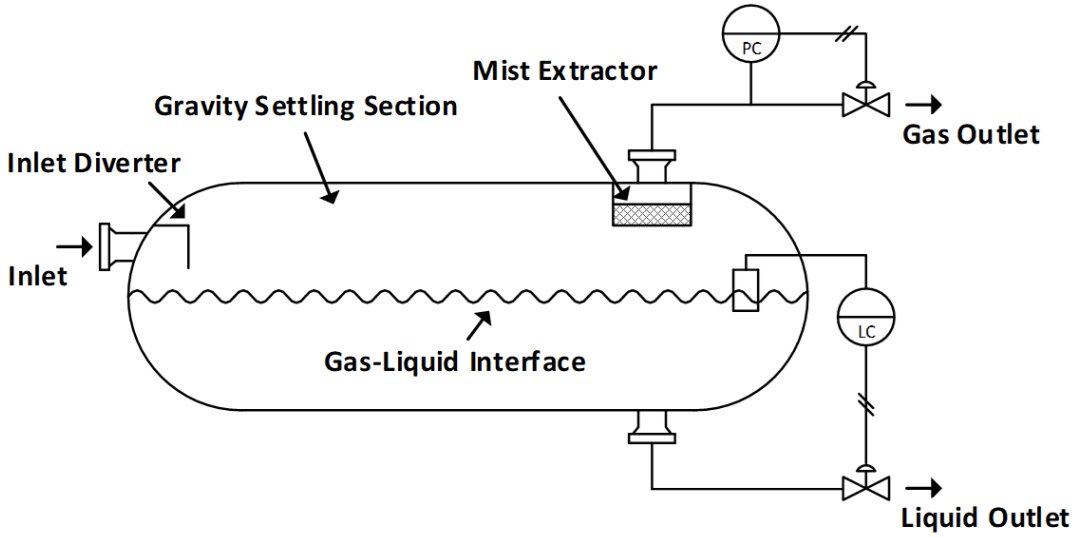

Figure 2.1: Schematic of a horizontal separator, adapted from Stewart and Arnold (2008)

will usually have a liquid level control, shown in the figure as LC. The level control regulates the exiting liquid flow rate to maintain a stable liquid level within the separator. Also, the pressure controller, shown in the figure as PC, regulates the exiting gas flow rate to maintain a constant pressure within the vessel.

2.1.2 Vertical Separators

Vertical separators usually contain the same internals as the horizontal separator, but are instead positioned vertically as the name implies. An example schematic of a vertical gas-liquid separator is shown in Figure 2.2. Similar to the horizontal separator, the multiphase stream enters through the inlet and passes through the inlet conditioning device. The liquid flows downwards towards the exit at the bottom of the separator while the gas exits through the top. The gas exits through the mist extractor to remove droplets too small to be separated from the overhead gas phase while in the gravity settling section. As with the horizontal separator, vertical separators usually have liquid level and pressure controls that regulate the liquid and gas flow rates, respectively. The main difference between horizontal and vertical

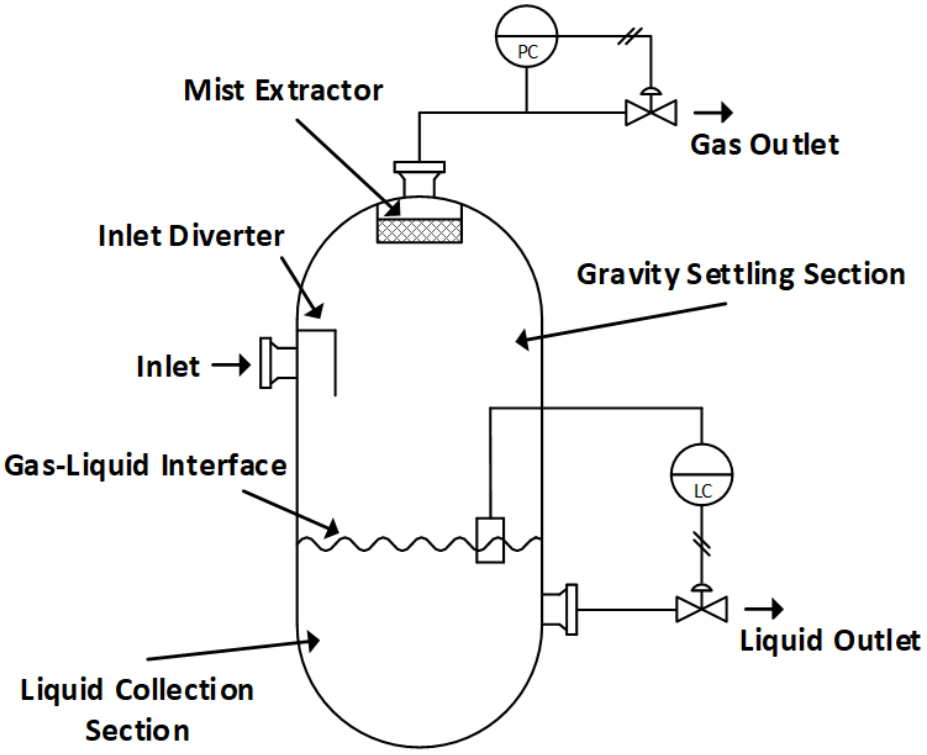

Figure 2.2: Schematic of a vertical separator, adapted from Stewart and Arnold (2008)

separators is how the bulk liquid flows relative to the entrained gas. Within horizontal separators, the liquid flow is normal to the direction of the entrained gas flow. Vertical separators, on the other hand, require that any entrained gas flows against the downward flow of the liquid. This makes liquid degassing more challenging in a vertical separator than what it would otherwise be in a horizontal separator.

2.1.3 Spherical Separators

Spherical separators, an example of which is shown in Figure 2.3, are less common than either horizontal or vertical separators. As name implies, the spherical separator is contained within a sphere. In essence, a spherical separator is a vertical separator that has been shrunk down so that there are no vertical walls left within the design, only the end caps. Within this design, the multiphase inlet enters through the top of the separator and is diverted to the sides of the vessel by a dished head.

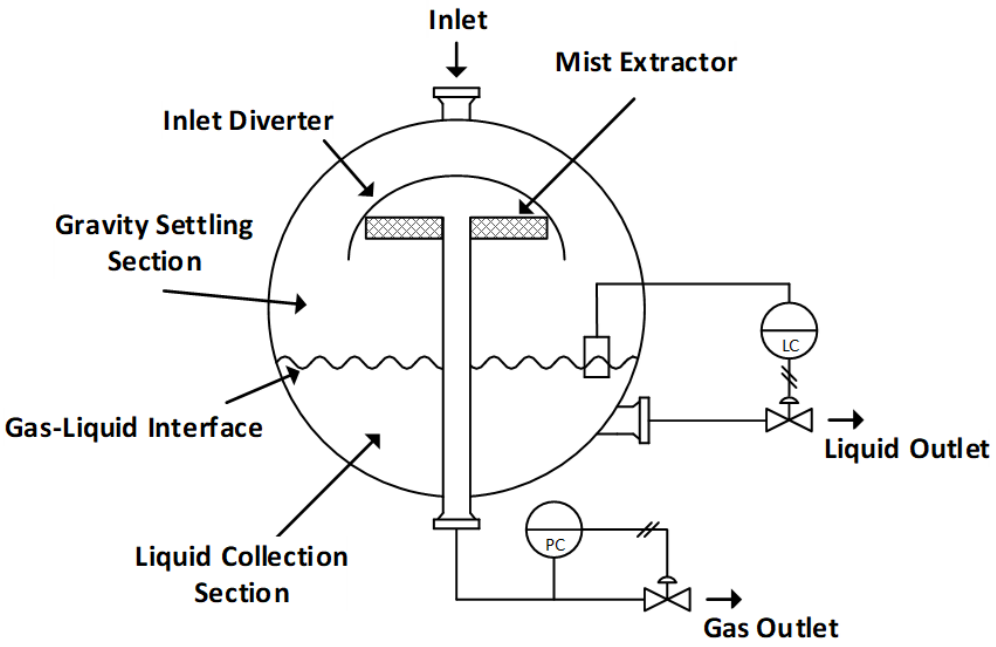

Figure 2.3: Schematic of a spherical separator, adapted from Stewart and Arnold (2008)

As the liquid collects within the liquid collection section, the bulk phases separate and the liquid stream exits through an opening in the separator's side below the gas-liquid interface. The gas being separated from the liquid exits the separator through the mist extractor then subsequently through the gas outlet down the middle of the separator.

The rationale for designing gas-liquid separators as a sphere stems from the fact that spheres are the most efficient method of containing pressure. In theory, spherical separators were designed to take advantage of the best characteristics of both horizontal and vertical separators, however in practice they exhibit some of the worst separation performance (Stewart and Arnold, 2008). Spherical separators also have very limited surge capacity and are difficult to both size and operate. As such, spherical separators will not be further considered here.

2.1.4 Separator Selection

The process of selecting between a horizontal and vertical separator for a given application requires an understanding of the benefits and drawbacks offered by each design. As a general rule of thumb, vertical separators are usually used when the gas-liquid ratio is high while horizontal separators are used when the gas-liquid ratio is low, though there are many other design considerations that must be accounted for.

Horizontal separators are generally acknowledged to have better separation properties compared to vertical separators (Lake and Arnold, 2007). In a horizontal separator, the flow direction of the phase being separated (either liquid droplets in the gas phase or gas bubbles in the liquid phase) is not countercurrent to the flow of the bulk phase outlet. Liquid droplets fall perpendicular to the bulk gas phase flow while the bubbles rise perpendicular to the liquid flow. This means that the net velocity of the phase being separated is not metered by the flow of the bulk phase exiting the separator. Horizontal separators are also best suited for liquid-liquid separation where the liquid phase is further split into two different streams.

Potentially foaming liquids are best handled by a horizontal separator. As the liquid flows through a horizontal separator, the bulk phases are allowed to stratify physically within that space. Any foam generated at the inlet of the horizontal separator will also have the separator's liquid residence time to decay and hopefully completely dissipate. Since new interfacial area between the bulk gas and liquid phases in a vertical separator is not generated as the liquid flows through the vessel, any foam formation at the vessel's inlet has a much higher chance of accumulating and potentially interfering with the separation performance.

Vertical separators, on the other hand, are best suited when the overall liquid flow is low. Vertical separators occupy less plan area than what an equivalent horizontal separator would require. This aspect is especially important in situations

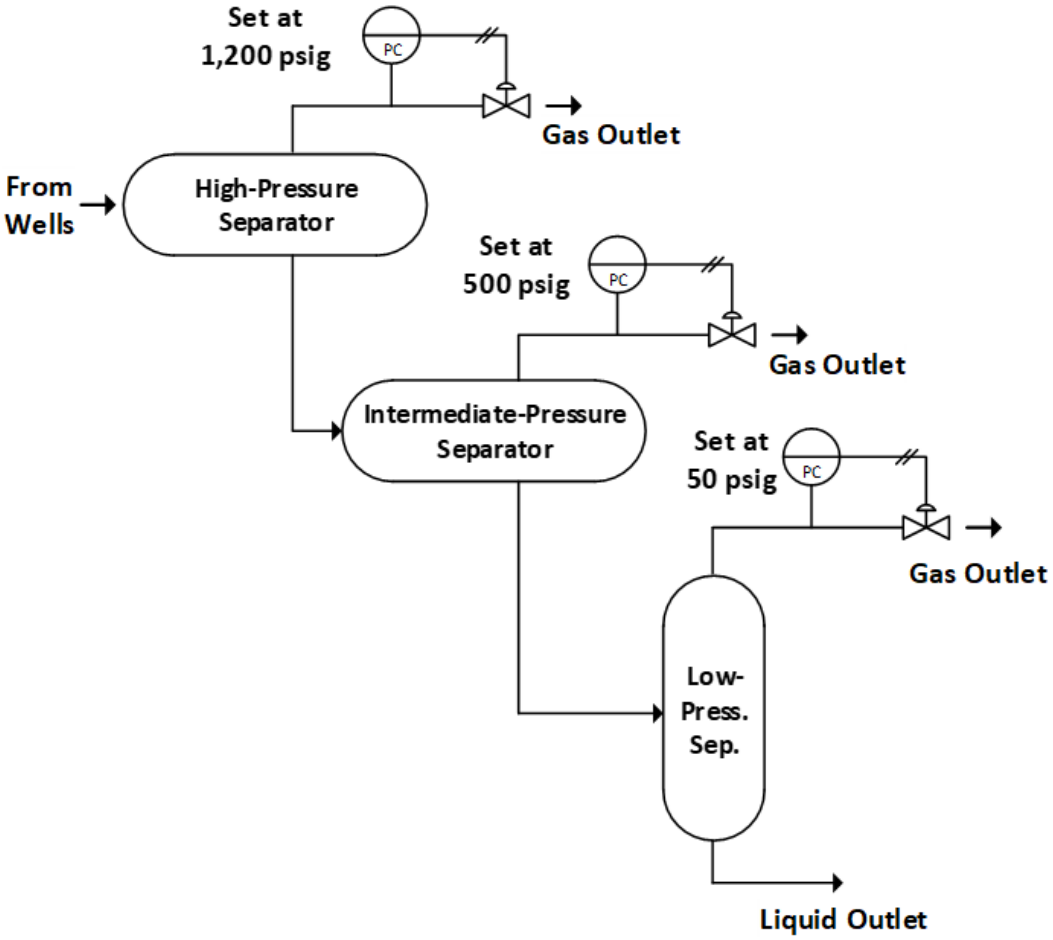

Figure 2.4: Example three-stage separation process, adapted from Stewart and Arnold (2008)

where available area is at a premium, such as offshore platforms or existing refineries. Vertical separators also offer considerable advantages when it comes to solids handling, since the liquid outlet can be placed directly at the center of the vessel bottom. This can help mitigate sand buildup within the separator (Arnold and Stewart, 1998). Finally, vertical separators offer greater surge capacity compared to horizontal separators.

The pressure at which the gas-liquid separation is to be performed may also play a significant role in the selection of the vessel design. If the hydrocarbon stream has a pressure drop prior to entering the separator (or within the separator itself), some amount of dissolved gas will come out of solution. Vessels where a significant

amount of solution gas is expected to come out are often referred to as flash vessels, though they are identical in form to the aforementioned separators. Since liquid degassing is usually the separation bottleneck in these high pressure units, these separators are typically horizontal in orientation. As example of this can be seen the three-stage separation process shown in Figure 2.4.

2.2 Cyclone Separators

As petroleum production has been pushed to more remote and extreme environments, there has been increased interest in separator vessels that are smaller in size compared to conventional separators. Cyclone separators can be viewed as a more compact alternative to conventional gas-liquid separators. Cyclone separators, also referred to as compact separators, are separators that rely on centrifugal forces as the driving force for phase separation instead gravity alone. Cyclone separators function by swirling the incoming gas-liquid multiphase stream. This swirling produces a centrifugal force that drives the denser liquid phase towards the separator walls while the less-dense gas phase remains in the center. The centrifugal acceleration generated by cyclone separators can exceed the acceleration produced by gravity alone by up to three orders of magnitude (Austrheim, 2006). The increased driving force for separation allows cyclone separators to be smaller and lighter than traditional separators.

Cyclone separators come in a variety of different configurations. An example of a popular cyclone separator, the Gas-Liquid Cylindrical Cyclone (GLCC) can be seen in Figure 2.5 (Kouba and Shoham, 1996). The GLCC functions by feeding the multiphase gas-liquid stream through an inclined inlet section which then enters tangentially to the separator. Due to the angle of the inlet, the gas-liquid stream is swirled around the body of the separator, promoting separation of the two phases. The liquid flows down the separator wall towards the liquid exit and the gas flows

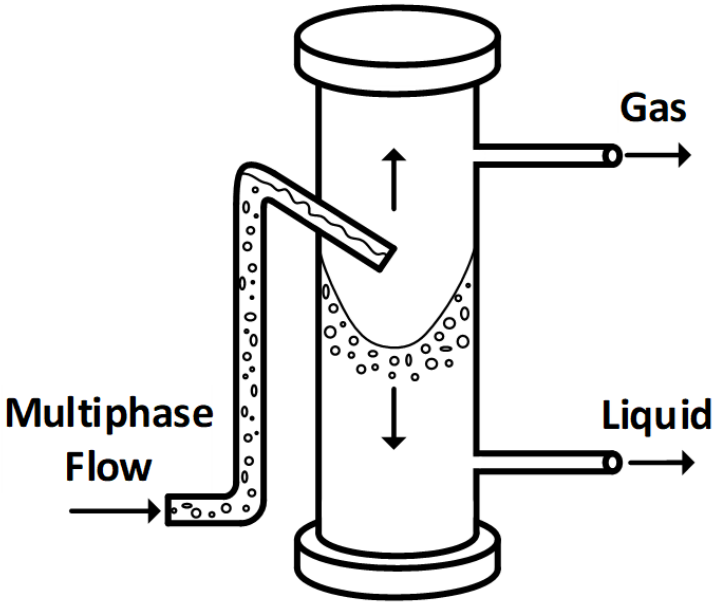

Figure 2.5: Schematic of a GLCC separator, adapted from Erdal et al. (1997)

upwards towards the gas exit. The GLCC is known as a tangential flow centrifugal separator since the inlet flow enters the main separator body tangentially. Axial flow separators, on the other hand, swirl the liquid along the same axis as the inlet flow by passing the multiphase stream over a helical vane.

Although cyclone separators have a size advantage over conventional gas-liquid separators, they are not commonly employed in production operations. The centrifugal force which is required for separation, is very sensitive to the gas and liquid flow rates. Variability in the inlet flow will more than likely result in poor separation efficiencies. Also, the energy consumed by the swirling of the gases and liquids results in a pressure drop that is larger than what would otherwise be expected in a conventional separator. This pressure drop could result in higher pumping/compression cost further downstream. Lastly, the design of cyclonic separators is often proprietary, making it difficult for engineers to model and operate these separators.

2.3 Separator Internals

Conventional gas-liquid separators can be equipped with various separator internals in attempt to increase the separation efficiency. Separator internals help promote better separation by more evenly distributing the stream flow, increasing coalescence of both droplets and bubbles, as well as mitigating conditions that are detrimental to good separation. Conditions that involve foaming, liquid waves within the separator, or solid deposition should be avoided if good separation efficiencies are to be maintained.

2.3.1 Inlet Conditioning Devices

The purpose of inlet conditioning devices is to reduce the momentum of the inlet stream flowing into the separator (Bahadori, 2014). This decrease in the stream momentum right at the beginning of the separator usually performs the initial bulk gas-liquid separation as well as preconditions the distribution of the gas flow. Ideally, droplet shearing is also minimized within this region to avoid droplet breakup into smaller droplets. There are many different types of inlet conditioning devices, as seen in Figure 2.6.

The diverter plate and dished head function by rapidly changing the direction of the inlet flow. By imposing a sudden change in the direction of the flow, the denser liquid phase with a higher momentum compared to the gas phase strikes the plate, accumulates, and falls to the bottom of the vessel. The less-dense gas phase tends to flow around the plate and disengage from the liquid. The benefit of the diverter plate-type inlet conditioning devices is that they are relatively simple to design and install.

The reversed pipe or half-pipe configuration also consist of a relatively simple design. The reversed pipe is simply a piece of pipe that redirects the flow towards the back of the separator. A half-pipe design directs the inlet flow downwards into

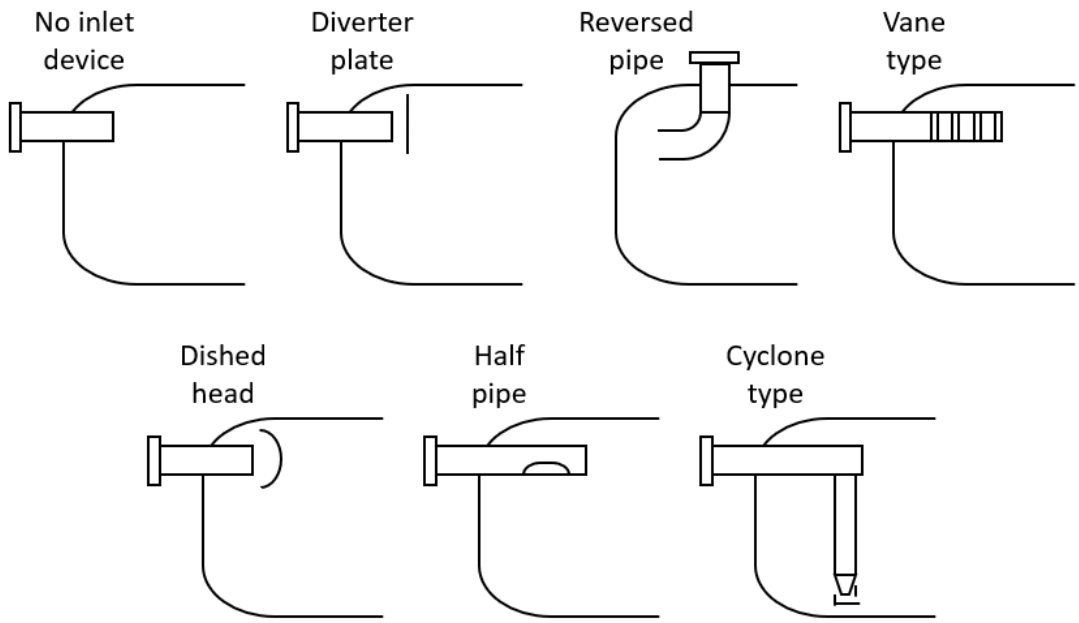

Figure 2.6: Example of different inlet conditioning devices, adapted from Bothamley (2013*a*)

the separator. The disadvantage of pipe-type inlet conditioning devices is that they have the potential to further entrain gas into the liquid.

More complex inlet conditioning devices include inlet vanes and inlet cyclones, both relying on centrifugal forces to enhance separation. Inlet vanes consist of a series of curved fins that divert the flow outward into the separator. The curvature of the vanes promotes inertial impact of liquid droplets while the gas flows around them. Cyclonic inlet conditioning devices generate the centrifugal forces by swirling the inlet stream tangentially, similar to the behavior standalone cyclone separators seen in Section 2.2. The same disadvantages apply to centrifugal inlet conditioning devices as previously mentioned for standalone cyclone separators, namely: the separation performance is sensitive to the inlet flow and the resulting separation produces a relatively high pressure drop. The advantage of using centrifugal-type separators as inlet conditioning devices as opposed to standalone units is that if the inlet conditioning device fails to properly separate the gas and liquid phases, the phase separation can

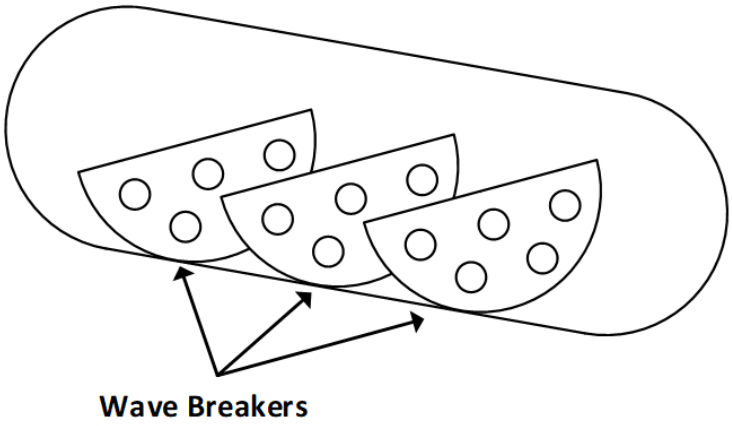

Figure 2.7: Wave breakers inside horizontal separator, adapted from Stewart and Arnold (2008)

still occur within the vessel volume, mitigating to some extent the sensitivity to the flow rate. New separator designs typically employ either vanes or centrifugal inlet conditioning devices (Bothamley, 2013*a*).

2.3.2 Wave Breakers

Large horizontal separators often require wave breakers to prevent sloshing within the vessel. These anti-wave elements usually consist of perforated baffles positioned along the length of the separator. The baffles help minimize disturbances to the liquid flow and are particularly useful in three-phase separation. An example of these wave breakers can be seen in Figure 2.7.

2.3.3 Foam Breakers

Foaming has the potential to greatly reduce the capacity of gas-liquid separators due to the increased residence times required to dissipate the foam. If foam is still present at the end of a separator's residence time, the foam can be pulled into the separator outlet, potentially jeopardizing equipment not meant to handle foam further downstream. Foam breakers assist in foam mitigation by forcing the foam

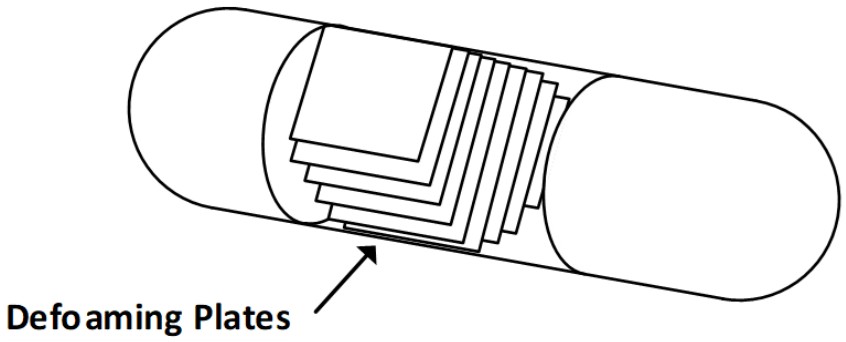

Figure 2.8: Example of foam breaker inside a horizontal separator, adapted from Arnold and Stewart (1998)

through a series of parallel plates. These closely spaced plates, as shown in Figure 2.8, expose the foam to additional surface area, breaking up the foam as it is dragged across the surface of the plate.

2.3.4 Mist Extractors

As the gas flows through the separator, droplets too small to be separated within the bulk of the separator will still be present in the exiting gas stream. To ensure as much of this fine mist is captured as possible, mist extractors are often employed at the gas outlet. Like the inlet conditioning device, there are a variety of different mist extractors available. Common mist extractor designs include wire mesh, vane packs, as well as cyclones.

Wire mesh mist extractors, as the name implies, is a mesh of knitted wires through which the exiting gas stream is passed. Wire meshes are also the most common mist extractors found in production operations (Stewart and Arnold, 2008). The knitting of the wires allows the meshes to have a large surface area and void fraction. The effectiveness of the wire mesh is dependent largly on the gas velocity being in the proper range. If the gas velocity is too low, the fine droplets will simply drift through the mesh without colliding with any of the wire elements. If the gas

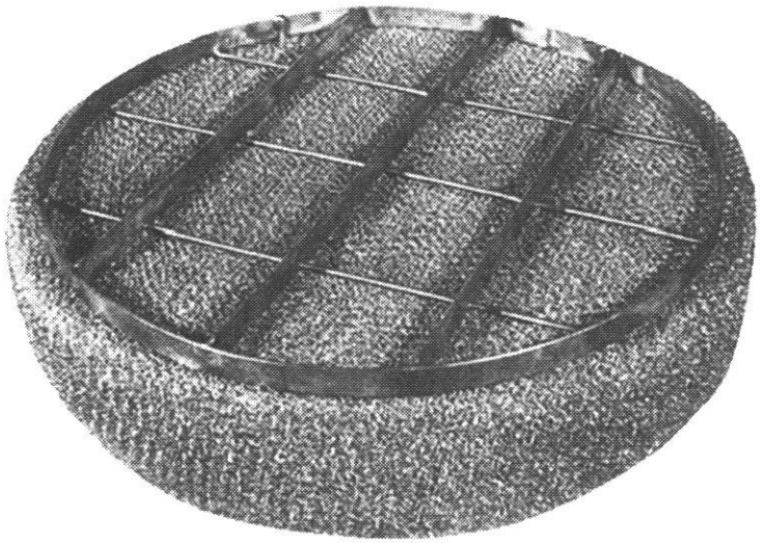

Figure 2.9: Wire mesh mist extractor, reproduced with permission from Elsevier, B.V. Stewart and Arnold (2008)

velocity is too high, liquid droplets that collided with the wires will be re-entrained into the gas phase. An example of a wire mesh can be seen in Figure 2.9.

Vane mist extractors function in a similar manner to wire meshes, though parallel plates are instead used as a source of surface area available for droplet collision. Within a vane pack, these parallel plate contain directional changes, impinging droplets onto the surface where they coalesce and fall to the liquid collection area. An example of a vane mist extractor can be seen in Figure 2.10.

Mist extractors are susceptible to plugging if the liquid stream is prone to solid deposition. Bypass lines or removing the mist extractor entirely may be needed to rectify the issue if the plugging is acute (Lyons, 2009).

2.4 Separator Sizing

When sizing a separator, the capacity of the separator in both the gas and liquid phases must be considered. Proper sizing of a gas-liquid separator is contingent on allowing the liquids to sufficiently separate from the gas phase and the gases to

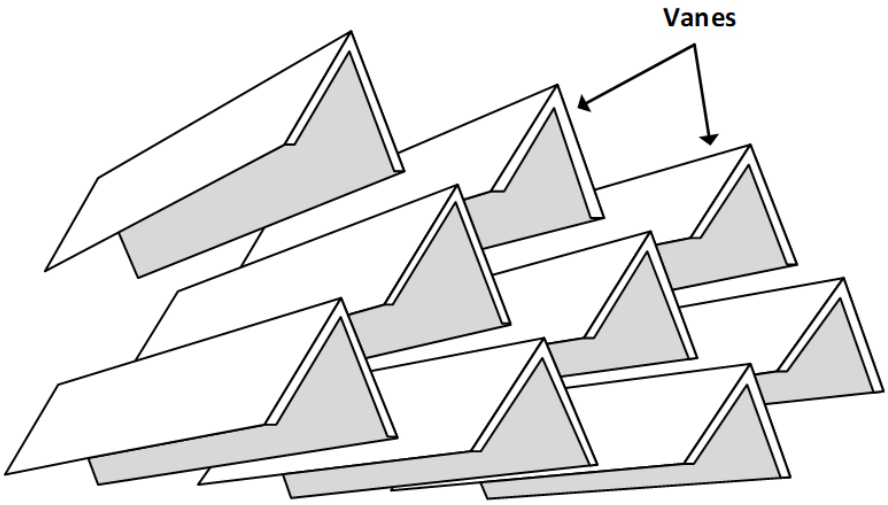

Figure 2.10: Vane mist extractor, adapted from Arnold and Stewart (1998)

sufficiently separate from the liquid phase. Both the droplet and bubble separation capacities can be considered independently. Since liquid degassing is the main focus of this research, only horizontal separators will be considered here.

2.4.1 Droplet Separation Capacity

The residence time of the gas phase within the separator can be calculated by dividing the vessel length, L_{ves}, by the gas phase velocity, v_{g},

$$t_{\text{r,g}} = \frac{L_{\text{ves}}}{v_{\text{g}}} \tag{2.1}$$

Within the gravity separation section of the gas-liquid separator, a droplet can be considered separated if it is large enough to travel from the gas inlet to the liquid surface within the residence time of the gas phase (Bothamley, 2013*b*). If the vertical height between the droplet inlet and the liquid surface is taken as h_{g}, the minimum droplet velocity required for separation can be calculated using

$$v_{\text{t}} = \frac{h_{\text{g}} v_{\text{g}}}{L_{\text{ves}}} \tag{2.2}$$

where v_t is the terminal droplet velocity. This terminal droplet velocity is then dependent on the size of the droplet as well as the physical properties of the liquid and gas phases. Performing a force balance on a droplet in an upward flowing gas stream, the terminal settling velocity of the droplet can be calculated

$$v_t = \sqrt{\frac{4gd(\rho_l - \rho_g)}{3C_D\rho_g}} \tag{2.3}$$

The drag coefficient, C_D, is known to be a function of the Reynolds number of a droplet in the gas phase. The Reynolds number is thus defined as

$$Re_g = \frac{dv\rho_g}{\mu_g} \tag{2.4}$$

If the droplet Reynolds number is $Re_g < 1$, the droplet is said to be in the Stokes flow regime. The droplet drag coefficient can then be calculated using

$$C_D = \frac{24}{Re_g} \tag{2.5}$$

For droplets with Reynolds numbers larger than 1, but less than 1000, the drag coefficient correlation formulated by Putnam can be used (Putnam, 1961)

$$C_D = \frac{24}{Re_g}\left(1 + \frac{Re_g^{2/3}}{6}\right) \tag{2.6}$$

This range in droplet Reynolds number is usually sufficient to characterize the droplet velocities in most separator applications (Austrheim, 2006). Combining Equations 2.2 and 2.3, the smallest droplet diameter expected to be completely separated can be found, d_{100}. All droplets larger than this diameter are assumed to be completely separated within the gravity settling region of the separator. Only droplets smaller than d_{100} are assumed to persist in the exiting gas stream. When designing a separator, the vessel diameter and/or vessel length can be adjusted to

ensure droplets of a given size are separated.

2.4.2 Bubble Separation Capacity

Historically, sizing separators for an adequate bubble separation capacity has been done using the API 12J guidelines shown in Table 1.1. For a given crude API gravity, the API 12J guidelines will recommend a liquid residence time range required for adequate bubble separation. There is reason to believe, however, that these guidelines represent an oversimplification of the degassing process since the only variable assumed to significantly effect liquid degassing is the API gravity of the oil.

The API gravity of a crude oil is generally known since the quality of a crude is mainly evaluated based on this metric (Riazi, 2005). Higher API gravity oils have a lower specific gravity which also usually correlates to lower aromatic content, lower pour point, lower viscosity and lower carbon-to-hydrogen weight ratio. Higher API crudes are considered lighter while lower API crudes are considered heavier. The API gravity of an oil can be directly calculated from the specific gravity at 60 °F.

$$^{\circ}\text{API} = \frac{141.5}{\text{SG}} - 131.5 \tag{2.7}$$

where the specific gravity at 60 °F is defined as

$$\text{SG} = \frac{\rho_{\text{oil}}}{999\,[\text{kg/m}^3]} \tag{2.8}$$

Taking the average of the API gravities and the recommended residence times, and converting the API gravities to liquid densities, the API 12J guidelines can then be seen in Table 2.1. Here it is shown that increased liquid densities should require larger residence times. From a physical perspective, these results are somewhat confounding. For a bubble rising in liquid, the bubble velocity is a function of the bubble's buoyancy in the liquid, assuming no bubble growth within the medium. This

velocity can be calculated using Equation 2.3 in an analogous process to the droplet velocity calculation. According to this equation, holding all else constant, higher liquid densities should result in faster bubble velocities. Faster bubble velocities would then in turn require less liquid residence time to be separated. This reasoning is in contradiction to the results shown in Table 2.1.

Table 2.1: API 12J degassing guidelines with liquid density

Oil Density [°API]	Specific Gravity	Density [kg/m^3]	Retention Time [min]
35	0.85	849	1
25	0.90	903	1.5
15	0.97	965	3

While the API gravity of a crude oil is defined from the specific gravity, the API gravity is known to correlate with the liquid viscosity as well. The chart in Figure 2.11 depicts the approximate kinematic viscosity and temperature correlation used by the American Society for Testing and Materials (ASTM) for different crude oil API gravities. Using this correlation, approximate kinematic viscosities can be found at 60 °F (15.6 °C). Converting to dynamic viscosities, these values are listed in Table 2.2.

Table 2.2: API 12J guidelines with liquid viscosity

Oil Density [°API]	Density [kg/m^3]	Kinematic Viscosity [cSt]	Dynamic Viscosity [cP]	Retention Time [min]
35	849	5.0	4.2	1
25	903	130	120	1.5
15	965	5000	4800	3

Assuming a bubble is within the Stokes flow regime, the bubble velocity will vary in proportion to the liquid viscosity by a factor of $v \propto \mu^{-1/2}$. Assuming that the residence time requirement of the liquid is inversely proportional to the bubble velocity, the liquid residence time will be proportional to the liquid viscosity by a factor of $t_r \propto \mu^{1/2}$. With the rapid increase in dynamic liquid viscosities shown in

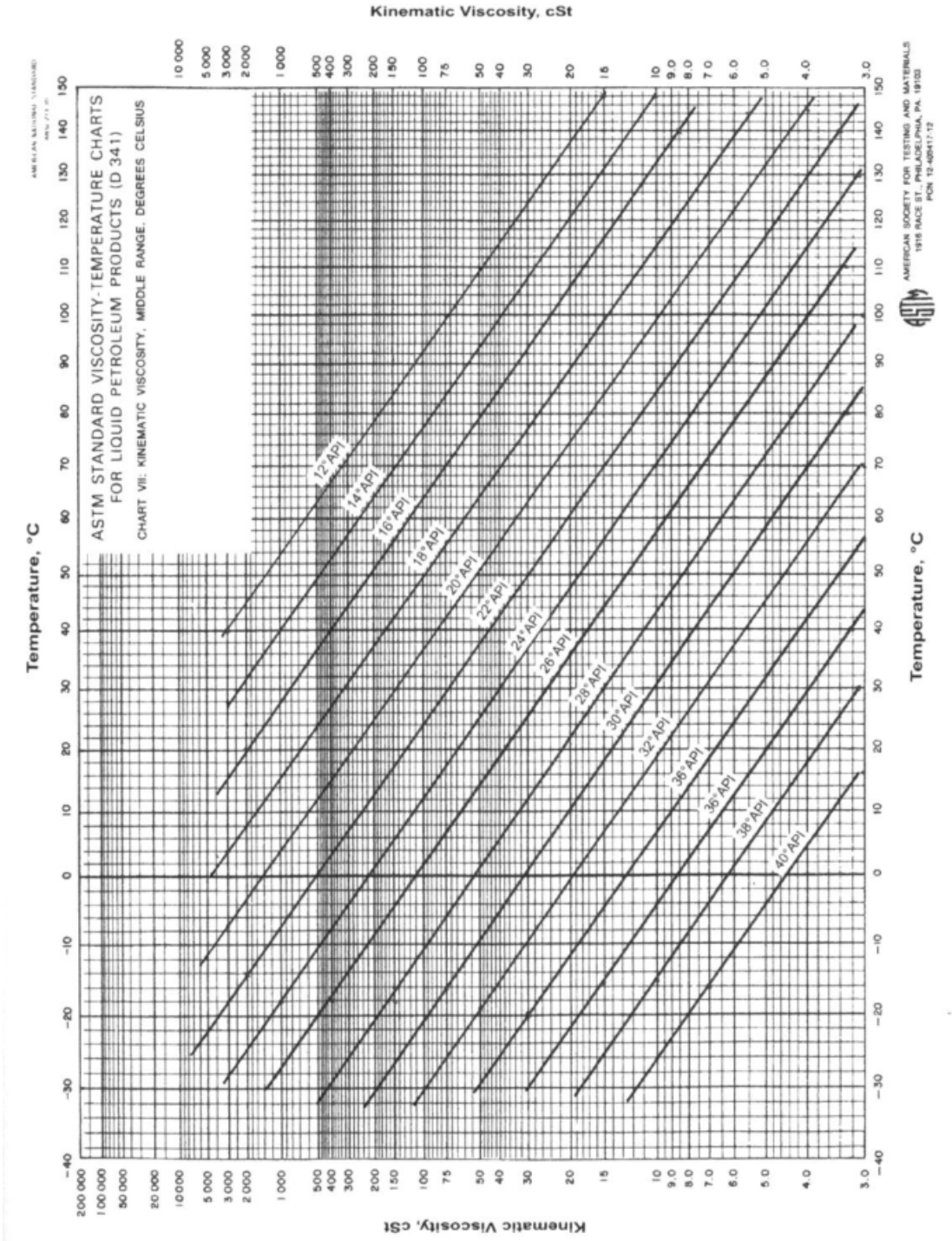

Figure 2.11: Approximate viscosity-temperature relationship for different crude API gravities, reproduced with permission from ASTM International ASTM (2017)

Table 2.2, the associated liquid residence time increases do not adhere to the previously stated proportionality. Although viscosity correlations in the low API gravity range are known to be unreliable (Riazi, 2005), these conclusions further indicate that the API 12J guidelines may be poorly suited for some conditions, particularly more viscous oils.

While other degassing guidelines exist, most are not particularly quantitative, especially if gas evolution is to be considered in conjunction with entrained gas bubbles rising out of the liquid. The GPSA Engineering Data Book, for example, recommends that the velocity of a single 200 μm bubble within the fluid of interest be calculated and multiplied by the liquid residence time within the separator. If the bubble rise is greater than the liquid height, it can be assumed that resulting liquid would contain a free gas volume of less than 1% (GPSA, 2016). There is however, no quantitative evidence provided for this assertion.

Bothamley also recommended that a version of the droplet separation capacity calculation seen in Section 2.4.1 be employed for bubbles in the liquid phase instead (Bothamley, 2013*b*). This method requires the estimation of a bubble size distribution due to a liquid jet plunging into a bulk liquid, an estimation of the volume of entrained gas, and calculation of the bubble velocities using Equations 2.1 – 2.3 replacing the gas with the liquid phase physical properties. While more quantitative than the previously presented degassing guidelines, the gas and liquid phase entering the separator are still assumed to be at equilibrium with one another. If gas evolution is to be accounted for within horizontal separator designs, the transient liquid concentration must be considered as well as changes to the total gas-liquid interfacial area over time. In order to create a better understanding of the degassing process with the occurrence of gas evolution, the dynamics of bubbles in liquids must first be considered.

CHAPTER III

BUBBLE DYNAMICS

The following material in Sections 3.1 to 3.4 has been reproduced in part with permission from Elsevier, B.V. [Lavenson, D. M., Kelkar, A. V., Daniel, A. B., Mohammad, S. A., Kouba, G., Aichele, C. P. (2016). "Gas evolution rates - A critical uncertainty in challenged gas-liquid separations" Journal of Petroleum Science and Engineering, 147, 816-828].

Gas evolution, in the present context, refers to the process of evolution to the bulk gas phase of initially dissolved gas from solution. The entire life cycle of a bubble being produced by excess solution gas, starting from nucleation, through detachment, growth, rise, and coalescence is shown in Figure 3.1. Gas evolution rates are thus expected to depend on the rates of bubble nucleation, growth, rise and coalescence at bulk gas-liquid interface.

3.1 Bubble Nucleation

Given the definition provided for the evolution of solution gas, it is appropriate to begin with an examination of the literature on bubble nucleation. Bubble nucleation is a well-studied field due to the several academic and industrial intersections - boiling, cavitation, the beverage industry, electrolysis, and more (Carey, 1992; Ghiaasiaan, 2007). Bubbles are generated due to disruptions in the thermodynamic equilibrium state of the system as a result of either super-heating or supersaturation. A supersaturated state is a prerequisite for gas evolution in the context of gas-liquid separators. Gas bubbles in the liquid will form as a result of a phase change occur-

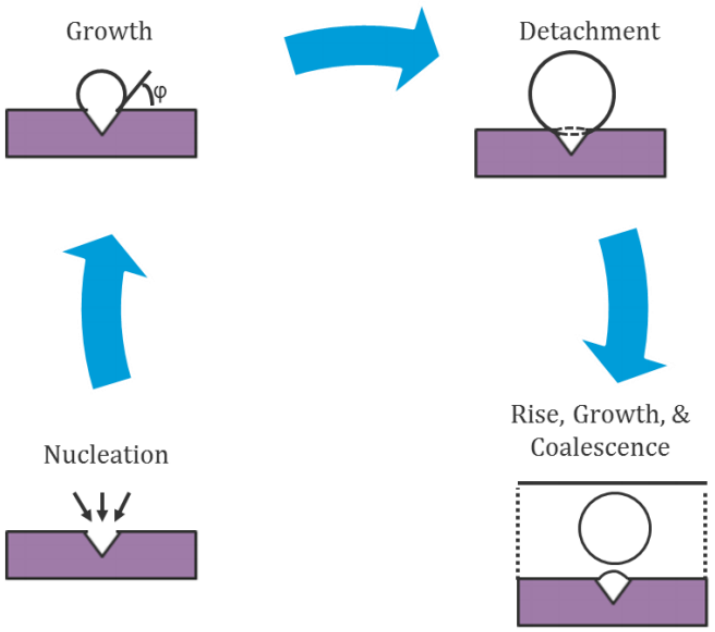

Figure 3.1: Schematic of the evolution cycle of a bubble showing nucleation, growth at site, detachment, rise (and growth), and finally coalescence with bulk gas-liquid interface

ring in the system that is driven by the super-saturated condition. While superheated systems have their relevance in certain applications, this review and discussion will henceforth use the broader term of supersaturation to describe systems of interest.

The driving force of bubble formation is the degree of supersaturation. Consider first a hypothetical gas-liquid system at saturation with some mole fraction, x_{b}, of dissolved gas in the liquid phase at a given temperature and pressure, condition A. Suppose the same system is now depressurized isothermally some ΔP to a new state B, resulting in a supersaturated liquid. The liquid will release gas to reach a new saturation mole fraction, x_{i}, of dissolved gas until it again reaches the equilibrium solubility curve at B. This process is illustrated in Figure 3.2.

Lubetkin (Lubetkin and Blackwell, 1988) defines the supersaturation ratio, ξ, as

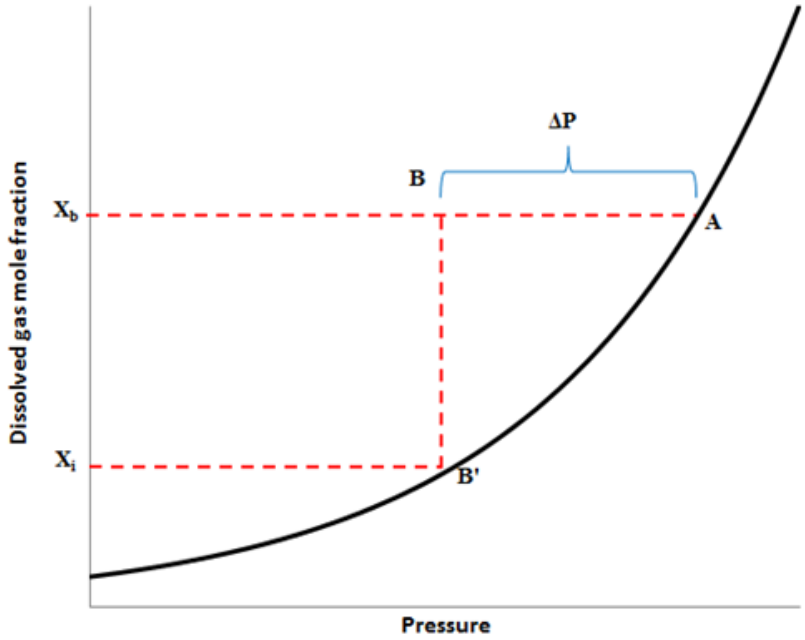

Figure 3.2: Dissolved gas mole fraction as a function of pressure for a given arbitrary system (units on both scales are arbitrary)

$$\xi = \frac{x_\mathrm{b}}{x_\mathrm{i}} - 1 \tag{3.1}$$

In supersaturated systems, bubbles emerge from so-called nuclei in various sizes. At radii below a certain critical value, R_c, bubbles will tend to collapse, while for radii equal to or greater than the critical value, they will tend to grow and participate in the gas evolution cycle. This critical radius is defined using the Laplace equation

$$\Delta P = \frac{2\sigma}{R_\mathrm{c}} \tag{3.2}$$

where σ is the surface tension of the gas-liquid interface and ΔP is the difference between the bubble vapor pressure and the pressure on the external liquid phase. Brennen postulated that, for a pure supersaturated liquid, the work required to form a bubble of critical radius R_c is given by (Brennen, 2013)

$$W_{\mathrm{c}} = \frac{16\pi\sigma^3}{3(\Delta P)^2} \tag{3.3}$$

This work can be expressed as a function of the supersaturation by using Henrys law defined in Equation 3.4

$$H = \frac{P_{\mathrm{i}}}{x_{\mathrm{i}}} \tag{3.4}$$

$$W_{\mathrm{c}} = \frac{16\pi\sigma^3}{3P_{\mathrm{i}}^2\xi^2} \tag{3.5}$$

where H is the Henry's law constant and P_{i} is the pressure at which the Henry's law constant is calculated, or at state A in Figure 3.2.

As supersaturation increases, the work required to form a critical radii bubble decreases. This work is considered an energy barrier for the system to overcome to nucleate bubbles. Consider also the effect of surface tension on the energy barrier. The work required to nucleate bubbles increases cubically with the surface tension assuming a constant supersaturation. The system surface tension is thus critical to understanding the barriers hindering bubble nucleation.

Bubbles can nucleate in a variety of locations within the liquid phase, including the bulk, on particles in the bulk, on smooth solid surfaces, or in cavities and surface imperfections. Defining and classifying these nucleation types has been the subject of many studies, including the development of an accepted nomenclature. Bubble nucleation is often classified into four different types of nucleation – types I-IV (Jones et al., 1999). Type I and II nucleation, also known as classical nucleation, are defined as homogeneous and heterogeneous nucleation, respectively. Typically, the levels of supersaturation required for type I and II nucleation are quite high. Type III nucleation is referred to as pseudo-classical nucleation, which includes both homogeneous and heterogeneous nucleation. This nucleation occurs at pre-existing gas cavities, but

the radius of curvature of the cavity's meniscus is less than the critical bubble radius. This results in a smaller energy barrier for nucleation to occur. Type IV nucleation is defined as non-classical nucleation since it assumes that cavities exist where the radii of curvature are greater than the critical bubble radius, and thus there is no nucleation energy barrier to overcome.

Classical nucleation (types I and II) dates back to several studies in the early 20th century (Becker and Döring, 1935; Farkas, 1927; Volmer, 1926) with several reviews available on the topic (Cole, 1974; Frenkel, 1946; Kulkarni and Joshi, 2005; Lubetkin, 1995; Sides, 1986). The details of classical nucleation theory (CNT) itself will not be discussed here due to sufficient past treatment in the literature. Hemmingsen found that classical bubble nucleation required supersaturation levels of 100 and more (Hemmingsen, 1975). In most situations of interest, bubbles form under low levels of supersaturation out of pre-existing gas cavities and therefore, classical mechanisms for bubble formation in most practical scenarios is not expected to be important (Enríquez et al., 2013).

Type III and IV nucleation, by definition, require much lower levels of supersaturation to promote bubble nucleation. A variety of studies have illustrated this result, with many focusing on the importance of pre-existing gas cavities on the rate of bubble nucleation. Harvey et al. were some of the first to demonstrate these effects (Harvey, 1945; Harvey et al., 1947). Early studies remarked the significant increase in bubble production if the nucleating surface was roughened or dirty. They hypothesized the existence of preformed nuclei, referred to as Harvey nuclei, which have a radius of curvature greater than the critical radius. They also compared the effects of attempting to remove the gas cavities initially on the nucleation supersaturation requirements. When the gas cavities were deactivated, they found nucleation occurred at high supersaturation levels consistent with type II nucleation events. This was in contrast with samples that did not have the cavities deactivated which showed only

low levels of supersaturation necessary to initiate bubble formation.

Chen studied the onset of bubble nucleation in a heterogeneous setting by investigating nucleation on particles (Chen et al., 1993). They measured the nucleation rate and found it to be higher than the predicted value, as a result of a reduction in the energy barrier to nucleation and in line with type III and IV nucleation definitions. Other studies have also confirmed the preference of bubble nucleation for active sites and pits, even observing the formation of consecutive bubbles, thereby confirming that the gas evolution process is indeed a repeating cycle at active locations (Clark et al., 1959; Westerheide and Westwater, 1961). Further studies have probed the effect of hydrophobicity of surfaces on the formation of bubbles. Researchers have argued the existence of a crevice model based on a hypothesis that hydrophobic impurities in surfaces exist at the bottom of cavities (crevices) where microbubbles may exist (Crum, 1982; Strasberg, 1959; Vinogradova et al., 1995; Winterton, 1977). This allows for micron and sub-micron bubbles to exist in cavities where there is no water-surface contact, supporting the hypothesis that pre-existing cavities are critical foundations of type III and IV nucleation events.

Bauget and Lenormand reviewed bubble formation literature in porous media, with an emphasis for the application of solution gas drive in heavy oil production (Bauget et al., 2002). They noted, in agreement with Jones et al (Jones et al., 1999), that in many occasions the necessary supersaturations to induce bubble formation were much lower when measured experimentally than compared with the predicted values. Bauget and Lenormand also reviewed a heterogeneous thermodynamic model which incorporated a correction factor to reduce the required activation energy for bubble formation. However, they recognized that both thermodynamic models were ineffective at describing nucleation in boiling or depressurization systems. Instead, they too argued the necessity of a model that incorporates pre-existing gas nuclei. The inclusion of pre-existing gas nuclei is often included in porous media models

(Dominguez, 1997; Hirasaki et al., 1988). The models classify the pre-existing gas phase either as present as bubbles in the bulk liquid or trapped in the roughness of the solid. The models, however, do not aid in the interpretation of the experimental results available in the literature. This includes the existence of a minimum supersaturation required to nucleate bubbles, based on the maximum size of any pre-existing bubbles (El-Yousfi, 1992; El Yousfi et al., 1997; Wang and Dhir, 1993; Yang and Kim, 1988)

The field of bubble nucleation has been widely researched, including both classical and non-classical types of nucleation. While the literature correctly identifies the underlying thermodynamic parameters that govern classical nucleation, it has become apparent that for most practical applications bubble nucleation is governed by type III and IV nucleation events. Nevertheless, an understanding of bubble nucleation in systems and conditions relevant to oil production is lacking. Quantitative data are needed on nucleation rates of relevant gases (methane, ethane etc.) on pipe (carbon steel) walls in a variety of flow situations.

3.2 Bubble Growth

After the nucleation process concludes, the bubble is free to grow, and eventually detaches from the surface. The bubble growth process is complicated, involving simultaneous mass, momentum, and energy transfer between the expanding bubble and the fluid surrounding it. The growth rate is influenced by the rate of molecular diffusion to the interface of the bubble, liquid inertia in the region surrounding the bubble, viscosity, and surface tension.

Early studies focused on the heat transfer-controlled growth of vapor bubbles (nucleate boiling) rather than bubble growth from dissolved gas where mass transfer dominates. These studies, including Plesset and Zwick (Plesset and Zwick, 1954), and Foster and Zuber (Forster and Zuber, 1954) were limited to the spherically symmetric

growth of single, isolated, bubbles controlled by heat transfer inside infinite liquids of constant superheat. Scriven obtained an analytical solution for spherical bubble growth controlled by the transport of mass and heat in an infinite pool of liquid using similarity analysis (Scriven, 1959). For single bubble growth in uniform temperature fields, such as during nucleate boiling, his analysis produces a simple parabolic relationship for bubble growth; $R \propto t^{1/2}$, where R is the bubble radius and t the time of growth. The proportionality is related to the thermal (or molecular) diffusivity and superheat (or supersaturation) in heat transfer (or mass transfer) controlled growth. Scrivens similarity analysis assumes an initial bubble size equal to zero, which is erroneous for several situations. Deviations from his parabolic relation have been reported from experimental and theoretical works and depend on the liquid properties (Divinis et al., 2006; Kostoglou and Karapantsios, 2005). A systematic study of some of the effects resulting in the deviation of the parabolic profile is available (Enríquez et al., 2014). Moreover, bubbles produced by coalescence of smaller neighboring bubbles do not follow the parabolic growth law (Buehl and Westwater, 1966; Westerheide and Westwater, 1961).

The interest here is primarily in mass-transfer controlled bubble growth. Analysis of this process is complicated by the highly coupled and nonlinear nature of the governing mass and momentum balances and the diffusion equation. The movement of the gas-liquid interface (i.e., bubble size) is related through momentum transfer to the gas pressure inside the bubble. In addition, the requirement of mass conservation relates the bubble radius to the gas pressure and the rate of gas diffusion. Finally, the rate of gas diffusion depends on the movement of the interface through the diffusion equation. These complexities mean there is no known general analytical solution (Arefmanesh et al., 1992). Nevertheless, Scrivens simple parabolic relation has proven to be useful in describing the isothermal mass-transfer controlled bubble growth from supersaturated solutions (Barker et al., 2002; Bisperink and Prins, 1994;

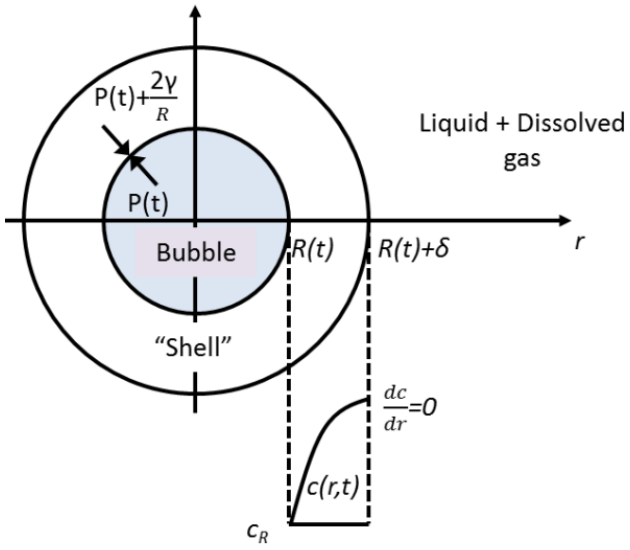

Figure 3.3: Typical single bubble growth model schematic

Glas and Westwater, 1964). In slightly supersaturated solutions, $0 < \xi < 1$, where mass transfer is expected to be diffusion-controlled, however, bubble growth slower than the parabolic relation has been reported (Enríquez et al., 2013). A typical single bubble growth model is schematically shown in Figure 3.3.

Mass-transfer (diffusion) controlled bubble growth in viscous liquids has been treated in other classical papers include those of Barlow and Langlois (Barlow and Langlois, 1962), Street et al. (Street et al., 1971), Szekely and Martins (Szekely and Martins, 1971), and Rosner and Epstein (Rosner and Epstein, 1972). Barlow and Langlois and Szekely and Martins examined bubble growth in Newtonian liquids while Street et al. considered growth in an Ostwald-de-Waele power law liquid. The analysis of Street et al. is further complicated by considering the liquid surrounding the bubble to be finite and a variable liquid viscosity. Barlow and Langlois and Street et al. both solve mass and momentum transfer equations with a simplified diffusion equation, where the concentration gradients are restricted to a thin shell surrounding the bubble. Outside this boundary layer, gas concentration was assumed to be undisturbed and equal to the initial concentration. Under this assumption, the

equations can be combined into a single integro-differential equation which is solved by a finite difference method. Rosner and Epstein used the moment integral method to solve the diffusion equation by assuming a polynomial to describe the concentration profile inside the boundary layer.

$$\frac{C^* - C}{C^* - C_0} = \left(1 - \frac{r - R}{\delta}\right)^2 \tag{3.6}$$

where C^* is the bulk concentration of the gas.

Several researchers, using different polynomial profiles, have adopted Rosner and Epsteins method for mass-transfer controlled growth (or collapse) of bubbles in both viscous Newtonian and viscoelastic liquids (Ruckenstein, 1964). Patel followed a similar approach to develop a simple model with a set of ordinary differential equations describing bubble growth in viscous liquids (Patel, 1980). Payvar used a similar approach to predict the mass transfer-controlled bubble growth during the rapid decompression of a liquid (Payvar, 1987).

Bubble growth takes place at the nucleating site as well as during bubble rise. Liger-Belair et al. found, in studies of bubble production in champagne, that bubble growth rates were constant during ascension (Liger-Belair et al., 2002). Their findings corroborate those of Shafer and Zare (Shafer and Zare, 1991), who also observed the linearity of radius increase with time for bubbles rising in a glass of beer. Liger-Belair et al. developed a simple mass-transfer model for the expansion of bubble radius.

$$\frac{dn}{dt} = k_\mathrm{l} A \Delta C \tag{3.7}$$

where n is the gas moles transfered, k_l is the liquid phase mass transfer coefficient, A is the bubble area, and ΔC is the concentration driving force.

Gas-liquid mass transfer coefficients are also expected to be dependent on the liquid viscosity and superficial gas velocity (Fernández et al., 2015; Zhou et al., 2014).

Moreover, it has been shown that the mass transfer coefficients for gas dissolution (absorption) and evolution (desorption) processes are identical (Hamborg et al., 2010).

Understanding of bubble growth in the context of oil and gas production is limited, although general trends can be inferred from this review. The presence of surface active agents including asphaltenes will further complicate the growth process in real scenarios.

3.3 Bubble Rise

Upon detachment of the bubble from the nucleation site, bubbles begin to rise towards the gas-liquid interface. The rise dynamics are governed by several forces including gravity, buoyancy, drag, surface tension, viscous, and lift forces. Stokes was one of the first to propose a relationship for bubble rise velocity that still holds true in some aspects today (Stokes, 1851). Since that study, there have been numerous more examining various system effects on the bubble rise velocity and trajectory. The importance of a quantitative framework for understanding bubble rise dynamics intersects with many industrial applications, including design of flotation tanks, bubble columns, contactors, gas-liquid reactors, and gas-liquid separations.

Several correlations for bubble rise velocity have been published in the literature with varying levels of utility and robustness (Abou-El-Hassan, 1983; Angelino, 1966; Astarita and Apuzzo, 1965; Clift et al., 2005; Haberman, 1954; Harmathy, 1960; Karamanev, 1996, 1994; Mendelson, 1967; Peebles, 1953; Stokes, 1851). The Stokes rise velocity relationship can be calculated using

$$v = \frac{gd^2(\rho_\mathrm{l} - \rho_\mathrm{g})}{18\mu_\mathrm{l}} \tag{3.8}$$

The above formulation can be arrived at by combining Equations 2.3 – 2.5 using the liquid physical properties as the continuous phase. Stokes law works well for a single spherical bubble, in a pure liquid with minimal surfactant contamination

and no turbulence in the external fluid. It also assumes that there is no slip at the bubble-liquid interface and the bubble itself undergoes no internal circulation. These assumptions curtail the application of Stokes law for more complicated systems. Most other correlations agree, however, with the fundamental assumption of a density difference driving force.

The shape of bubbles also has a strong impact on the bubble rise velocity. Studies have attempted to account for the effects of bubble deformation due to various reasons such as surfactant presence, viscous Newtonian and non-Newtonian liquids, and other physicochemical parameters. Most studies agree with the fundamental principle that rise velocity increases with bubble size (Barnett et al., 1966; Haque et al., 1988; Margaritis et al., 1999). However, these studies illustrate in various ways the effects of bubble shape variations on rise velocity. Grace used a dimensional analysis to highlight the dependence of the Reynolds number (Re) on the Eotvos (Eo) and Morton numbers (M) (Grace, 1973). Clift re-purposed this relationship into a convenient graphical illustration for quickly identifying different bubble shape regimes (Clift et al., 2005). Some of these bubble shapes include spherical, ellipsoidal, wobbling, skirted, spherical-cap, and dimpled ellipsoidal-cap. Clift noted that bubbles tend to be ellipsoidal at intermediate Re and intermediate Eo, wobbling at high Re and moderate Eo, while the spherical-cap, ellipsoidal-cap and skirted regimes require Eo to be large.

In his thesis work, Slettebø compiled several different bubble rise velocity correlations and tested their applicability with gas bubbles in viscous model oils (Slettebø, 2009). Slettebø found that Karamanev drag coefficient correlation based on the Archimedes number worked well for the tested experimental conditions, where Archimedes number is defined as

$$Ar = \frac{g\rho_{\mathrm{l}} d^3}{\mu_{\mathrm{l}}^2}(\rho_{\mathrm{l}} - \rho_{\mathrm{g}}) \tag{3.9}$$

For Archimedes numbers $Ar < 13,000$, the Karamanev drag coefficient correlation becomes (Karamanev, 1994)

$$C_{\mathrm{D}} = \frac{432}{Ar}\left(1 + 0.0470Ar^{2/3}\right) + \frac{0.517}{1 + 154Ar^{-1/3}} \tag{3.10}$$

If $Ar > 13,000$, the the drag coefficient is constant at $C_{\mathrm{D}} = 0.95$. The bubble Reynolds number and Morton numbers are calculated using

$$Re_{\mathrm{l}} = \frac{dv\rho_l}{\mu_l} \tag{3.11}$$

and

$$M = \frac{g\mu_{\mathrm{l}}^4(\rho_{\mathrm{l}} - \rho_{\mathrm{g}})}{\rho_{\mathrm{l}}^2\sigma^3} \tag{3.12}$$

Then, the Tadaki number, introduced by Tadaki and Madea, is calculated using (Tadaki, 1961)

$$Ta = Re \cdot M^{0.23} \tag{3.13}$$

Using the Tadaki number, the bubble shape factor $d_{\mathrm{e}}/d_{\mathrm{h}}$ can be determined

$$\frac{d_{\mathrm{e}}}{d_{\mathrm{h}}} = a \cdot Ta^b \tag{3.14}$$

where the coefficients a and b can be found using Table 3.1

Table 3.1: Tadaki correlation constants (Tadaki, 1961)

a=1	b=0	while $Ta < 2.11$
a=1.14	b=-0.176	while $2.11 \leq Ta < 5.46$
a=1.36	b=-0.28	while $5.46 \leq Ta < 16.53$
a=0.62	b=0	while $16.53 \leq Ta$

Finally, the bubble velocity can be calculated using (Karamanev, 1994)

$$v = \sqrt{\frac{4}{3}\frac{gd}{C_{\mathrm{D}}}}\frac{d_{\mathrm{e}}}{d_{\mathrm{h}}} \tag{3.15}$$

Equation 3.15 in conjunction with Equations 3.10 and 3.14 were found to be in good agreement with experimental results over a range of bubbles shapes and sizes in viscous oils (Slettebø, 2009). At small bubble diameters, Equation 3.15 reduces to Stokes flow in Equation 3.8. The bubble velocity calculation using Equations 3.9 – 3.15 is an iterative process. For a specific bubble diameter, an initial bubble velocity guess is required to solve Equations 3.9 – 3.15. The calculated bubble velocity can then be used as the new initial bubble velocity guess and the entire process is repeated until the error between the guessed and calculated bubble velocities reaches an acceptable value.

3.4 Bubble Coalescence

Throughout the process of gas evolution from solution, bubbles may undergo coalescence. At high supersaturations, bubbles at adjacent nucleation sites may coalesce if the sites are separated by a distance of the order of the magnitude of the detachment diameter (Buehl and Westwater, 1966). Furthermore, the ascending bubbles could coalesce as they approach the interface; a process governed by surface tension forces, film drainage rates, and turbulence. Once at the interface, commonplace observations suggest that bubbles do not instantaneously merge with the bulk gas phase. Depending on the fluid properties, one might observe foam formation, which gradually degrades as bubbles break up. While bubble coalescence, as modeled by film rupture, is widely studied, its role in the gas evolution process has received little attention (Liao and Lucas, 2010). For a single bubble at the bulk gas-liquid interface, the time to merge with the bulk gas phase can be estimated using the formulation proposed by Sambath (Sambath, 2013)

$$t = 10\sqrt{\frac{\Delta\rho r^3}{\sigma}} \tag{3.16}$$

where r is the bubble radius. Within the context of a separator, bubble coalescence is advantageous to efficient separation. As bubbles coalesce, the resulting bubbles will have increased rise velocities within the liquid, further increasing the separator's ability to separate gases from liquids.

3.5 Summary

A complete accounting of the bubble dynamics in a supersaturated liquid includes bubble nucleation, bubble growth, the bubble rise within the fluid, and ultimately the coalescence at the bulk gas-liquid interface. The physics governing each step in the life cycle of a bubble is different and can be modeled with varying degrees of confidence. For example, classical bubble nucleation in pure environments is well understood from a physics-based perspective, but is rarely of practical interest. The non-classical type III and IV nucleation events are the usual mechanisms of bubble generation, though the modeling of such events is challenging to generalize. Modeling a bubble's growth and rise velocity, on the other hand, has been relatively well quantified for a variety of different systems.

CHAPTER IV

MASS TRANSFER

4.1 Gas-Liquid Mass Transfer

Gas evolution out of a supersaturated liquid can be framed in terms of mass transfer from the bulk liquid into the gas. Mass transfer is defined as the net movement of mass from one location to another due to a driving force, which in the case of gas evolution is a concentration difference between the bulk and equilibrium values. The direction of the transfer of mass is also important. Gas being dissolved into an undersaturated solution is referred to as absorption, while gas evolving out of a supersaturated solution is referred to as desorption. Within this context, gas evolution and desorption can be used interchangeably. The interphase mass transfer of both absorption and desorption can be visualized in Figure 4.1.

The variable p represents the gas phase partial pressure, C is the liquid phase solute concentration, and the subscripts b and i refer to the bulk and interface values

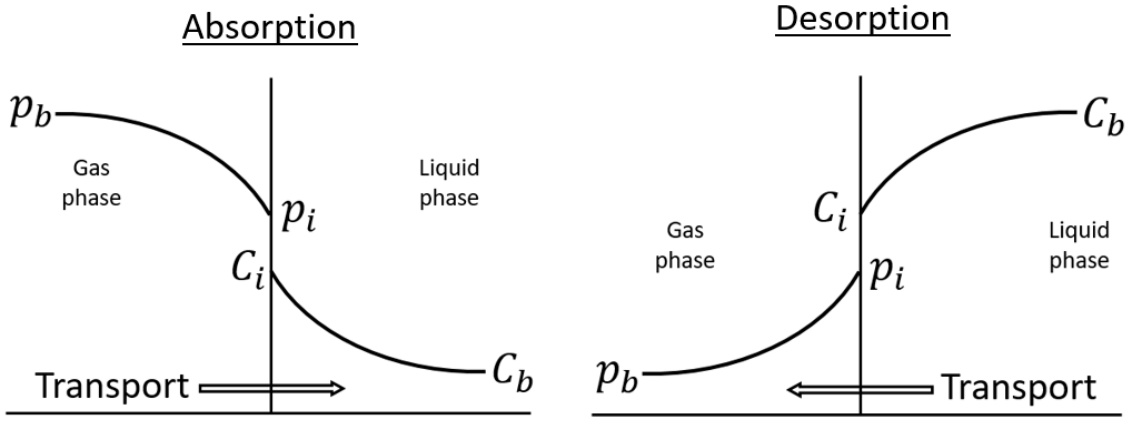

Figure 4.1: Absorption and desorption mass transfer across a gas-liquid interface

respectively. The gas-liquid interface is represented as the vertical line between the gas and liquid phases. During absorption, a gradient forms in the gas-side partial pressure due to the resistance to mass transfer at the gas-liquid interface. As the gas species being absorbed passes through the interface into the liquid, the solute concentration increases until the bulk liquid concentration is reached. During desorption, the exact opposite is true. The bulk solute concentration in the liquid starts high, then decreases as it approaches the interface. Once past the interface, the partial pressure of the gas species decreases until the bulk partial pressure is reached.

The molar flux of the species being absorbed can be written as (Seader et al., 1998)

$$J = k_{\mathrm{g}}(p_{\mathrm{b}} - p_{\mathrm{i}}) \tag{4.1}$$

and

$$J = k_{\mathrm{l}}(C_{\mathrm{i}} - C_{\mathrm{b}}) \tag{4.2}$$

where k_{g} and k_{l} are the gas side and liquid side mass transfer coefficients. The units of k_{g} are in $\mathrm{mol}/(\mathrm{m}^2 \cdot \mathrm{s} \cdot \mathrm{Pa})$ and the units for k_{l} are in $\mathrm{m/s}$. For desorption, the molar flux can instead be written as

$$J = k_{\mathrm{g}}(p_{\mathrm{i}} - p_{\mathrm{b}}) \tag{4.3}$$

and

$$J = k_{\mathrm{l}}(C_{\mathrm{b}} - C_{\mathrm{i}}) \tag{4.4}$$

Under the condition of steady state flow, the flux leaving one phase must be equal to the flux entering the other. Since interfacial concentrations are inconvenient,

if not impossible, to measure, the overall mass transfer form with respect to the liquid is preferred. Taking the desorption case, the overall mass transfer rate can be written as

$$J = K_{\mathrm{l}}(C_{\mathrm{b}} - C^*) \tag{4.5}$$

where C^* is the equilibrium solute concentration in the liquid. For absorption, the concentration difference in Equation 4.5 would simply be reversed. The overall mass transfer coefficient with respect to the liquid side, K_{l}, is then defined using

$$\frac{1}{K_{\mathrm{l}}} = \frac{1}{k_{\mathrm{l}}} + \frac{1}{k_{\mathrm{g}}H} \tag{4.6}$$

where the Henry's constant, H is in units of $(\mathrm{Pa} \cdot \mathrm{m}^3)/\mathrm{mol}$. Using Equation 4.5, the driving force for mass transfer is now defined in terms of bulk concentration values which can easily be measured experimentally. Since only high purity, single compound gases are used for the studies presented here, the resistance to mass transfer on the gas side can be considered negligible with respect to the liquid side, thus $1/(k_{\mathrm{g}}H) \ll 1/k_{\mathrm{l}}$ (Bird et al., 2004). Taking this assumption, the overall rate of mass transfer expressed in Equation 4.5 can be simplified to

$$J = k_{\mathrm{l}}(C_{\mathrm{b}} - C^*) \tag{4.7}$$

During processes where the interfacial area has the potential to vary across different conditions, the flux is usually broken up into two different terms (Welty et al., 2009)

$$\frac{dC_{\mathrm{b}}}{dt} = k_{\mathrm{l}}a(C_{\mathrm{b}} - C^*) \tag{4.8}$$

where the volumetric interfacial area, a is defined as

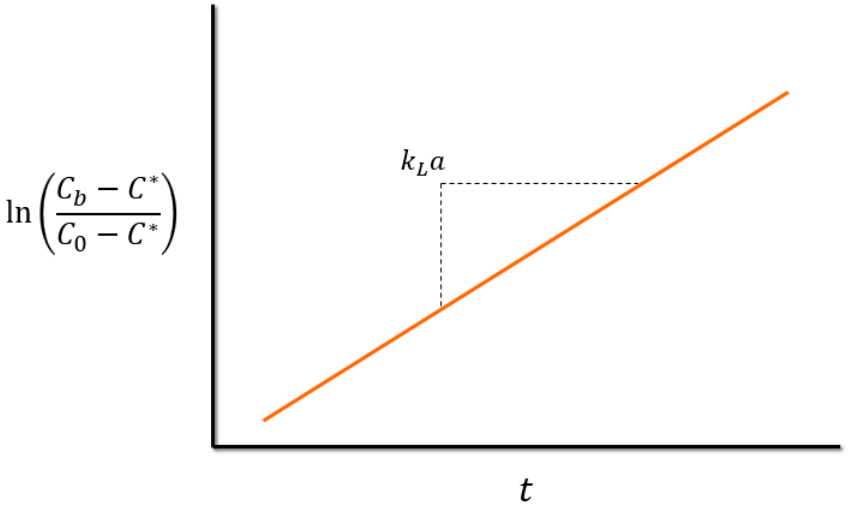

Figure 4.2: Graphical representation of the volumetric mass transfer coefficient calculation

$$a = \frac{A}{V} \tag{4.9}$$

where A is the interfacial area available for mass transfer and V is the liquid volume. By taking the initial condition of $C_{\mathrm{b}}(t = 0) = C_0$ and integrating, Equation 4.8 yields

$$\ln\left(\frac{C_{\mathrm{b}} - C^*}{C_0 - C^*}\right) = k_{\mathrm{l}} a t \tag{4.10}$$

To determine mass transfer coefficients from experimentally measured concentration values, left-hand side of Equation 4.10 can be plotted against time which would yield a curve similar to the one presented in Figure 4.2.

The natural log of the normalized change in solute concentration should yield a straight line when plotted against time. The slope of the resulting linear profile would be the volumetric mass transfer coefficient, $k_{\mathrm{l}}a$. If the interfacial area and the liquid volume is known, the mass transfer coefficient can be decoupled from the volumetric interfacial area.

4.2 Mass Transfer Theories

The rate of mass transfer is known to be a function of the solute diffusivity in the solvent, the physical properties of the associated phases as well as the hydrodynamic conditions (McCabe et al., 1993). Multiple theoretical approaches have evolved to account for these effects on the mass transfer coefficient, k_l.

4.2.1 Film Theory

Film theory, first developed by Lewis and Whitman, assumes that mass transfer is controlled entirely by diffusion through a stagnant film immediately adjacent to the gas-liquid interface (Lewis and Whitman, 1924). The film sublayer is assumed to be of width δ. Beyond the width of the film, bulk mixing is assumed to have no effect on mass transfer. Within the film sublayer, the concentration profile of the diffusing species is linear with respect to the distance from the interface to the end of the film. The concentration of the diffusion species at the end of the film is equal to the bulk concentration. The mass transfer coefficient can be expressed as

$$k_l = \frac{D}{\delta} \tag{4.11}$$

where D is the diffusion coefficient of the species of interest. The film theory, while useful, fails in many important aspects. Experimentally, the dependence of the diffusion coefficient on the mass transfer coefficient has been found to vary from $D^{1/2}$ to $D^{2/3}$ which is substantially lower than the linear dependence predicted by the film theory of mass transfer (Kawase and Moo-Young, 1987). The film width, δ, is also usually measurable within an experimental setting. As such, this term is often treated as an adjustable parameter to fit the experimental data.

4.2.2 Penetration Theory

While film theory assumes that the film sublayer is unaffected by the bulk mixing, the penetration theory, first developed by Higbie, introduces the idea that eddies from the bulk fluid could break into the diffusion layer (Higbie, 1935). These penetrating eddies reside within the film for some renewal time t_e. After the renewal time elapses, the eddies are completely mixed within the diffusion film and the process starts over again. The expression for the mass transfer coefficient within this framework can then be written as

$$k_l = \sqrt{\frac{D}{\pi t_e}} \tag{4.12}$$

While the penetration theory approaches a more realistic representation of mass transfer occurring within real systems, the eddy renewal time t_e is very difficult to determine independently. Like the film width in the film mass transfer theory, the time for eddy renewal is often instead used as a fitting constant to correlate experimental data.

4.2.3 Surface Renewal

The surface renewal theory of mass transfer was developed by Danckwerts as an improvement to the penetration theory (Danckwerts, 1951). The constant renewal time, t_e, was allowed to vary stochastically as a surface renewal rate r, where the mass transfer coefficient can be written as

$$k_l = \sqrt{Dr} \tag{4.13}$$

The mean time between surface renewal events can approximated as $1/r$. The surface renewal theory, like the penetration theory, predicts a more reasonable dependence of the diffusion coefficient on the mass transfer coefficient. While conceptually more

realistic, the surface renewal rate is again difficult to measure and often used instead as a fitting constant.

4.2.4 Large Eddy Model

Several researchers have attempted to develop a version of the surface renewal theory that relates the surface renewal rate explicitly to the bulk mixing of the liquid. Fortescue and Pearson first developed the large eddy model as an extension of the surface renewal model (Fortescue and Pearson, 1967). The model is based on an idealized eddy cell adjacent to the gas-liquid interface and assumes that the largest eddies within the liquid control the rate of mass transfer. The mass transfer coefficient is solved for as

$$k_l = 1.46\sqrt{\frac{D \cdot v'}{L}} \tag{4.14}$$

where v' is the root mean squared of the turbulent velocity fluctuation and L is the integral length scale.

4.2.5 Small Eddy Model

Lamont and Scott developed the small eddy model around a similar idealized eddy cell but instead of the large eddies dominating, the small eddies are assumed to control the rate of mass transfer (Lamont and Scott, 1970). This model was developed with the intent of being generally applicable to a wide variety of mass transfer applications. The small eddy formulation has been used successfully for mass transfer modeling in both bubble columns (Linek et al., 2005; Martín et al., 2009; Wang and Wang, 2007) and stirred tanks (Linek et al., 2004; Buffo et al., 2012). While small eddies are assumed to be the most important scale of mixing, the effect of large eddies within this model are not neglected. Two separate derivations of the mass transfer coefficient formulation were presented: one for mass transfer across

a solid surface

$$k_l = 0.4(\epsilon\nu)^{1/4} Sc^{-2/3} \tag{4.15}$$

and for mass transfer across a fluid surface

$$k_l = 0.4(\epsilon\nu)^{1/4} Sc^{-1/2} \tag{4.16}$$

where ϵ is the energy dissipation rate and ν is the kinematic viscosity of the liquid. The Schmidt number is defined as

$$Sc = \frac{\nu}{D} \tag{4.17}$$

The difference between Equation 4.15 and 4.16 arise from the specification of surface boundary conditions in the derivation. Within the small eddy model, the liquid velocity at the interface can be decoupled into two independent values: the velocity normal to the liquid surface, u, and the velocity parallel to the liquid surface, v. For the solid surface derivation, the surface boundary condition is $u = v = 0$. The fluid surface derivation, on the other hand, takes the surface boundary condition as $u = 0$ and $\partial v/\partial y = 0$, where y is the distance from the liquid interface. In theory, the free fluid surface would allow the parallel liquid velocity streams to exist since the surface is deformable, however the normal liquid velocity is kept at zero if the gas-liquid interface is to remain completely flat. The solid surface derivation instead dictates that the liquid exactly at the interface is completely stagnant.

4.3 Summary

Mass transfer in a gas-liquid system can be modeled using a variety of different theoretical frameworks. While early models, such as the film and penetration theories, were too simple to yield useful predictions, later models were successfully applied to

real systems. The small eddy model derived by Lamont and Scott was found to be one of the most generally applicable theoretical mass transfer models for gas-liquid systems. This model will be used to calculate mass transfer coefficients and make comparisons to experimental results in later chapters.

CHAPTER V

EXPERIMENTAL DEVELOPMENT

As mentioned in Section 1.2, the primary goal of this research was to develop a new method of measuring gas evolution out of supersaturated hydrocarbon solutions at high pressure. Previous experimental studies of gas evolution were limited in their ability to measure gas evolution at pressure and the applicability of the results outside of the experimental apparatus were questionable. To measure gas evolution at high pressure, a new experimental method was required. In this chapter, the development of the high pressure gas evolution experiment is documented.

5.1 Previous Mass Transfer Experimental Designs

Gas evolution, as previously stated, is fundamentally mass transfer occurring between gas and liquid phases. To measure the rate of mass transfer, an experiment must be capable of first generating a driving force for mass transfer. In this case, the driving force for mass transfer is supersaturation as defined in Equation 3.1. Once the driving force is established, the mass transfer event should be initiated by mixing the liquid and measuring the rate at which gas comes out of solution. Without mixing in the liquid phase, gas would only evolve out of the liquid via diffusion through the liquid interface. Stirred vessels have been used extensively to study gas-liquid mass transfer due to their ease of use, though these studies focus almost exclusively on absorption as opposed to desorption (Garcia-Ochoa and Gomez, 2009). For the study of gas evolution within a stirred vessel, several considerations must be taken into account.

5.1.1 Rapid vs Gradual Depressurization

When designing an experiment to test for the rates of gas coming out of solution, the essential feature needed is the ability to generate a supersaturated solution (i.e. driving force) in the liquid with respect to the overhead gas phase. Within a batch system, there are two different routes of accomplishing this. The overhead gas phase can be depressurized in either a rapid or gradual manner. After a saturated gas-liquid solution is formed within a pressurized vessel, rapid depressurization entails opening a valve to the pressurized gas phase and letting some of the gas out quickly. The idea is to approach a perfect step change in the overhead gas phase pressure: the faster the pressure changes from its initial to final value, the better. The quick change in the gas pressure would then instantaneously generate a supersaturated solution within the liquid and initiate gas evolution.

The rapid depressurization technique is used by Hamborg et al. in their absorption-desorption studies of non-reactive fluids (Hamborg et al., 2010). From the data generated, a near instantaneous pressure step change is seen prior to the mass transfer event, though these studies were conducted at near atmospheric pressures. The downside of the rapid depressurization technique is that the maximum pressure drop while maintaining an approximate step change is limited by the tendency of the exiting gas flow to become choked. During choked flow, the gas flow rate becomes independent of the pressure drop between inlet and outlet. Once the flow is choked, increasing the driving force will not alter the flow rate of gas (Winters et al., 2012). The longer it takes for gas to be exhausted, the more the underlying gas evolution signal will become obfuscated. Rapid depressurization should be done very quickly, preferably through a large exhaust outlet. At high pressures, the issue of gas choking during rapid depressurization will only be amplified.

As mentioned in Section 1.1.2, Hunt also performed a rapid depressurization-type experiment using a piston and cylinder setup instead of a typical pressure vessel

(Hunt, 1995). The advantages of the piston-cylinder experiment is that the challenges associated with choked flow are completely avoided. However, the entire piston-cylinder experiment was difficult to construct and the upper pressure limit of the experiment was severely limited due to difficulty maintaining a seal between the piston and the cylinder wall.

The gradual depressurization technique is performed by slowly bleeding off gas from the overhead of an initially saturated solution. If the depressurization rate is low enough, it will not disturb the supersaturated solution as it develops. Once the pressure draw down is complete, the vessel is once again sealed and liquid phase mixing is started to initiate gas evolution. Gas evolution can be monitored by the pressure increase in the overhead gas phase, as with the previous technique. This technique was first exemplified by Schweitzer and Szebehely using a mechanically agitated pressure vessel and a needle valve for slow depressurization (Schweitzer and Szebehely, 1950). While in theory, the maximum allowable supersaturation ratio is only limited by the pressure differential between the vessel and the exhaust, Schweitzer and Szebehely did not attempt to quantify the amount of gas removed, thus making the supersaturated ratio calculation not possible.

In field conditions, a supersaturated solution entering a separator could be potentially generated by via both mechanisms, though the rapid depressurization route is probably more likely to be encountered. A choke upstream of the separator would instantaneously drop the pressure of the inlet gas-liquid stream. Assuming the gas-liquid system is at equilibrium prior to the choke, the resulting pressure drop would instantaneously generate a supersaturated liquid solution with respect to the new overhead pressure. Assuming an ideal gas with a starting pressure of 500 psia, a 50 psi pressure drop through a choke would result in a supersaturated solution of 0.11. This method of supersaturation generation would be akin to the rapid depressurization technique. On the other hand, a supersaturated solution has

the potential to form gradually as well. As the gas-liquid stream flows through a pipe, there will be a naturally occurring pressure drops due to friction in the flow. If the rate of mass transfer in the gas-liquid system is slow enough, the rate of pressure drop could be faster than the system's ability to return to equilibrium, thus generating a supersaturated solution as it flows. This has to potential to occur in more viscous oils, where the pressure drop due to friction is usually higher in a flowing system and the rate of gas-liquid mass transfer is usually lower.

5.1.2 Batch vs Semibatch Operation

When using stirred vessels to measure mass transfer rates, the experiment can be operated in either a batch or semibatch mode of operation (de Lamotte et al., 2017; Linek et al., 2005; Biń, 1984). A semibatch-type experiment involves sparging gas into the bottom of the pressure vessel during the mass transfer measurement, while a batch-type experiment does not have any additional gas flow. While semibatch operation allows mass transfer to occur with a specific rate of entrained gas being introduced into the liquid, the determination of the interfacial area available for mass transfer is challenging. In a large number of studies measuring mass transfer with a sparged gas, it is not possible to deconvolute the mass transfer coefficient from the volumetric interfacial area, as seen in Figure 4.2. As such, the results are not generalizable beyond the confines of the experiment. Due to this limitation, all iterations of the developed gas evolution experiment were performed in a batch-type mode of operation.

5.1.3 Subcritical vs Supercritical Mixing

Within a batch-type experiment, there are two different mixing regimes of interest: subcritical and supercritical mixing (Scargiali et al., 2013). Subcritical mixing refers to mixing performed below the critical mixing point, while supercritical mixing

takes place above the critical mixing point. At an initial low mixing speed within the vessel, the liquid interface will remain flat. As the mixing speed is increased, the liquid interface will begin to deform and form a vortex around the impeller shaft. Eventually with a high enough mixing speed, the liquid vortex will reach the impeller head and begin to disperse gas into the liquid and form bubbles. At this point, the critical mixing speed is reached. As the mixing speed is further increased, the volume of gas being entrained will also increase and the overall size of the entrained bubbles will decrease. The same complications arise during supercritical mixing as seen for semibatch operation, namely the difficulty in measuring the interfacial area.

5.2 Materials

5.2.1 Pressure Vessel

A 1,000 mL pressure vessel was purchased with a pressure and temperature rating of 10,000 psia (68.9 MPa) and 150 °C, respectively. The pressure vessel was manufactured by High Pressure Equipment Company (HIP) and composed of 316 stainless steel. The pressure vessel featured an O-ring closure in combination with a separate metal back-up ring for easy access to the vessel contents through the top of the vessel. The pressure vessel was also equipped with 6 quartz windows located 90°apart from one another. See Figure 5.1 for a schematic of the window placement on the pressure vessel. A heating/cooling circulator jacket was fitted onto the vessel for temperature control.

5.2.2 High-Pressure Pump

A high-pressure dual-cylinder syringe pump manufactured by Teledyne ISCO was used in conjunction with the pressure vessel in order to set up the gas evolution experiment. The pump pressure and temperature rating was 10,000 psia (68.9 MPa) and 200 °C, respectively. Each pump cylinder had a total volume of 100 mL. Due to

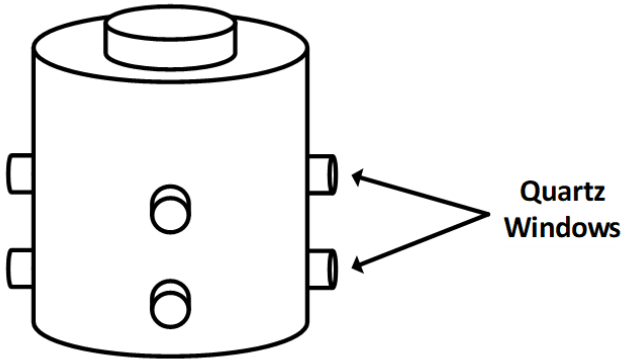

Figure 5.1: Schematic of the window placement on the pressure vessel

the dual-cylinder design, the pump was able to provide a continuous flow of pumped material if needed. The high-pressure pump also came equipped with a controller that allowed the operator to independently adjust each pump.

5.2.3 Mixer

The pressure vessel came equipped with a magnetically driven (MagDrive) mixer and controller. The initial MagDrive assembly had the same pressure and temperature ratings as pressure vessel. The mixer assembly was manufactured by Supercitical Fluid Technologies (SFT) and featured a 1 inch Gaspersinator type impeller used to mix the liquid within the pressure vessel. The mixer controller only allowed for the power to the mixer to be modulated. In order to mix the liquid in the pressure vessel at a certain rpm, power vs rpm correlations were developed for this initial mixer assembly. The impeller shaft often displayed excessive shaft runout and eventually failed in October of 2016 (see Section A.1.14 for a summary of the event). The original MagDrive assembly was replaced with a MagDrive manufactured by Autoclave. The new MagDrive assembly featured instead a 1 inch Rushton turbine. The Autoclave mixer assembly also featured a tachometer built into the mixer head cap, allowing the mixer controller to directly control the impeller speed.

5.2.4 Valves and Actuators

In order to contain the pressure within the experiment, three two-way HIP ball valves are used. The valves are rated up to 15,000 psia (103.4 MPa). To enable remote control of the valves, each valve is mounted with a TruTorq pneumatic actuator. These actuators utilize low pressure instrument air (max 120 psia) to open or close the HIP ball valves. In turn, the actuators are controlled using a LabVIEW data acquisition system set up on the operator's computer. The actuators are configured as air-to-close. In their normal position, the springs within the actuators force the valves open. The instrument air pressure is required for the valves to close. This method of actuator operation was selected so that in case of a failure in the instrument air supply, the valves will default to the open position and depressurize the experiment. All tubing used in the gas evolution experiment is manufactured from HIP, with an outer diameter of 1/8 inch and a pressure rating of 15,000 psia.

5.3 Rapid Depressurization Experiment

The initial conception of the gas evolution experiment focused on the rapid depressurization technique, similar to the mass transfer experiments performed by Hunt and Hamborg et al. (Hunt, 1995; Hamborg et al., 2010). A schematic of the rapid depressurization experiment can be seen in Figure 5.2.

The rapid depressurization experiment was composed of two distinct steps: initial pressure saturation followed by a rapid depressurization event. The pressure vessel was first loaded with a predetermined amount of liquid and then saturated with pressurized gas until the system came to equilibrium. The system was allowed to saturate at an initial saturation pressure for 2 hours with the mixer set to the desired mixing speed. A wait period of 2 hours was found to be sufficient to allow for the system to come to equilibrium. Once saturation period elapsed, the rapid depressurization event was initiated by opening the exhaust valve and venting the

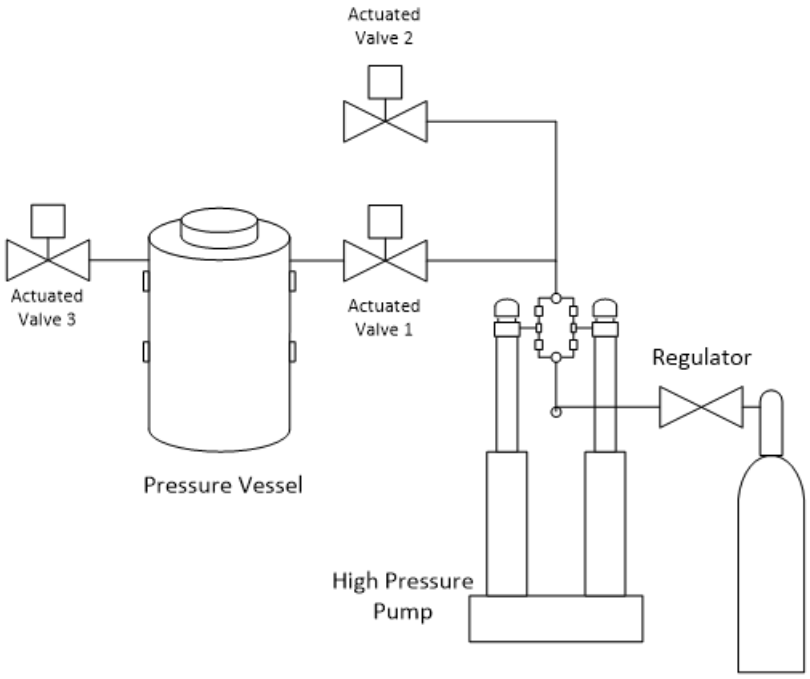

Figure 5.2: Schematic of the rapid depressurization experimental setup

system to the atmosphere. The system is then allowed to return to equilibrium conditions as gas evolved out of solution. The first proof of concept tests utilized 750 mL of water as the liquid phase and compressed air as the gas phase. An example of the resulting rapid depressurization pressure trace can be seen in Figure 5.3.

As previously stated, the aim of the rapid depressurization technique was to approach a step change in the overhead gas pressure as best as possible. With a near instantaneous pressure drop, the pressure within the reactor should increase after the pressure drop as gas is evolving out of solution. As seen in Figure 5.3, the depressurization event does not take more than 10 s, but the increase in the pressure due to gas evolution is indistinguishable from the overall pressure trace. Clearly, the transience associated with the pressure drop were too large for the gas evolution signal to be measured. As the saturation pressure is increased above 200 psia (1.38 MPa), the pressure at which choked flow sets in will also increase. By increasing the pressure of the experiment, the transience due to the choked flow will only become magnified.

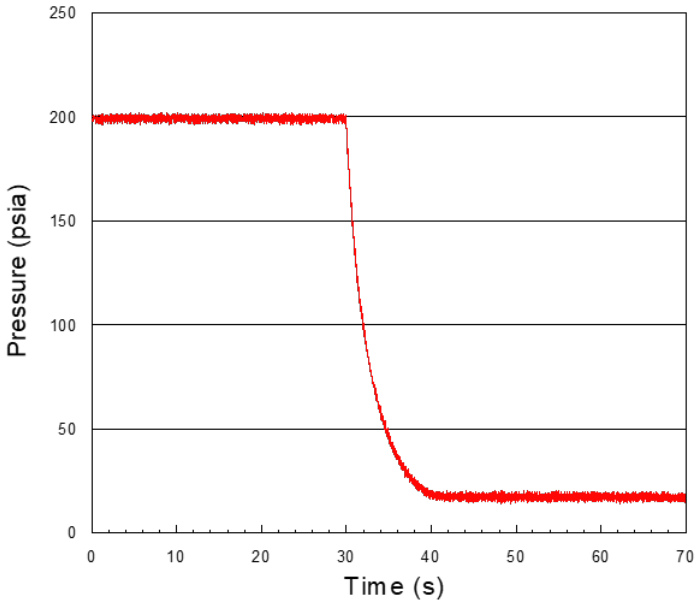

Figure 5.3: Pressure response curve of air-water system at 200 psia, reproduced with permission from Society of Petroleum Engineers (Daniel et al., 2015)

5.4 Gradual Depressurization Experiment

Since the pressure limitations of the rapid depressurization experiment were too constrained for the scope of this project, the experiment was modified to utilized the gradual depressurization technique instead. This experimental setup would then be more similar to the work done by Schweitzer and Szebehely in their gradual depressurization experiment (Schweitzer and Szebehely, 1950). A schematic of the gradual depressurization experimental setup can be seen in Figure 5.4.

The gas evolution experiment was modified by adding another section of tubing connecting the outlet of the prior exhaust valve (valve 3) to the pump inlet. Valve 2 then became the exhaust outlet for the entire system. Using this configuration, the pump can now both pressurize and depressurize the vessel in a controlled manner. By opening valve 1 and closing valve 3, the pump outlet feeds directly into the pressure vessel. To depressurize the pressure vessel, valve 3 is opened while valve 1 is closed. In this configuration, the pump inlet is now drawing from the pressure vessel.

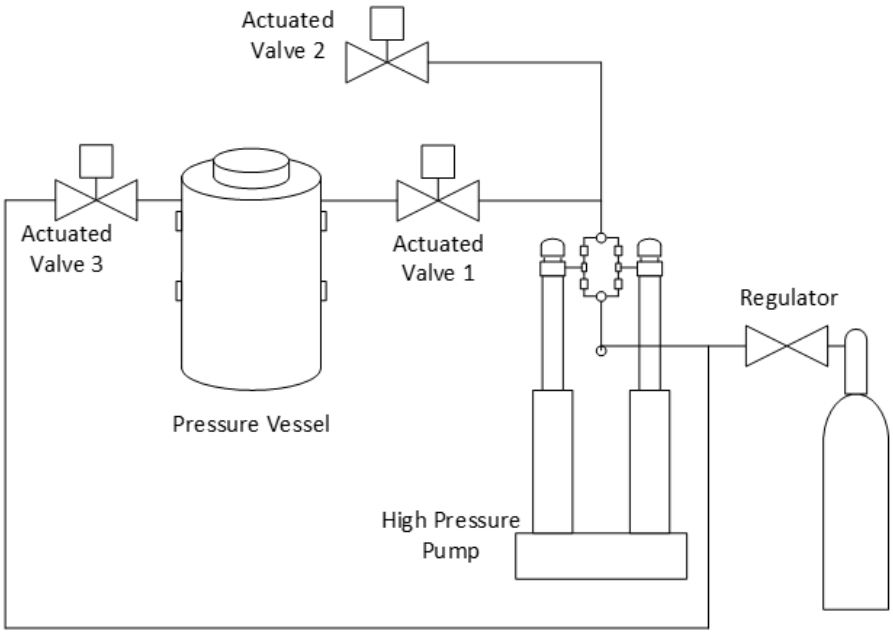

Figure 5.4: Schematic diagram of the gradual depressurization experimental setup

To perform the gradual depressurization experiment, the liquid inside the vessel is initially pressurized using the dual-cylinder continuous flow pump. For this step, valves 2 and 3 are closed while valve 1 is left open. The mixing is then turned on and the overhead gas phase is allowed to solubilize into the liquid. Once all the gas has been solubilized at the desired saturation pressure, the mixing is turned off and the system is allowed to reach equilibrium again. The point at which the solubilization is complete is evaluated by analyzing the change in the pressure slope over time. This pressure slope feature was coded into the LabVIEW data acquisition system. If the pressure slope reaches zero, the pressure is determined to be constant and the gas-liquid system is assumed to be at equilibrium. To gradually depressurize the overhead gas phase, valve 1 is closed and valve 3 is opened. The high-pressure pump is then used to slowly draw in gas from the pressure vessel. In effect, this operation is increasing the total overhead volume, which in turn decreases the gas phase pressure. If this pressure decrease is gradual enough, the liquid within the pressure vessel will

not be disturbed. As the overhead gas phase decreases in pressure, the liquid within the pressure vessel becomes supersaturated. Once the pump depressurization is complete, the gas evolution event is initiated by turning on the mixer and agitating the fluid. Within this closed system, the pressure will then increase as gas comes out of solution. By avoiding the choked flow conditions, the gas evolution measurement is no longer limited by the pressure at which the experiment is being operated.

5.5 Safety

With any high pressure system, safety should always be paramount in the construction, commissioning and operation of the experiment. Throughout the development of the gas evolution experiment, several key safety features have been incorporated into the experimental design and operation. One of the primary safety features is derived from the physical location of the experiment.

5.5.1 Hazardous Reaction Lab

The gas evolution experiment is housed within the Hazardous Reaction Lab (HRL) at Oklahoma State University. The experiment itself is located inside a specially designed blast cell for high energy experiments. A picture of the blast cell exterior can be seen in Figure 5.5. Additionally, a picture of the gas evolution experiment within the blast cell can be seen in Figure 5.6.

The entire gas evolution experiment is controlled remotely from the lab area within the HRL which separates the operator from the experiment via a reinforce concrete wall. The valves are controlled using pneumatic actuators while the pressure and temperature data is logged on the operator's computer within the lab area. The pump controller is also located inside the lab area. The lab area is connected to the blast cell by a series of conduits through which the instrumentation cables are passed. Once the experiment is energized, the operator is prohibited from entering the blast

Figure 5.5: Exterior of the Hazardous Reactions Lab blast cell

Figure 5.6: Gas evolution experiment located inside the blast cell

cell. This segregation of the experimental setup from the lab area greatly reduces the operator's exposure in case of a mishap.

5.5.2 Purging Procedure

Operating with hydrocarbon systems at pressure also introduces the risk of ignition potentially occurring during the experiment. In order to minimize the risk of a flammability event, a purging procedure was instituted to ensure that whenever hydrocarbons were introduced into the experiment the gas concentration within the pressure vessel would always be outside of the explosive range. By controlling the oxygen concentration within the vessel, the explosive risk can be greatly reduced.

The limiting oxygen concentration (LOC) specifies the minimum concentration of oxygen required to produce an explosion of a flammable gas. Below the LOC, explosive conditions cannot be reached no matter what change in the flammable gas concentration takes place. As the total pressure increases, the LOC will also change. For this experiment, however, the total system pressure is increased only by adding the sample gas being tested. If the sample gas tested does not contain oxygen (which is true of all hydrocarbon tests presented here), increasing the total system pressure will cause the percent of oxygen in the gas phase to decrease quickly until it becomes negligible. In order to avoid a potentially explosive environment, the LOC criteria needs to be met only when methane is first introduced into the system.

Figure 5.7 shows an example of the ternary system composed of air, inert gas and the flammable test substance. For this exercise, the flammable gas used will be methane. Methane is also the gas phase used in all the hydrocarbon experiments presented in Chapters 6 and 7. The lowest point of encroachment of the explosion area, bounded by the lower explosive limit (LEL) and upper explosive limit (UEL), into the required concentration of oxygen is what dictates the LOC. In Figure 5.7, the limiting air concentration (LAC) is shown instead of the LOC. The LAC can be

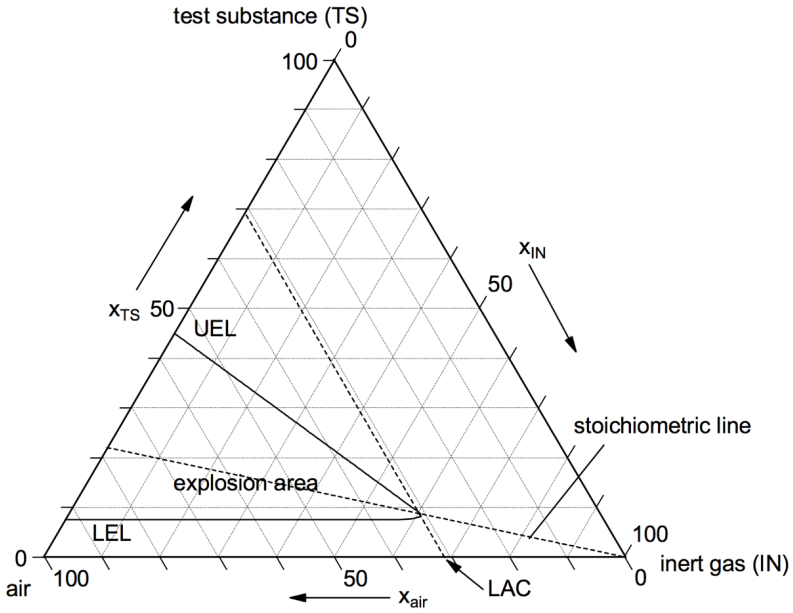

Figure 5.7: Example of ternary diagram of flammable gas system (Holtappels et al., 2011)

easily converted to the LOC by multiplying the LAC by the molar concentration of oxygen in air, 0.209.

Figure 5.8 shows the change in explosion area for a methane fuel system in air and nitrogen as pressure is increased up to 100 bar. While there is a significant increase in the total bounded area, the LAC and subsequent LOC decreases only by a small amount at 100 bar (53 mol% in air) when compared to the value at 1 bar (55 mol % in air). The LAC actually increases up to 60 mol% in air at 10 bar. Once the experiment is pressurized up to 100 bar with methane, the oxygen concentration inside the vessel would already be negligibly small (0.0021 mol%).

In order to purge the pressure vessel and decrease the total oxygen concentration prior to the introduction of hydrocarbons, an inert gas phase is required. Pure nitrogen is used as the inert gas for the experiments presented here. In order to successfully purge the system with nitrogen, there are two potentially viable methods of accomplishing this: pressure purging and sweep-through purging. Pressure purging involves closing the atmospheric outlet and filling the system with inert gas. The

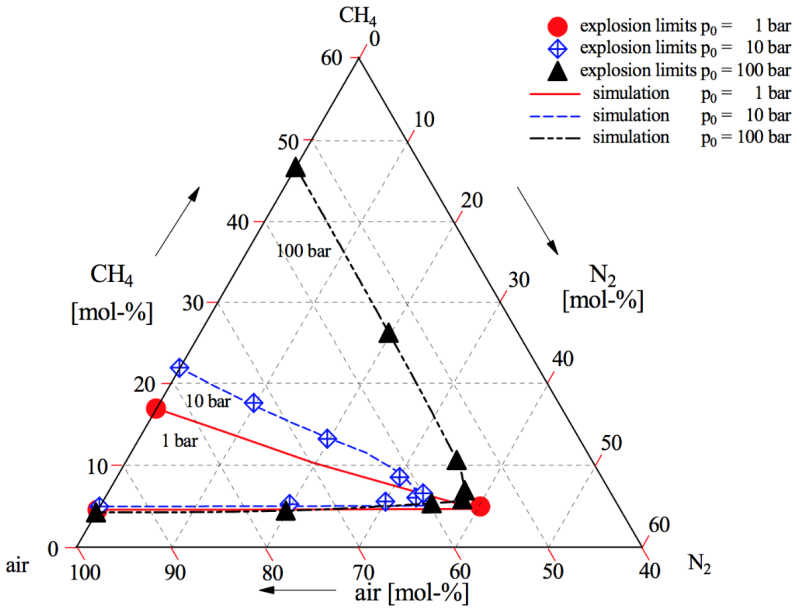

Figure 5.8: Ternary system with explosion limits at various pressures for air, nitrogen and methane (Holtappels et al., 2011)

outlet is then opened to relieve the pressure, removing some amount of residual air in the process. This pressurization and discharging procedure is repeated until the internal gas composition reaches the desired level. During pressure purging, it is important to let the pressurized system to sit for some period of time to ensure that all the internal gases have had the chance to mix. Sweep-through purging, on the other hand, involves displacing internal air by maintaining a continuous flow of inert gas through the system for some period of time. While in principal the execution of the sweep-through purging is simpler, non-idealities in the gas mixing become an issue in reliably predicting resulting gas concentrations. Since the inlet and outlet orifices within the pressure vessel are placed directly opposite one another, it seems very probable that there would be a significant amount of flow short-circuiting leading to poor internal mixing in the vessel internals. As such, the pressure purging is the adopted purging method.

While LOC test results vary with specific vessel geometries, ignition criteria, etc., Zlochower and Green complied LOC values from a variety of different tech-

niques for methane with nitrogen as the inert gas. These LOC values for methane ranged from 12.0 to 10.7 mol% (Zlochower and Green, 2009). In the interest of being conservative the lowest LOC value, 10.7 mol%, will be used.

Assuming the gases behave ideally, the initial number of oxygen moles in the system can be calculated using

$$n_{z=0} = \frac{P_{atm}V}{RT} \tag{5.1}$$

$$n_{\mathrm{O}_2,z=0} = x_{\mathrm{O}_2} n_{z=0} \tag{5.2}$$

where x_{O_2} is the molar concentration of oxygen in air and the subscript z refers to the number of times the purging cycle has been performed ($z = 0$ refers to the system prior to any inert gas purging taking place). Assuming isothermal conditions and no oxygen in the inert gas, the total moles and oxygen concentration in the pressurized system can be calculated using

$$n_{z=1} = \frac{P_{inert}V}{RT} \tag{5.3}$$

$$x_{\mathrm{O}_2,z=1} = \frac{n_{\mathrm{O}_2,z=1}}{n_{z=1}} = \frac{x_{\mathrm{O}_2} P_{atm}}{P_{inert}} \tag{5.4}$$

where P_{inert} is the pressure at which the inert gas is being delivered and P_{atm} is the atmospheric pressure. The above calculation can be repeated multiple times for multiple pressure purging cycles. If the nitrogen is delivered at 200 psig, the resulting oxygen concentration in the vessel would be

$$x_{\mathrm{O}_2,z=1} = \frac{0.209 \cdot 14.7\mathrm{psia}}{214.7\mathrm{psia}} = 0.014 \tag{5.5}$$

The resulting molar concentration of oxygen after one pressure purge with

nitrogen at 200 psig would be an entire order of magnitude lower than the LOC for methane. This significantly simplifies the purging process since only one purging cycle would be required before methane is introduced while at the same time providing for a large margin of safety in the resulting oxygen concentration. This purging procedure with nitrogen is performed prior to each gas evolution experiment when hydrocarbons are being tested.

5.5.3 Blast Cell Blower

The blast cell is equipped with an exhaust blower to circulate air through the confined area within the blast cell (located on the top right of the blast cell entrance, as seen in Figure 5.5). The blower has an airflow capacity ranging from 1,390 to 1,640 ft^3/min (39.4 to 46.4 m^3/min). Measuring the blast cell volume to be 585 ft^3 (16.6 m^3), the number of air changes per minute is conservatively estimated to be 2.4 min^{-1}. In the event of a catastrophic failure in the pressure containment, the potential worse case scenario involves 1 L of methane pressurized at 10,000 psia (68.9 MPa) being discharged into the confinements of the blast cell. With that quantity of methane assumed to be immediately released, the resulting methane concentration in the blast cell would be 4.1 mol%. This potential worse case methane concentration is still below the LOC value of 10.7 mol%. This calculation, however, assumes that the released methane is instantaneously mixed into the air. Local methane concentrations could still potentially be above the LEL. With 2.4 volume equivalent changes per minute, the exhaust blower capacity should be more than enough to prevent a potentially explosive environment from forming within the blast cell. Prior to each gas evolution experiment, the blast cell blower is turned on and left in operation until the entire experiment is concluded.

5.5.4 Hydrocarbon Sensors

Hydrocarbon sensors were also introduced to alert operators in the event of a hydrocarbon leak. Prior to each experiment, the rechargeable hydrocarbon sensors were distributed to their designated positions. One sensor was placed inside the blast cell directly above the pressure vessel, one was placed on the exterior of the blast cell next to the gas cylinders, and the third was clipped directly onto the operator. In order to prevent premature wearing, each of the hydrocarbon sensor's designated position was regularly rotated. Since the hydrocarbon sensors did not rely on the building power, they would still be operational in the event of a power outage.

5.5.5 Emergency Shutdown

The experiment was designed around a simple emergency shutdown procedure. All the electronics in the lab area were plugged into a single power bank. By turning off this power bank, all the experimental functionality would immediately cease and the actuated valves containing the pressure would open. Additionally, the gas cylinder used for the low pressure instrument air is also located inside the lab area (no other gas cylinders are located inside the lab). By closing this gas cylinder, the pressure supply to the actuators ceases and the air-to-close actuators will return to the open position. In the event of an emergency shutdown, closing the gas cylinder ensures that the experiment will not become accidentally blocked in, potentially endangering an operation that would need to enter the blast cell to correct the issue.

5.6 Summary

By modifying the initial rapid depressurization experimental design, the pressure limitation on the gas evolution measurement was circumvented. Using the newly developed gradual depressurization experimental design, the gas evolution experiment was then tested over a range of different pressures, mixing speeds and gas-liquid com-

binations to ensure that the experiment was performing as expected. Additionally, the safety procedures developed in this chapter were utilized for all gas evolution trials going forward.

CHAPTER VI

GAS EVOLUTION EXPERIMENTS

With the newly developed gradual depressurization technique, the experiment was carefully tested over a variety of different conditions to ensure that the mass transfer measurement was both reliable and repeatable. The results of the gas evolution experimental validation are shown here.

6.1 Gas Evolution Experimental Procedure

The gas evolution experiment can be broken up into four distinct steps: initial pressurization, solubilization, depressurization, and gas evolution. Prior to starting the experiment, the pressure vessel is loaded with the desired sample liquid. All trials presented here use 500 mL of sample liquid. The circulator is then turned on and the vessel is allowed to reach the required liquid temperature before proceeding with the experiment. Referring to the experiment schematic in Figure 5.4, the experiment is set up for the initial pressurization step by closing valves 2 and 3 while opening valve 1. Starting the gas phase pressure and temperature data logging, the sample gas regulator is opened and the pump is used to pressurize the vessel up to the desired pressure. Once the pumping is finished, the pump cylinders are adjusted so that both cylinders are completely discharged. The sample gas regulator is also closed. Prior to starting the solubilization step, valve 1 is closed and valve 3 is opened.

In order to start the solubilization step, the mixing is turned on and the solution is allowed to solubilized until the gas-liquid system within the pressure vessel reaches equilibrium. Once at equilibrium, the mixing is turned off and the system is

allowed once again to reach equilibrium. At this point, the pressurized liquid within the vessel is in a quiescent state. Next the depressurization step is initiated by setting each pump cylinder to a refill rate of 1.2 mL/min. Since valve 1 was closed and valve 3 was opened in the prior step, the pump now draws in gas from the pressure vessel. For the fluids tested here, the refill rate of 1.2 mL/min was found to be slow enough to avoid disturbing the quiescent fluid. At an initial pressure of 300 psia (2.07 MPa), this depressurization rate results in an average pressure drop of around 1 psia/min (6.9 kPa/min).

Once the depressurization step is completed and both pumps completely refilled, the gas evolution experiment is initiated by turning on the mixer at the desired mixing speed. Gas is allowed to evolve out of solution until the system once again reaches equilibrium. Once this step concludes, the data logging is stopped and the experiment is depressurized. For an example of the overall pressure trace during the gas evolution experiment, see Figure 6.1.

6.2 Data Analysis

Calculating the total molar change during gas evolution requires an accounting of all gas moles initially introduced into the system. The total number of moles in the gas phase during the initial pressurization step can be calculated by adding the total moles pumped into the experiment to the number of moles already in the vessel overhead at atmospheric conditions

$$n_{total} = n_{pump} + n_{atmosphere} \tag{6.1}$$

where the total number of moles pumped into the system is calculated using

$$n_{pump} = f(EOS(P_{pump}, T_{pump}), V_{pump}) \tag{6.2}$$

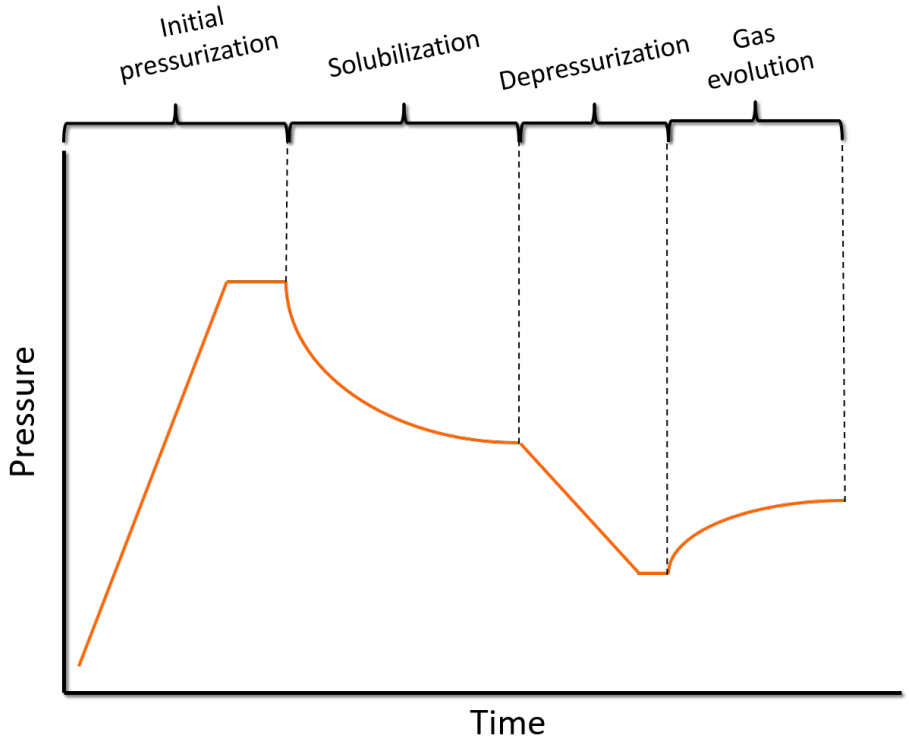

Figure 6.1: Example pressure trace for a gas evolution experiment

The pump is initially being fed by the sample gas cylinder. The pressure, P_{pump}, and temperature, T_{pump}, at which the sample gas is being pumped is used in conjunction with an equation of state to calculate the molar density of the gas at those conditions. The molar density can then be multiplied by the volume of the gas pumped, V_{pump}, to calculate to total number of moles feed into the system. For trials using air as the gas phase, the NIST reference equation of state for air was used (Lemmon et al., 2000). For trials using methane, the NIST reference equation of state for methane was used (Setzmann and Wagner, 1991).

The total moles dissolved into solution after solubilization step is completed can be calculated using

$$n_{\mathrm{l},0} = n_{total} - n_{\mathrm{g},0} \tag{6.3}$$

where the subscript 0 refers to the initial solubilized state. The moles in the overhead

gas phase at the initial solubilized state, $n_{g,0}$, is calculated using

$$n_{g,0} = f(EOS(P_{g,0}, T_{g,0}), V_{overhead}) \tag{6.4}$$

The overhead volume is calculated by subtracting the pressure vessel volume from the total volume of liquid within the pressure vessel. At the supersaturated state, the moles in the overhead gas phase can be calculated using

$$n_{g,SS} = f(EOS(P_{g,SS}, T_{g,SS}), V_{overhead} + 200 \text{ mL}) \tag{6.5}$$

The subscript SS refers to the supersaturated state of the experiment. To check that there has not been significant gas evolution (background diffusion) occurring during the pump depressurization, the moles in the overhead gas phase before and after depressurization can be compared to one another. The difference between these two values is less than 1% when minerals oils are being used as the liquid phase.

Finally, the moles of gas dissolved at the start of gas evolution step is calculated using

$$n_{l,SS} = n_{l,0} - (n_{g,SS} - n_{g,0}) \tag{6.6}$$

By subtracting the absolute change of moles in the overhead gas phase during gas evolution from the initial number of gas moles dissolved prior to gas evolution, the remaining moles dissolved in solution can also be calculated.

6.3 Mineral Oil Properties

The fluids used in the gas evolution experiments presented here consist of two different mineral oils: Tech 80 and Tech 500. Both mineral oils are manufactured by Tulco Oils. The findings presented by Schweitzer and Szebehely indicate that the liquid phase viscosity is a key variable governing gas evolution (Schweitzer and

Szebehely, 1950). As such, the two model oils selected had roughly an order of magnitude difference in the liquid phase viscosities. The physical properties for both the mineral oils are listed in Table 6.1. While the viscosities of the two mineral oils differ significantly, the measured surface tensions are very close to one another. This indicates that the surface properties are similar for the two mineral oils.

Table 6.1: Physical properties of Tech 80 and Tech 500 at 25 °C

	Viscosity [cP]	Surface Tension [mN/m]	API Gravity
Tech 80	18	30.7	31.3
Tech 500	191	32.6	30.9

6.4 SFT Mixer

As previously mentioned in Section 5.2.3, the original mixer that came with the pressure vessel was manufactured by Supercitical Fluid Technologies (SFT). The SFT mixer controller did not allow the mixing speed to be directly controlled, instead the controller simply modulated the power sent to the mixer. In order to relate the mixing power to the mixing speed, a correlation was formed between the two variables from a bench-top test. For this test, the mixing speed was measured using a hand-held tachometer. The results of this correlation can be seen in Figure 6.2. The mixing speed was found to vary linearly with the power sent to the mixer in both water and the viscous Tech 500 mineral oil.

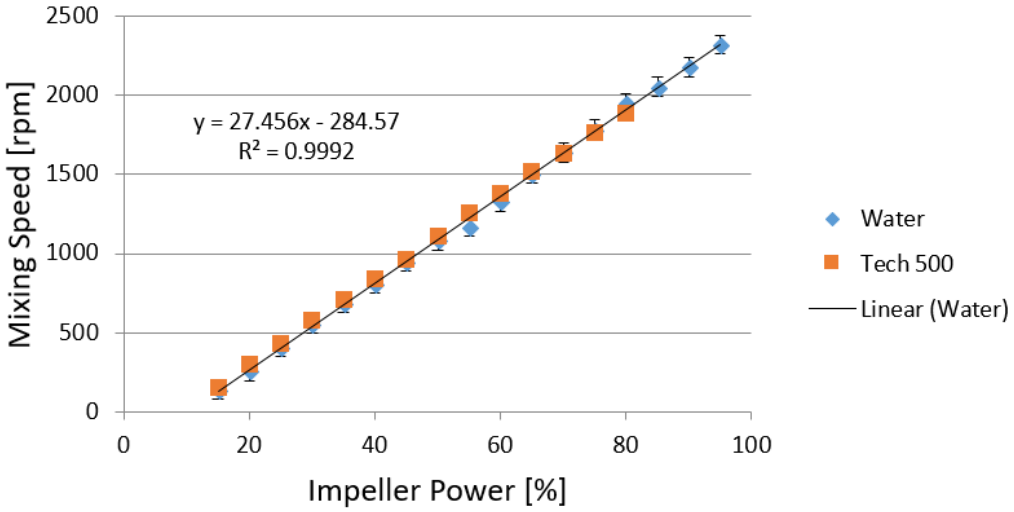

Figure 6.2: SFT mixer power correlation

6.4.1 Initial Results

The initial gas evolution tests were conducted using both Tech 80 and Tech 500 as the liquid phase and air as the gas phase. A comparison between the gas evolution profiles of both mineral oils at two different mixing speeds can be seen in Figure 6.3

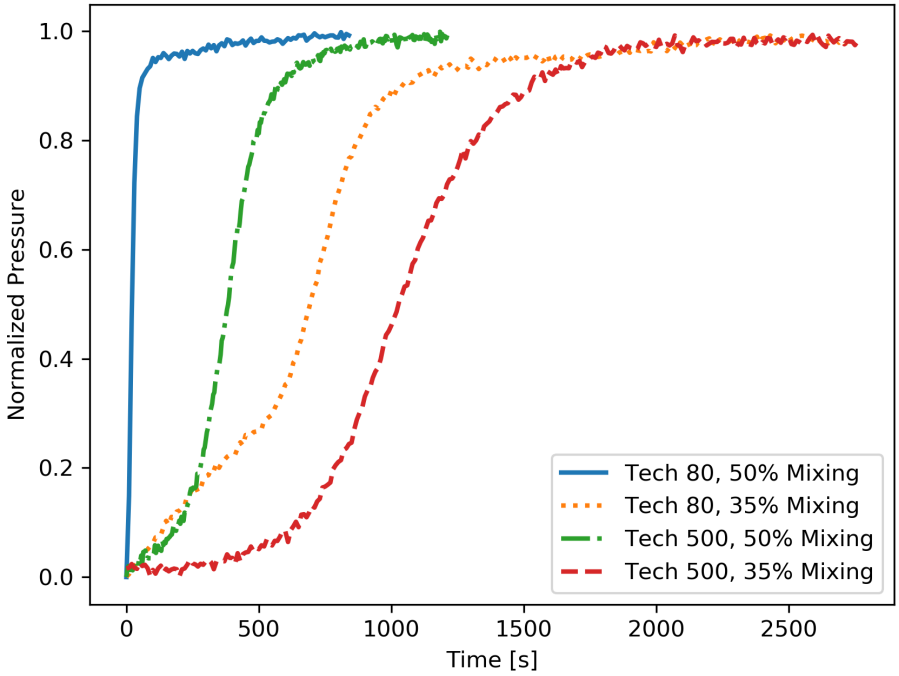

Figure 6.3: Effect of viscosity and mixing on gas evolution at 500 psia and 25 °C

The gas evolution pressure measurements were normalized using

$$P_{\text{norm}} = \frac{P - P_{\text{initial}}}{P_{\text{final}} - P_{\text{initial}}} \tag{6.7}$$

At the same mixing level, the more viscous mineral oil (Tech 500) evolved gas slower than the less viscous mineral oil (Tech 80). This result is in agreement with the data presented by Schweitzer and Szebehely (Schweitzer and Szebehely, 1950). Also, as the mixing level is increased, the rate at which gas evolves out of solution is also increased.

While performing the initial gas evolution experiments, trial replicates resulted in poor reproducibility. These trials were performed at the same mixing speed, liquid temperature, initial saturation pressure, and using the same gas-liquid system. Even though the same mixing speed was used, it was suspected that the liquid mixing was not consistent from trial to trial. From the bench-top mixing calibration tests, the

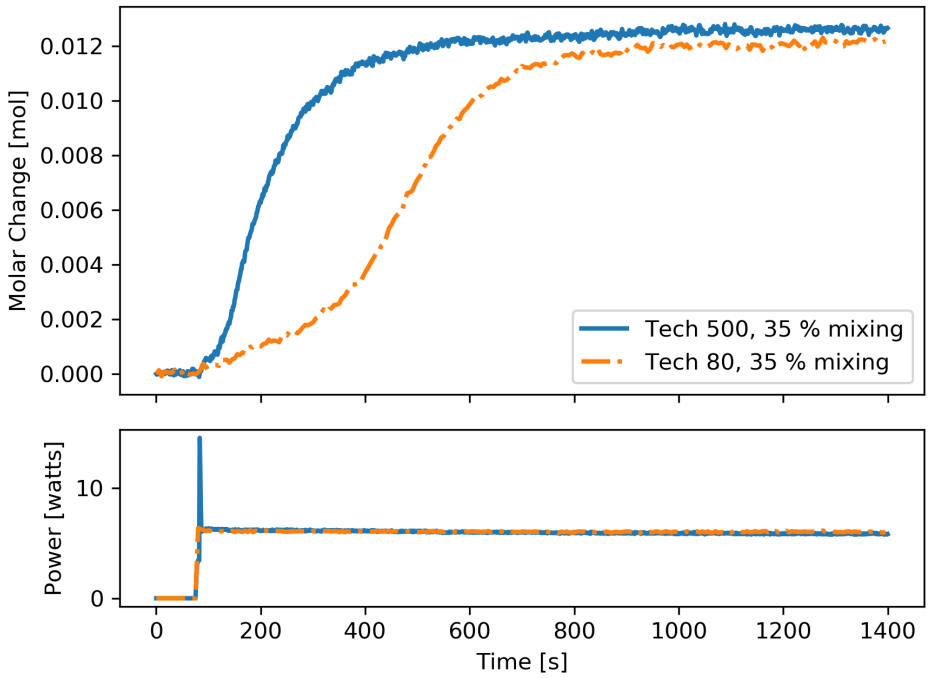

Figure 6.4: Gas evolution with SFT mixer and mixing power measurement at 500 psia and 10 °C

SFT mixer was known to display excessive shaft runout (wobbling of the shaft) on occasion. The shaft runout would occur randomly during regular operation. Increased mixing speeds would further increase the likelihood of shaft runout occurring. In order to further investigate this phenomena, an ammeter and voltmeter were connected to the mixer power supply and the power to the mixer was measured during gas evolution. As with the gas evolution pressure response, the calculated molar response during gas evolution can be plotted against time and compared to the mixing power measurement at the same time scale. Figure 6.4 shows an example of this comparison with gas evolution occurring in Tech 80 and Tech 500 at 10 °C.

The more viscous Tech 500 is expected to evolve gas slower than Tech 80. This is, however, not the case presented in Figure 6.4. Tech 500 exhibits a faster rate of gas evolution compared to Tech 80 at the same mixing speeds. Another interesting discrepancy between the two trials arises from the mixing power measurement. At

$t = 0$, the mixer is initially off for both trials. The gas evolution step is then initiated by turning on the mixer at roughly 75 s for both trials. While the mixing power set point is set to 35% in both cases, the measured mixing power in the Tech 500 trial exhibits a large initial spike compared to the Tech 80 mixing power. The Tech 500 mixing power then rapidly converges to the same level as the Tech 80 mixing power. This initial spike in the mixing power was likely due to excessive shaft runout right as the mixer was turned on. This sudden burst of increased mixing was hypothesized to lead to a faster rate of gas evolution compared to what otherwise would have been expected.

Another example of erratic mixing behavior can be seen in Figure 6.5. Here a trial replicate is being performed with Tech 500 at 25 °C and a mixing power set to 35%. Both measured mixing powers spiked during gas evolution, but not the same time. The mixing power of the first gas evolution trial (blue) initially spiked and maintained a mixing power above the usual level for around 400 s. The mixing power of the second gas evolution trial (orange) spiked roughly 100 s after the first trial and maintained an abnormal level throughout the rest of the gas evolution experiment. Even though both trials exhibited a spike in the mixing, the earlier spike in the first gas evolution trial significantly increased the rate of gas evolution compared to the second trial.

From these results, it was apparent that the irreproducibility between trial replicates was due to erratic mixing occurring randomly throughout the experiment. Soon after the mixing power measurement was installed, the SFT mixer failed due to excessive shaft runout. A summary of the impeller shaft failure can be found in Section A.1.14.

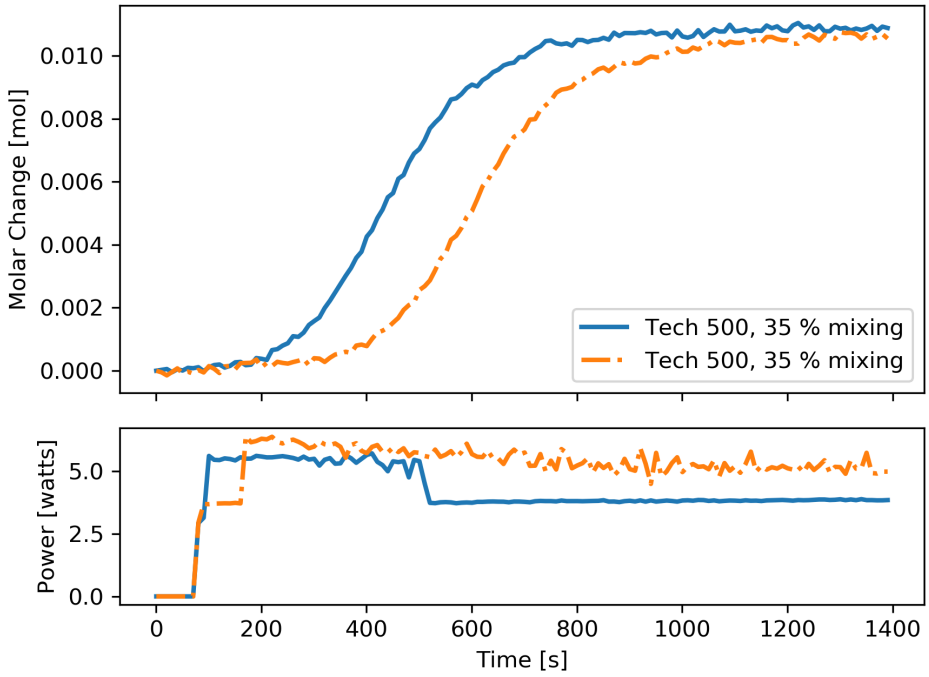

Figure 6.5: Gas evolution trial replicate of Tech 500 with SFT mixer and mixing power measurement at 500 psia and 25 °C

6.5 Autoclave Mixer

The SFT mixing assembly was replaced with a MagDrive mixer and controller manufactured by Autoclave. The new mixer came with a guaranteed shaft runout of less that 0.0005 in/in shaft. The Autoclave mixer also featured a tachometer built into the mixer head cap, enabling the controller to read the mixer speed in real time and modulate the mixing power to ensure the mixing speed set point is always maintained. Mixing rpm is now used as the controller input instead of the percent mixing power.

6.5.1 Results

In order to ensure that the new Autoclave mixer was performing as expected, several trial replicates were run with each model oil using methane as the gas phase. Figure 6.6 shows the gas evolution molar change of three different trials in Tech 80 at a mixing speed of 500 rpm. The gas evolution molar response was normalized using the same method described in Equation 6.7. The trial half-lives, that is the time required for half of the gas to evolve out of solution, were within 290 s of one another. For all three trials, the initial gas evolution profiles overlapped. The second trial, however, exhibited a small positive deviation at later times compared to the other two trials. This deviation was due to a higher ambient temperature for that particular day. While the liquid temperature within the pressure vessel is controlled using the circulator connected to the vessel jacket, the overhead gas phase temperature cannot be explicitly controlled within the experiment. The entire pressure vessel is wrapped in insulation to decrease the impact of the ambient temperature on the sample gas phase temperature. For the gas evolution experiments presented here, the gas phase temperature is always within 2 °C of the liquid temperature set point.

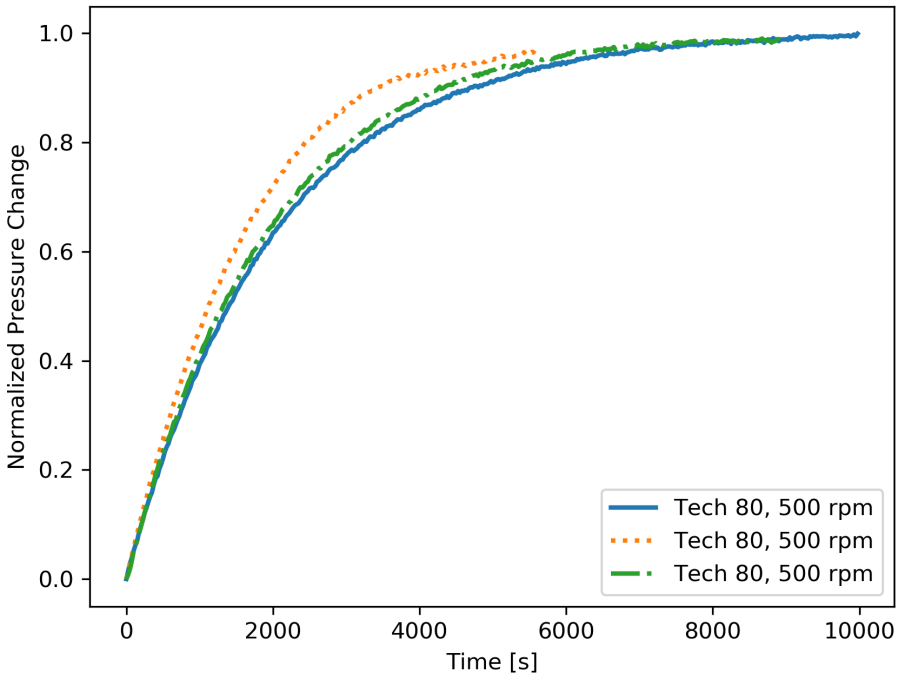

Figure 6.6: Gas evolution trial replicate of Tech 80 with Autoclave mixer at 25 °C

Figure 6.7 shows similar repeatability in the gas evolution measurement as seen in Figure 6.6. In Figure 6.7, three gas evolution trials were conducted using methane in Tech 500 at a mixing speed of 500 rpm. For these trials, all three gas evolution profiles are essentially identical. The measured trial half-lives were within 77 s of one another. The results shown in Figures 6.6 and 6.7 demonstrate that the experiment equipped with the Autoclave mixer is capable of generating repeatable gas evolution measurements.

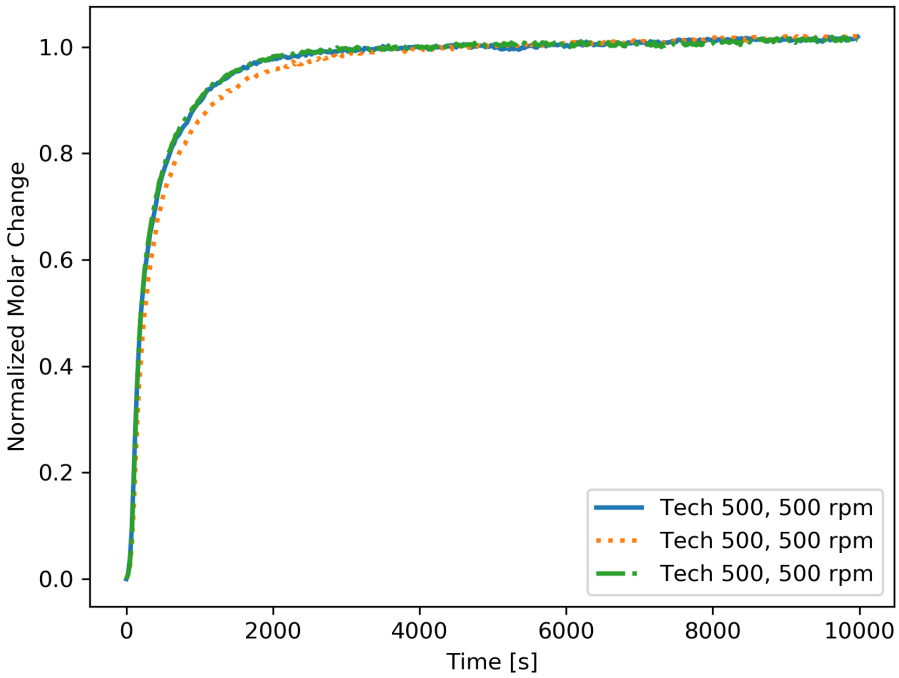

Figure 6.7: Gas evolution trial replicate of Tech 500 with Autoclave mixer at 25 °C

6.6 Summary

As shown here, the quality of the liquid mixing is an important factor to consider when measuring rates of gas evolution. The original SFT mixer would have needed to be replaced if it had not failed first. With confirmation that the gas evolution measurements can be conducted in a repeatable manner using the new Autoclave mixer, the next step in the experimental validation is ensuring that bubble nucleation is not significantly affecting the gas evolution measurements. For these trials, higher pressures will also be explored.

CHAPTER VII

ABSORPTION-DESORPTION EXPERIMENTS

Using the gradual depressurization experimental design described in the previous chapter, the gas evolution procedure can be modified to further validate this method of measuring mass transfer. Both the rates of absorption and desorption (gas evolution) can be measured for the same trial at the same process conditions. By interpreting the experimental output within a mass transfer framework, both the absorption and desorption mass transfer coefficients can be calculated and compared to one another. While these coefficients are expected to be equal for the same process conditions, experimental confirmation of this symmetry will further validate the developed gas evolution experimental design.

7.1 Absorption vs Desorption

The gas-liquid mass transfer framework presented in Section 4.1 is applicable in theory for both absorption and desorption (the direction of the flux should not matter). Rates of absorption and desorption are often assumed to be identical for the same temperature, pressure, and hydrodynamic conditions (de Lamotte et al., 2017). A potential source of asymmetry when comparing absorption and desorption mass transfer coefficients comes from the possibility of bubble nucleation. As seen in Section 3.1, bubble nucleation has the potential to occur in supersaturated solutions with relatively low supersaturation ratios. This potential for bubble formation is not present during absorption since the driving force for mass transfer is into the liquid, not out of it. During desorption, nucleating bubbles will provide additional

interfacial surface area available for mass transfer. If this additional surface area is not accounted for, the resulting desorption mass transfer coefficient will appear to be artificially increased compared to absorption at the same conditions.

In order to validate the developed experimental setup and confirm that bubbles are not forming during desorption, both rates of absorption and desorption will be measured for the same physical and hydrodynamic conditions. Experimental validation of this symmetry is extremely limited in the open literature. Of the absorption-desorption studies that exist, the rates of mass transfer were measured at near atmospheric conditions (Hamborg et al., 2010). Verification of this absorption-desorption symmetry has not been performed at high pressures using a bulk liquid and gas phase.

7.2 Mass Transfer Modeling

The rate of mass transfer is known to be a function of the physical properties of the gas and liquid phases as well as the hydrodynamic conditions. In order to account for the influence of these factors on mass transfer, the measured mass transfer coefficients are typically correlated within a stirred tank experiment using the dimensionless Sherwood correlation (Gilliland and Sherwood, 1934; Sherwood et al., 1975)

$$Sh = c_1 + c_2 Re_{\mathrm{s}}^{c_3} Sc^{c_4} \tag{7.1}$$

where Re_{s} is the stirred tank Reynolds number is defined using

$$Re_{\mathrm{s}} = \frac{\rho_{\mathrm{l}} \omega d_{\mathrm{i}}}{\mu_{\mathrm{l}}} \tag{7.2}$$

where ω is the impeller mixing speed. The Schmidt number is defined in Equation 4.17, and the Sherwood number is defined using

$$Sh = \frac{k_{\mathrm{l}} d_{\mathrm{i}}}{D} \tag{7.3}$$

where d_{i} is the impeller diameter. The constants c_1, c_2, c_3, and c_4 are used to fit the experimentally measured data to the above correlation. The drawback of this approach to mass transfer modeling is that the constants used for the fitting are dependent on the geometries of the stirred vessel, impeller, and liquid height. The resulting Sherwood correlation is not generalizable for predicting mass transfer rates in different systems. Since the goal of this work is to use mass transfer data measured within a stirred vessel for gas-liquid separator design, this method of correlating the data is not useful and therefore, will not be employed. Instead, theoretically derived mass transfer expressions, such as those listed in Section 4.2.5, will be evaluated for their ability to describe the data.

7.3 Experimental Description

The experimental setup utilized the same 1 L high-pressure stirred vessel and pump, seen in Figure 5.4. In order for absorption and desorption rates of mass transfer to be comparable, the same temperature, stirring speed, liquid volume in the vessel and initial saturation pressure of the gas were used for each absorption and desorption measurement of the same trial.

7.3.1 Test Conditions

For the mass transfer experiments presented here, a reference hydrocarbon system of high purity methane and n-dodecane were used as the gas and liquid phases, respectively. All trials were run with a liquid volume of 500 mL. Three different saturation pressures, 500, 1,000, and 1,500 psia (3.45, 6.89, and 10.3 MPa) were tested. The liquid temperature was kept constant at 45 °C. The physical properties of the system at these temperatures and pressures are listed in Table 7.1. Additionally,

Table 7.1: Liquid density and viscosity of n-dodecane and methane diffusivity in n-dodecane at 45 °C as a function of pressure (Jamialahmadi et al., 2006)

P [psia]	ρ_l [kg/m^3]	μ_l [Pa · s]	D [m^2/s]
500	661.7	3.12	7.93
1000	651.6	3.05	8.10
1500	641.4	2.83	8.73

the mass transfer studies conducted here are all performed at mixing levels that maintained a flat gas-liquid interface. By maintaining the mixing levels below the point of visually deforming the interface, the area available for mass transfer was quantifiable for all trials. By testing the mixer in dodecane on the lab bench, the maximum mixing speed resulting in no visual deformation was found to be 350 rpm. In order to establish a reasonable margin of error, the maximum mixing speed during the experiment was limited to 250 rpm.

7.4 Absorption-Desorption Experimental Procedure

The absorption-desorption experiment can be broken up into four distinct steps: initial equilibrium, absorption, second equilibrium, and desorption. To initiate an experiment, dodecane is first loaded into the pressure vessel, the circulator is turned on, and the liquid inside the vessel is allowed to reach the required temperature. Initially the pump positions are staggered: the first pump cylinder is completely filled while the second pump cylinder is completely discharged. Referring to the experiment schematic in Figure 5.4, valve 2 is closed and the system is pressurized using the sample gas cylinder. In order to conclude the initial equilibrium step, the mixer is turned on and the system is allowed to reach equilibrium. Once the initial equilibrium is reached, the mixer is turned off and the system is left to reach equilibrium once again. At this point, the liquid within the vessel is in a quiescent state.

In order to initiate the absorption step, the first syringe pump cylinder (initially full) is discharged resulting in an increase in the overhead pressure. By increasing the

overhead pressure, the liquid becomes undersaturated with respect to the new higher overhead pressure. Once the pump cylinder is completely dispensed, the absorption mass transfer is initiated by turning on the mixer at the desired mixing speed. As gas is absorbed into the now undersaturated liquid, the overhead pressure decreases. The system is then allowed to reach equilibrium once again.

After the absorption step is completed, the mixing is stopped, and the discharged pump cylinder (first pump cylinder) is then refilled again with gas from the pressure vessel overhead. This refilling of the pump cylinder causes the overhead pressure to decrease. Once the first pump cylinder is totally refilled, the mixing is then started again and the system is allowed to reach equilibrium. Once equilibrium is reached with the mixing on, the mixer is then turned off and the system is allowed to reach equilibrium once again as the liquid becomes quiescent. This step then returns the gas-liquid system back to the same equilibrium state prior to starting the absorption mass transfer step. Once finished, the second equilibrium step in the experiment is concluded.

In order to start the final desorption step, the second syringe pump cylinder (originally totally discharged) is refilled at the same rate of volume change used for the absorption step. This results in a decrease in the overhead pressure, causing the liquid to become supersaturated with respect to the overhead gas phase. Once the second pump totally refilled, the mixing is again turned on at the same speed used during the absorption experimental step and system is left until the desorption is complete. An example of a complete absorption-desorption experiment pressure trace and resulting change in liquid concentration can be seen in Figure 7.1.

The rate of pumping determines the rate at which the driving force for mass transfer is generated. For the absorption step, generating the undersaturated solution is dependent on the rate of volume dispensing. For the desorption step, generating the supersaturated solution is dependent on the rate of volume refilling. Care was

taken in selecting an appropriate rate of volume change for the pumps in both mass transfer steps (dispensing and refilling). If the rate of volume change selected for the pump was too large, the quiescent liquid may become disturbed, disrupting the generation of the mass transfer driving force. On the other hand, if the rate of volume change selected was too low, background solute-solvent diffusion occurring during the pumping process would significantly decrease the final mass transfer driving force.

A pump volume change of 20 mL/min was found to produce reliable results for this methane-dodecane system. Four of the trials presented here were, however, run using a suboptimal pump volume change of 1.2 mL/min (the same rate of volume change used in the gas evolution experiments in Chapter 6). For the methane-dodecane system, this lower rate of volume change resulted in the occurrence of significant background diffusion during pumping, thus decreasing the final driving force for mass transfer. While this did not significantly alter the rate at which mass transfer occurred, the absorption and desorption mass transfer coefficients were measured from a smaller driving force, decreasing the signal to noise ratio in the measurement, resulting in slightly larger associated error bars. A comparison of all measured mass transfer coefficients along with their associated error bars can be seen in Figure 7.19.

The reason that the desorption portion of the experiment is not performed immediately after the absorption step is due to the different starting liquid concentration. Since the liquid properties affect the rate of mass transfer and these properties change with different solute concentrations, it is important to ensure that the starting concentration prior to absorption or desorption is as close as possible if the two values are to be comparable. Returning to Figure 7.1, after the absorption step the liquid concentration is obviously higher than it was prior to the absorption commencing. By performing the second equilibrium step, the liquid concentration is brought down back to its initial position and the desorption step is then performed from there. For a detailed description of the standard operating procedure, see Appendix A.

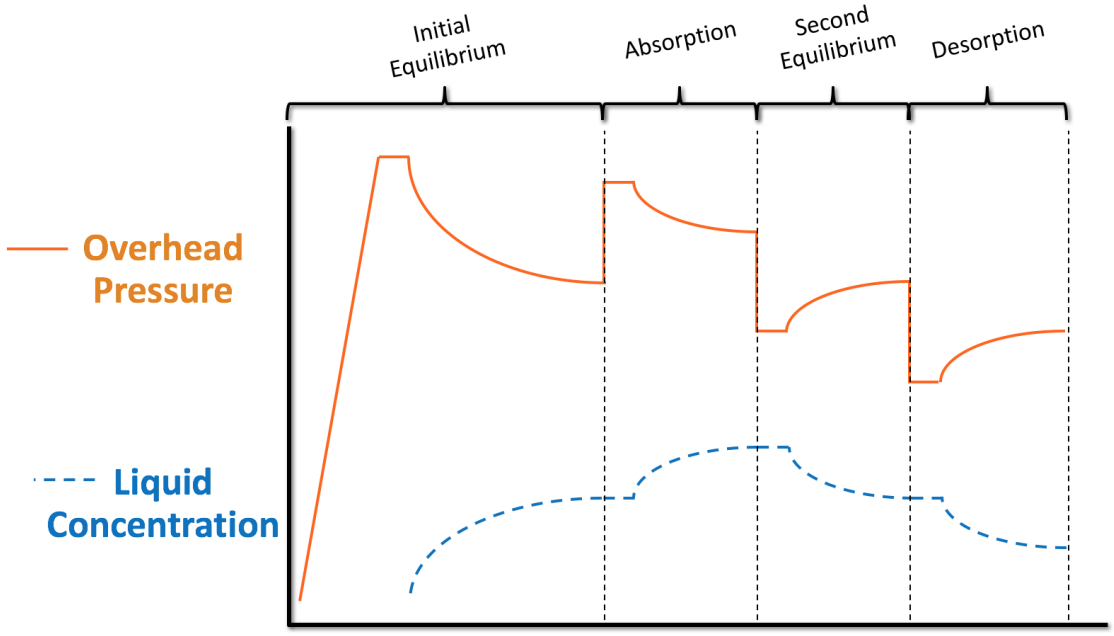

Figure 7.1: Example pressure and resulting concentration change in time for a complete absorption-desorption trial

7.5 Data Analysis

As the absorption and desorption portions of the experiment occur, the gas phase pressure and temperature are continually measured and converted into molar quantities using the same procedure described in Section 6.2. The measured molar change can be normalized using

$$n_{\text{norm}} = \frac{n - n_{\text{initial}}}{n_{\text{final}} - n_{\text{initial}}} \tag{7.4}$$

An example of the change in gas phase moles during absorption and desorption at the same trial conditions can be seen in Figure 7.2.

At equilibrium, the liquid phase mole fraction can be calculated using the simple form of Henrys law using Equation 3.4. Once the solute mole fraction is known, the liquid concentration can be calculated. Srivastan et al. measured equilibrium methane mole fractions at pressure in various hydrocarbon solvents, including n-dodecane (Srivastan et al., 1992). As seen in Figure 7.3, the change in methane

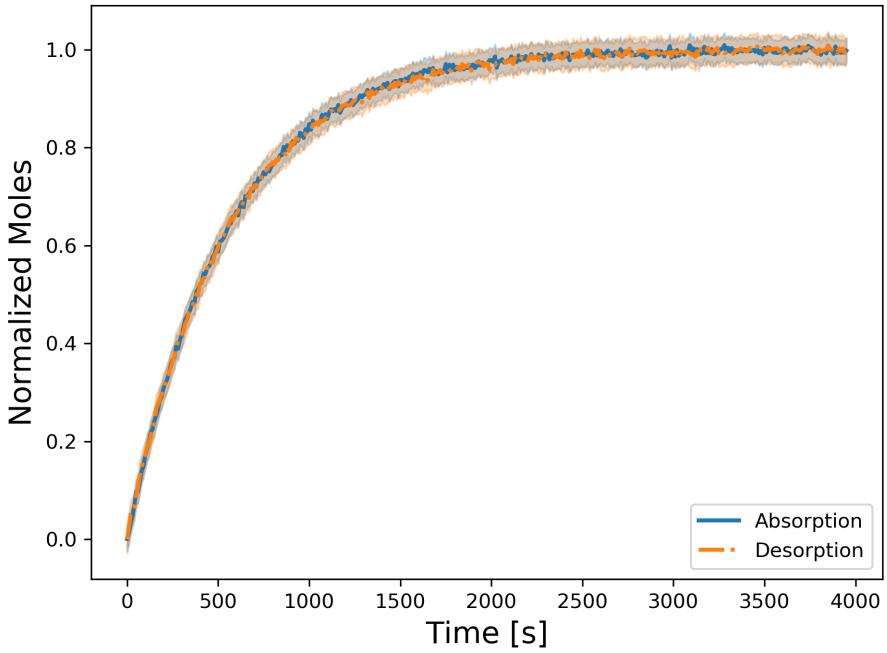

Figure 7.2: Normalized molar change in absorption and desorption experiments at 500 psi (3.45 MPa) and 180 rpm

concentration with pressure does not exhibit large non-idealities, indicating that the simple form of Henrys law is appropriate for the pressure range of interest. While the data from Srivastan et al. was measured at 50 °C, the Henrys constant does not exhibit a strong temperature dependence between 50 °C and 100 °C. Thus, the Henry's constant of $H = 25.7$ MPa at 50 °C was used for dodecane in the current experiment at 45 °C.

The rate of mass transfer across a gas-liquid interface in the case of desorption can be written using Equation 4.8. Since the driving force is reversed for absorption compared to desorption, the concentration difference must be reversed as well to avoid negative rates.

The change in bulk solute concentration was calculated via mole balance with the overhead gas phase. With the concentrations quantified, the volumetric mass transfer coefficient, $k_l a$, is found by plotting the left-hand side of Equation 4.10 against time and calculating the slope of the resulting linear fit. An example of this process

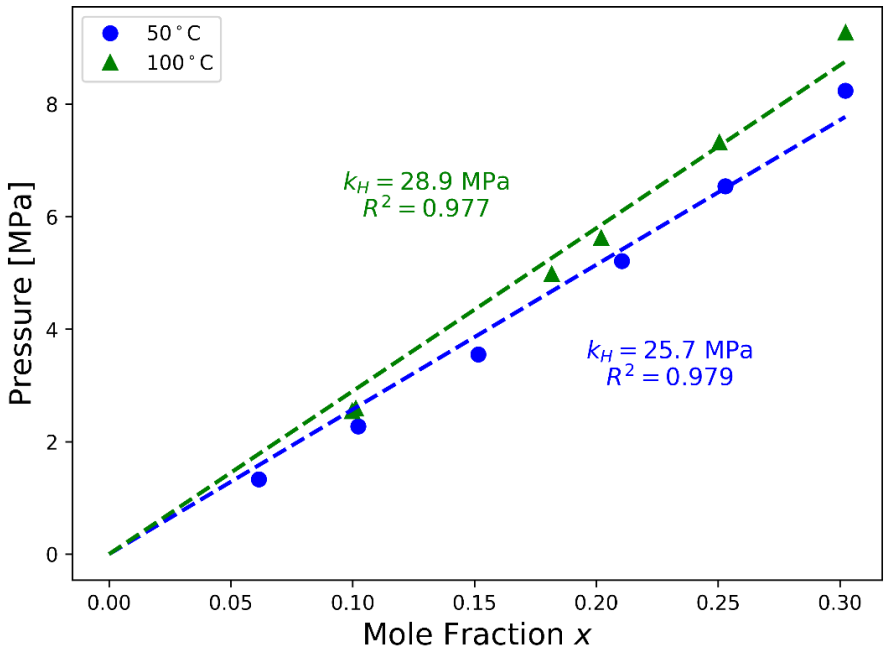

Figure 7.3: Solubility of methane in dodecane at various pressures, data taken from Srivastan et al. (Srivastan et al., 1992)

is seen in Figure 7.4. The first 1,000 s of each trial are used for the initial slope calculation. As the concentration approaches the equilibrium value, the natural log term in Equation 4.10 becomes very sensitive to small variations in the data, leading to potentially erroneous results in the calculated mass transfer coefficient. In order to decouple the mass transfer coefficient, k_l, from the volumetric gas-liquid interfacial area, a, the interfacial area available for mass transfer must be known. Only mixing speeds that did not visually deform the surface of the fluid were used in these experiments. A viewing port on the side of the pressure vessel was used to ensure the interface did not deform during experimental conditions since it has been shown that pressure can affect the quality of the gas-liquid interface under mixing conditions (Versteeg et al., 1987).

As shown previously, the mass transfer coefficient is dependent on both the physical properties of the system as well as the rate of energy dissipation. For non-aerated stirred vessels, the energy dissipation rate is dependent on the mixing speed

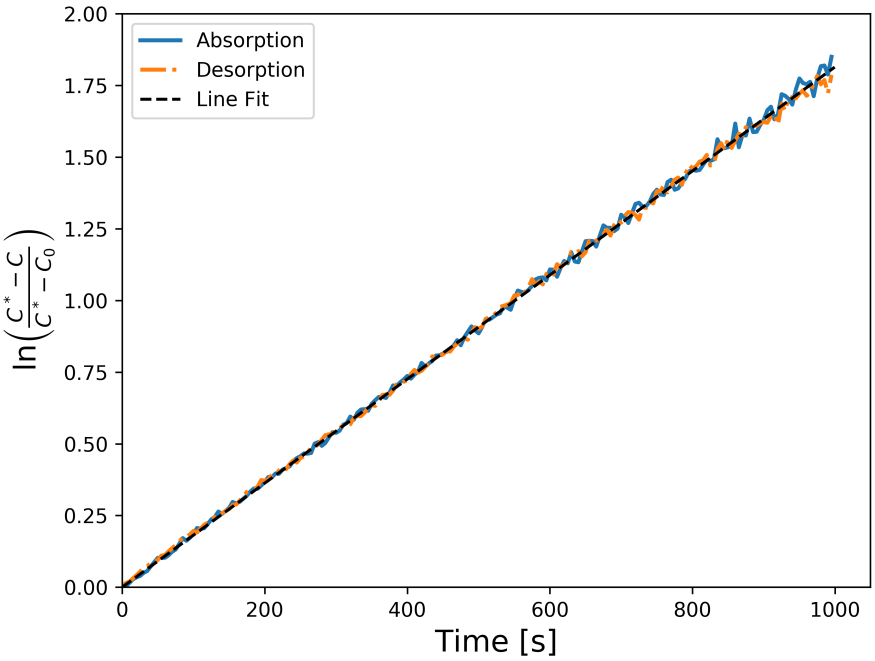

Figure 7.4: Log of normalized bulk concentration vs time for absorption and desorption at 500 psia and 180 rpm

as well as the geometry of the vessel. The dependency of these geometric variables, however, can be condensed into a single parameter, N_p, the power number (Biń, 1984). The average rate of energy dissipation can then be calculated (Garcia-Ochoa and Gomez, 2009)

$$\epsilon = \frac{N_\mathrm{p}\omega^3 d_\mathrm{i}^5}{V_\mathrm{l}} \tag{7.5}$$

The power number was calculated using a correlation for a 6-bladed Rushton turbine in an unbaffled vessel of a similar impeller diameter to vessel diameter ratio (Ma, 2014)

$$N_\mathrm{p} = 12.2 Re_\mathrm{s}^{-0.241} \tag{7.6}$$

where the stirred tank Reynolds number is defined in Equation 7.2. This power number correlation was formulated for Reynolds numbers between 200 and 10,000.

The experimental mixing Reynolds numbers were calculated to be between 2,290 and 6,090. While the experimental input utilized mixing speeds, the energy dissipation rate is the more generalizable mixing term. Since the energy dissipation rate, calculated with Equations 7.5 and 7.6, is dependent on the mixing speed as well as the physical properties of the liquid, the rate of energy dissipation for the same mixing speed will vary at different saturation pressures. As such, the data presented in this chapter will be plotted in terms of the mixing speed, though Table 7.2 is provided to easily convert the mixing speed values to energy dissipation rates at a given pressure.

Table 7.2: Mixing speed to energy dissipation rate conversion at different saturation pressures

P [psia]	ω [rpm]	ω [rps]	ϵ [m^2/s^3]
500	100	1.67	1.85E-04
500	180	3.00	9.38E-04
500	250	4.17	2.32E-03
1,000	100	1.67	1.85E-04
1,000	180	3.00	9.37E-04
1,000	250	4.17	2.32E-03
1,500	100	1.67	1.82E-04
1,500	180	3.00	9.23E-04
1,500	250	4.17	2.28E-03

7.6 Liquid Controlled Mass Transfer

For most gas-liquid mass transfer applications, the rate of mass transfer is assumed to be controlled by the liquid phase, as was done in the derivation of Equation 4.7. This assumption can be tested by calculating the fractional gas side resistance. The definition of the overall mass transfer coefficient with respect to the gas side, similar to Equation 4.6, can be written as

$$\frac{1}{K_g} = \frac{1}{k_g} + \frac{H}{k_l} \tag{7.7}$$

Rearranging, the fractional gas side resistance can be written as

$$\frac{K_g}{k_g} = \left(1 + \frac{H}{k_l/k_g}\right)^{-1} \tag{7.8}$$

Converting from mole fractions to concentration, the Henrys constant is calculated as $H = 58.1$ bar $\cdot$ L/mol. The gas and liquid phase diffusion coefficients can be taken as $D_g = 2.7 \cdot 10^{-5}$ m^2/s (Winn, 1950) and $D_l = 7.9 \cdot 10^{-9}$ m^2/s (Jamialahmadi et al., 2006). The ratio of the mass transfer coefficients can then be calculated assuming the surface renewal model is applicable Sobieszuk et al. (2014)

$$\frac{k_l}{k_g} = \sqrt{\frac{D_l}{D_g}} = 0.017 \tag{7.9}$$

Using the ideal gas law, the mass transfer coefficient ratio can be converted to a normalized concentration value $k_l/k_g = 0.45$ bar $\cdot$ L/mol. From Equation 7.8, the fractional gas side resistance can be calculated as $K_g/k_g = 0.0077$. Within this system, the gas phase mass transfer coefficient is expected to contribute towards only 0.77 % of the total resistance to mass transfer. As such, the assumption of liquid phase controlled mass transfer is justified.

7.7 Error Propagation

Experimental error was evaluated using Monte Carlo error propagation technique from the variability in the pressure transducer, temperature probe, and volume measurement of the overhead gas phase of $\sigma_P \pm 2.0$ psia (14 kPa), $\sigma_T \pm 0.5$ °C, and $\sigma_V \pm 1.2$ mL, respectively. The variability between the pressure, temperature, and volume measurements were assumed to be uncorrelated. First, a Gaussian distribution is generated using (Gardenier et al., 2011)

$$f_{gauss}(X_1, X_2) = \sqrt{-2\ln X_1}\cos 2\pi X_2 \tag{7.10}$$

where X_1 and X_2 are independently generated random numbers ranging from 0 to 1. The Gaussian distribution is then used to convert the measurement variability to a measurement with a normal noise distribution

$$P_\sigma = f_{\text{gauss}}(X_1, X_2)\sigma_{\text{P}} + P \tag{7.11}$$

$$T_\sigma = f_{\text{gauss}}(X_1, X_2)\sigma_{\text{T}} + T \tag{7.12}$$

$$V_\sigma = f_{\text{gauss}}(X_1, X_2)\sigma_{\text{V}} + V \tag{7.13}$$

A Gaussian distribution is approximated for each measured data point using 1,000 points in the distribution. Once the measured values with their associated distributions are generated, they can then be used to propagate the error through other calculations. The distribution in the calculated molar density values is evaluated using

$$\rho_\sigma = EOS(P_\sigma, T_\sigma) \tag{7.14}$$

where the equation used for methane used in this study is taken from Setzmann and Wagner (Setzmann and Wagner, 1991). Once the molar densities are calculated, the error in the molar calculation can be estimated using

$$n_\sigma = \rho_\sigma V_\sigma \tag{7.15}$$

The relative error in the mass transfer coefficient is then calculated from the relative error in the molar calculation (Valiorgue, 2012)

$$\frac{k_{\text{l},\sigma}}{k_{\text{l}}} = \frac{n_\sigma}{n} \tag{7.16}$$

7.8 Results

7.8.1 Desorption Mass Transfer

A summary of the desorption (gas evolution) mass transfer data collected for the absorption-desorption trials at various pressures can be seen in Figures 7.5 – 7.7.

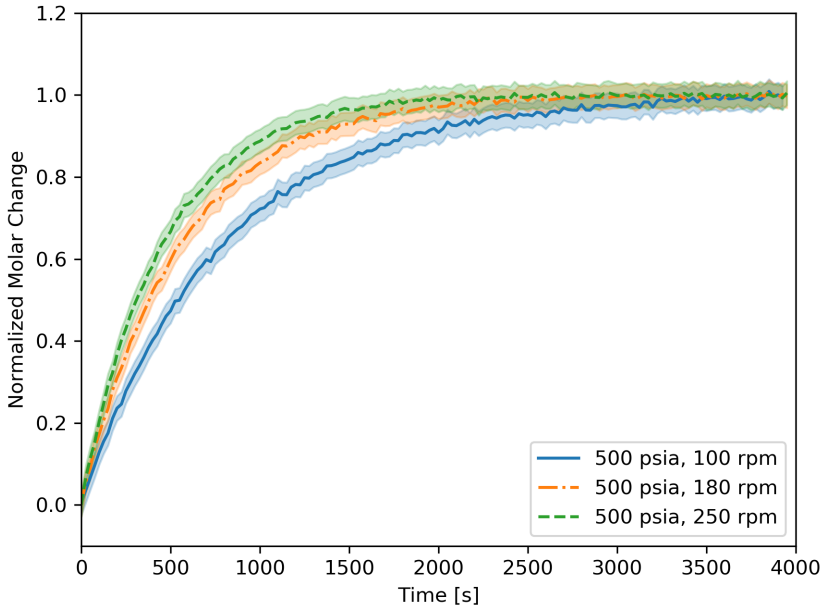

Figure 7.5: Desorption of methane in dodecane at 500 psia (3.45 MPa) and 45 °C

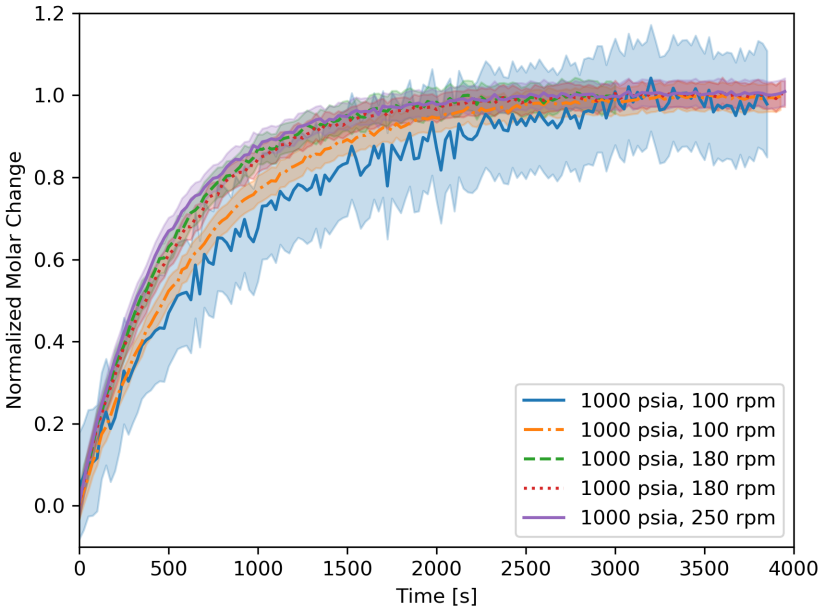

Figure 7.6: Desorption of methane in dodecane at 1,000 psia (6.89 MPa) and 45 °C

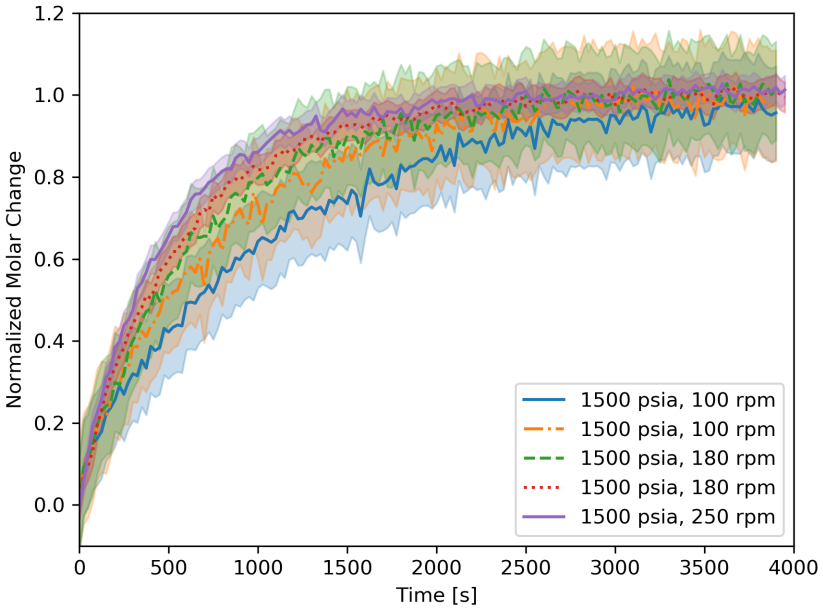

Figure 7.7: Desorption of methane in dodecane at 1,500 psia (10.3 MPa) and 45 °C

Increased mixing speeds resulted in faster rates of mass transfer as expected. As noted earlier, some of the trials were performed with the lower 1.2 mL/min rate of

volume change during the depressurization step. During these trials, the lower driving force resulted in a smaller gas evolution signal compared to what would have been otherwise expected with the 20 mL/min rate of volume change, increasing the relative error compared to the other trials. While the actual mass transfer coefficient was not significantly impacted (see next section), the resulting trials had larger associated error bars. The desorption trial replicates can be seen in Figures 7.8 – 7.11.

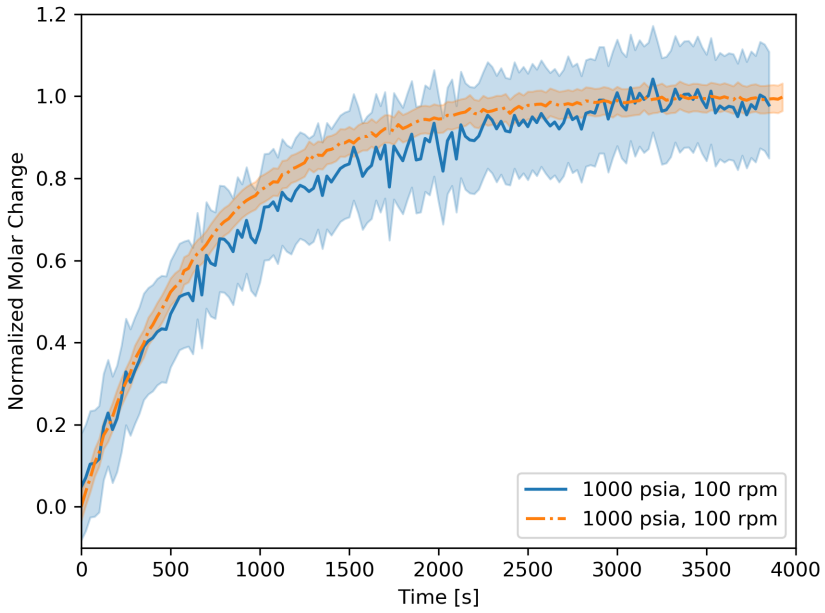

Figure 7.8: Desorption replicate of methane in dodecane at 1,000 psia (6.89 MPa), 100 rpm, and 45 °C

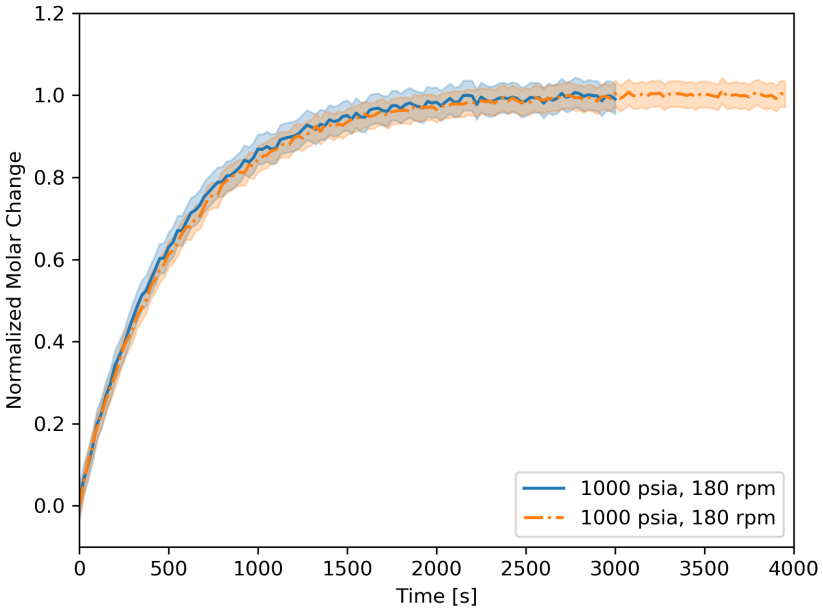

Figure 7.9: Desorption replicate of methane in dodecane at 1,000 psia (6.89 MPa), 180 rpm, and 45 °C

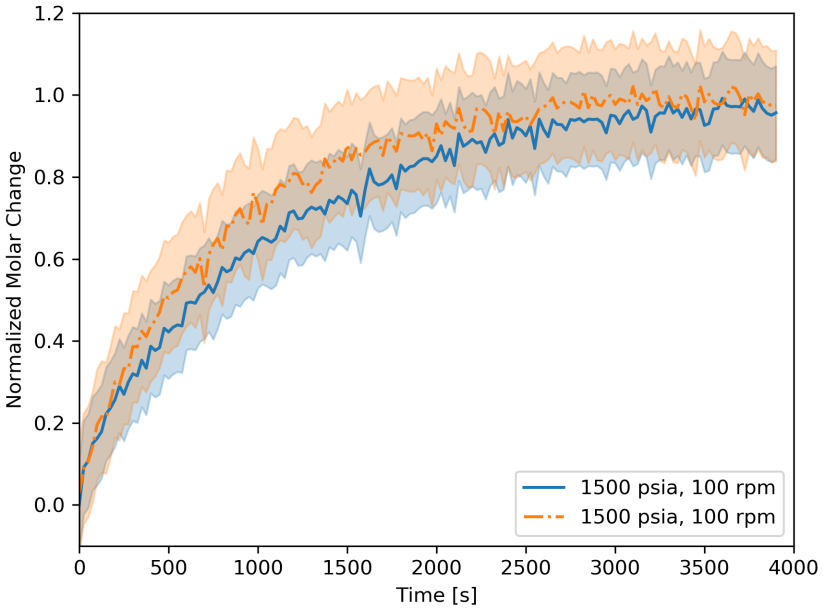

Figure 7.10: Desorption replicate of methane in dodecane at 1,500 psia (10.3 MPa), 100 rpm, and 45 °C

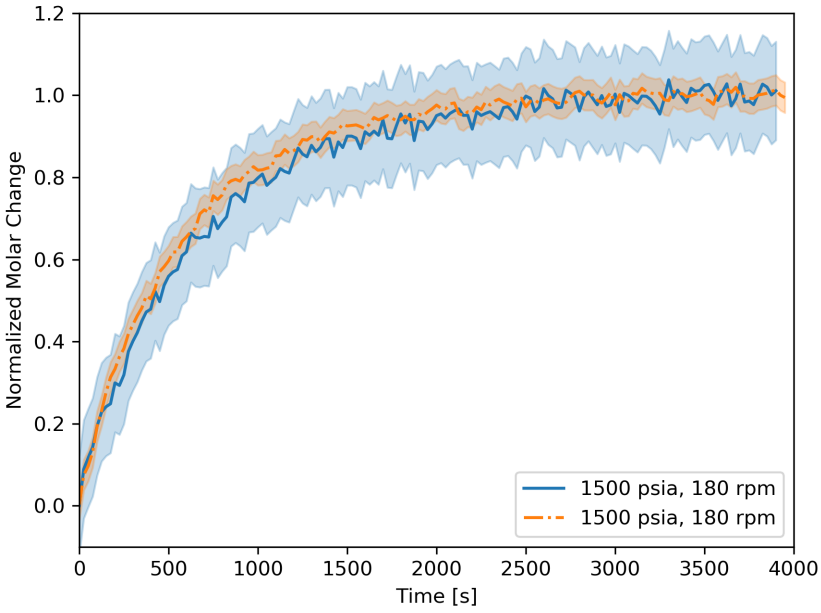

Figure 7.11: Desorption replicate of methane in dodecane at 1,500 psia (10.3 MPa), 180 rpm, and 45 °C

All four desorption trial replicates had overlapping error bars during the entirety of each measurement.

7.8.2 Absorption Mass Transfer

A summary of the absorption mass transfer data collected for the absorption-desorption trials at the tested pressures can be seen in Figures 7.12 – 7.14.

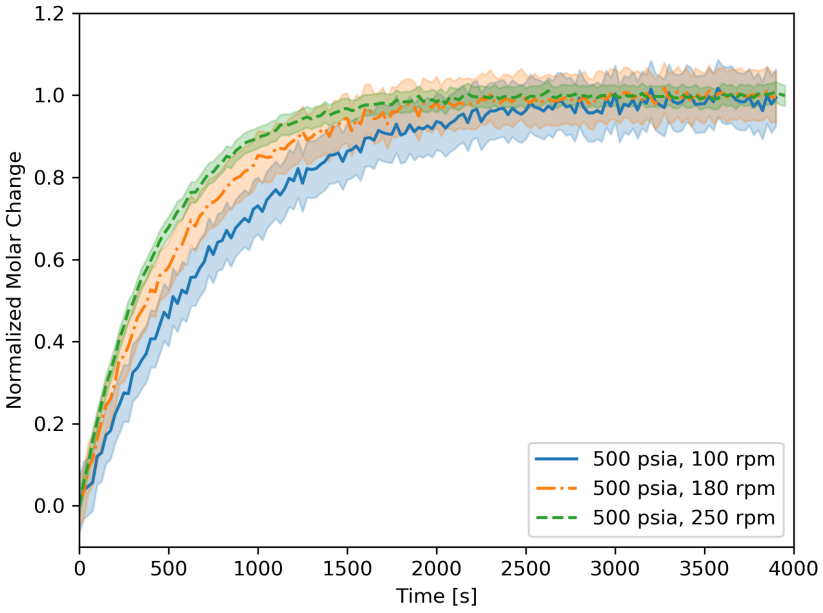

Figure 7.12: Absorption of methane in dodecane at 500 psia (3.45 MPa) and 45 °C

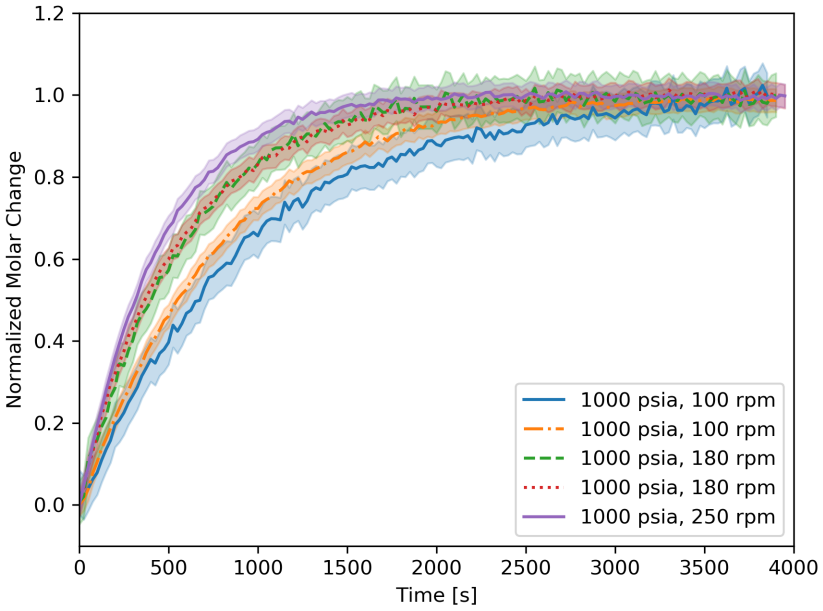

Figure 7.13: Absorption of methane in dodecane at 1,000 psia (6.89 MPa) and 45 °C

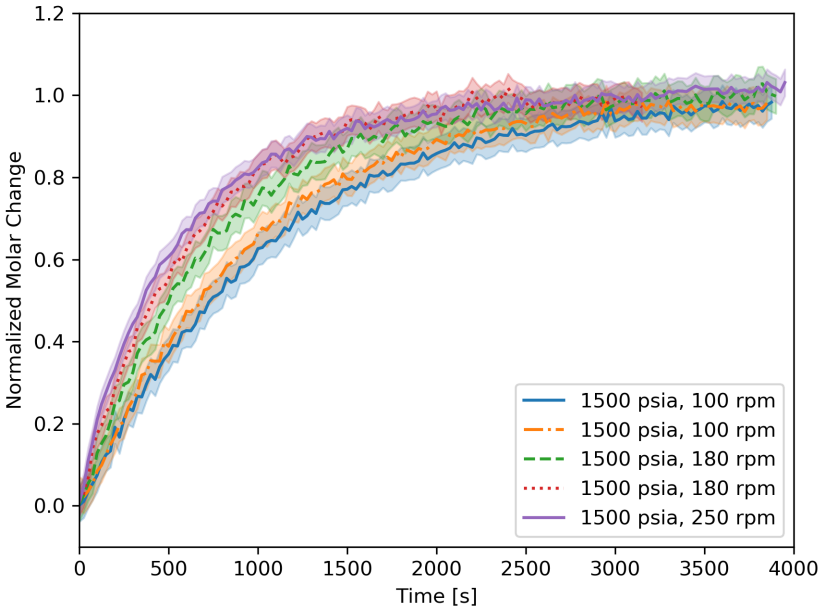

Figure 7.14: Absorption of methane in dodecane at 1,500 psia (10.3 MPa) and 45 °C

In order to avoid negative values in the molar changes, the net positive change in the overhead gas phase moles is shown for the absorption data in Figures 7.12 – 7.14. The same trends for the desorption mass transfer data are seen for absorption: increased mixing speeds result in faster rates of mass transfer. The absorption trial replicates can be seen in Figures 7.15 – 7.18.

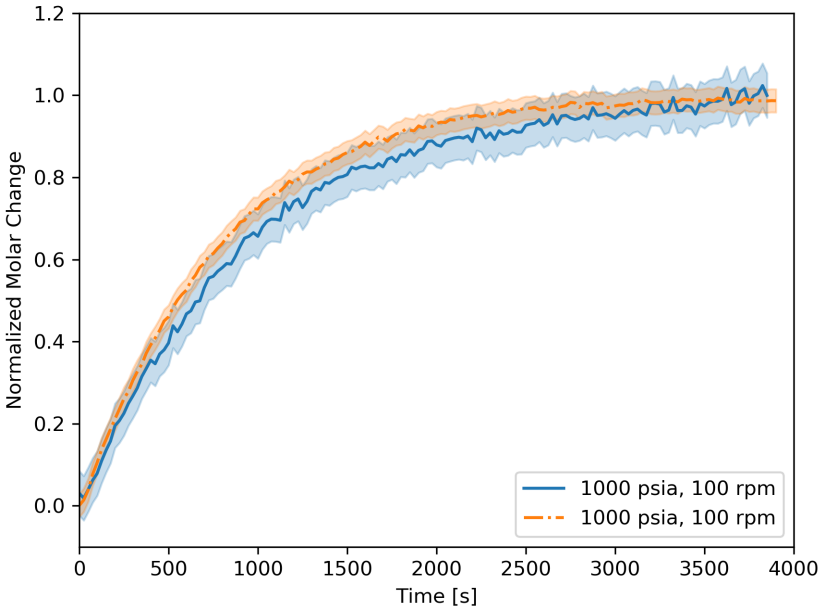

Figure 7.15: Absorption replicate of methane in dodecane at 1,000 psia (6.89 MPa), 100 rpm, and 45 °C

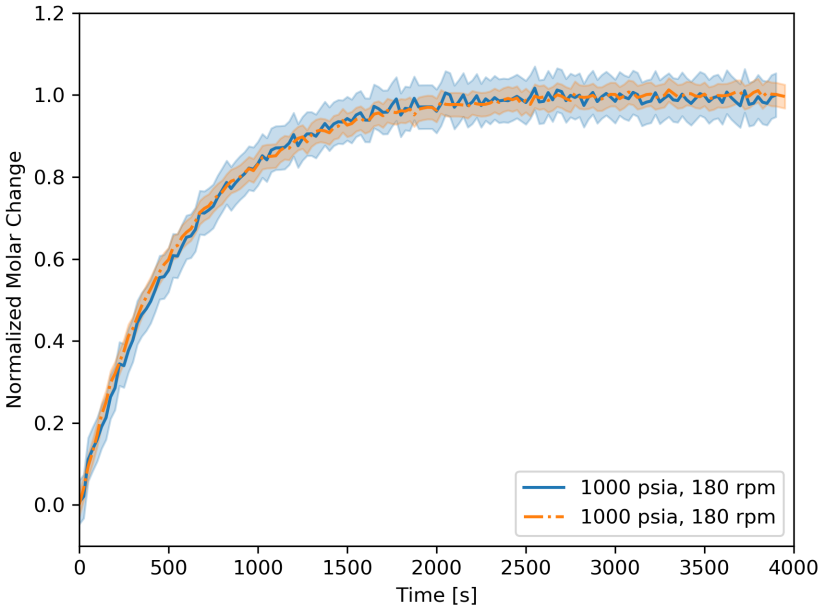

Figure 7.16: Absorption replicate of methane in dodecane at 1,000 psia (6.89 MPa), 180 rpm, and 45 °C

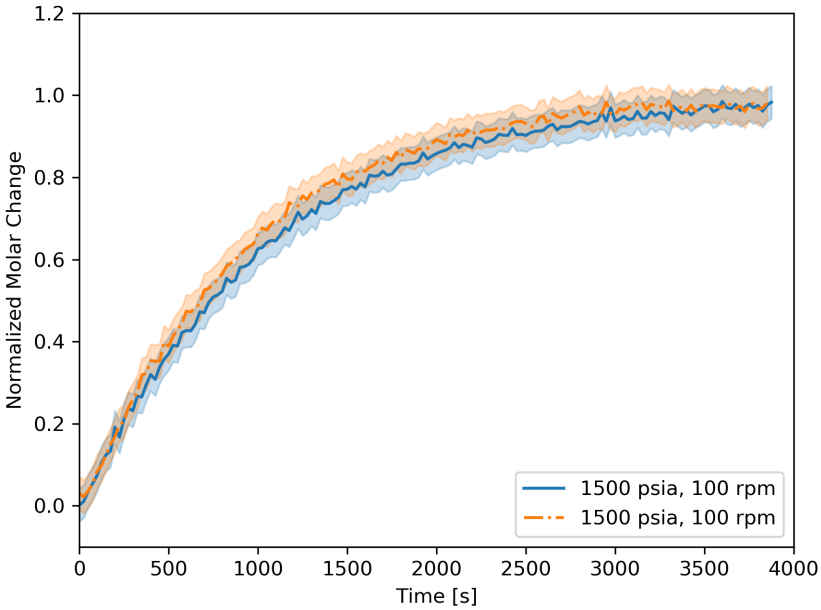

Figure 7.17: Absorption replicate of methane in dodecane at 1,500 psia (10.3 MPa), 100 rpm, and 45 °C

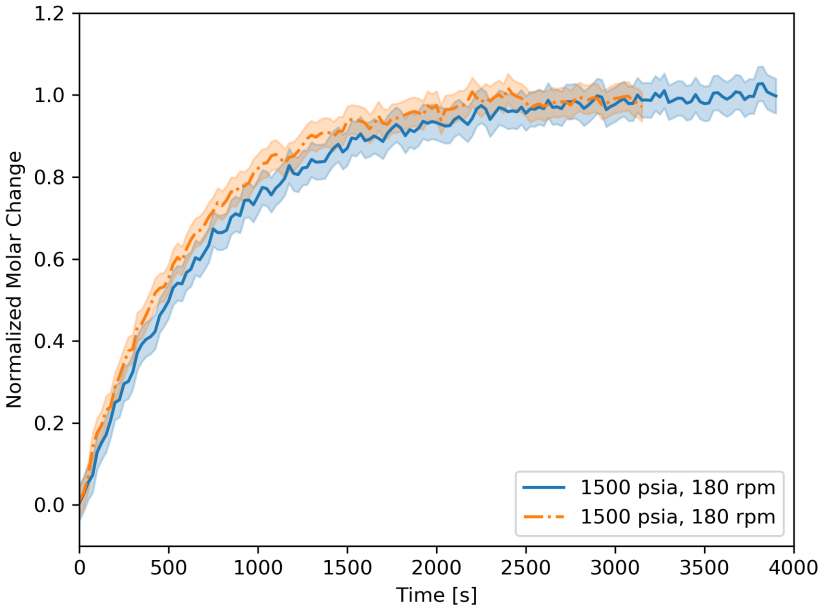

Figure 7.18: Absorption replicate of methane in dodecane at 1,500 psia (10.3 MPa), 180 rpm, and 45 °C

7.8.3 Mass Transfer Coefficients

A comparison of the measured absorption and desorption liquid phase mass transfer coefficients can be seen in Figure 7.19. The uncertainty bars shown on the mass transfer coefficients were calculated using the Monte Carlo error propagation method outlined in Section 7.7. All of the measured absorption and desorption mass transfer rates were within 17% of one another for the same trial and mixing conditions. Only two trials were more than one standard deviation away from parity between the measured absorption and desorption mass transfer coefficient. There was a slight bias towards desorption compared to absorption, though this result was not statistically significant. The measured mass transfer data can be found in Table 7.3.

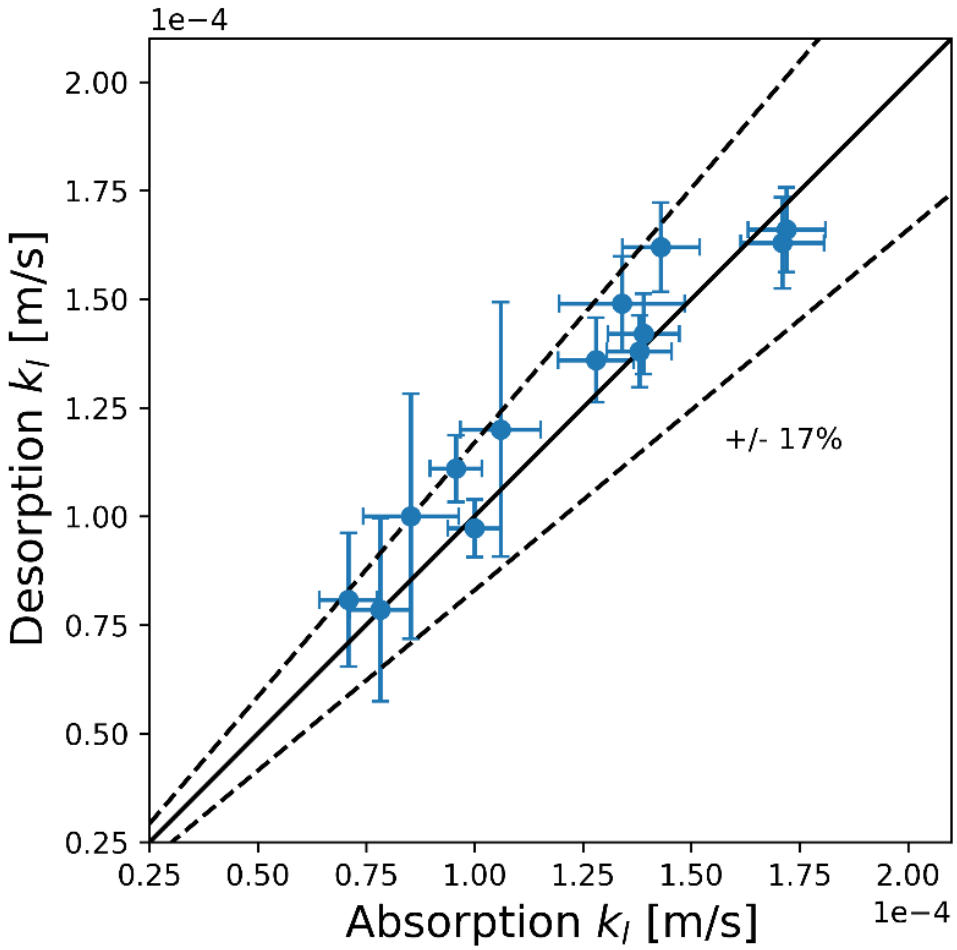

Figure 7.19: Comparison of the measured absorption and desorption mass transfer coefficients

By taking the average of the measured absorption and desorption mass transfer coefficients, the results can be plotted against the initial saturation pressure for that trial. As seen in Figure 7.20, the measured mass transfer coefficients were not a strong function of pressure. Given that the mass transfer coefficient is often modeled as a function of the gas-liquid physical properties (see Equations 4.15-4.16), this weak dependence on pressure is not particularly surprising since the physical properties of the methane-dodecane system, seen in Table 7.1, were themselves not a strong function of pressure.

Evaluating the effect of the impeller mixing speed on the averaged absorp-

Table 7.3: Measured absorption and desorption mass transfer coefficients of the methane-dodecane system

ω [rpm]	P [psia]	Absorption k_l [m/s]	Desorption k_l [m/s]	Mean k_l [m/s]
100	500	1.00E-04	9.73E-05	9.86E-05
180	500	1.38E-04	1.38E-04	1.38E-04
250	500	1.72E-04	1.66E-04	1.69E-04
100	1000	8.53E-05	1.00E-04	9.27E-05
100	1,000	9.57E-05	1.11E-04	1.03E-04
180	1,000	1.34E-04	1.49E-04	1.42E-04
180	1,000	1.39E-04	1.42E-04	1.40E-04
250	1,000	1.71E-04	1.63E-04	1.67E-04
100	1,500	7.09E-05	8.08E-05	7.59E-05
100	1,500	7.82E-05	7.85E-05	7.83E-05
180	1,500	1.06E-04	1.20E-04	1.13E-04
180	1,500	1.28E-04	1.36E-04	1.32E-04
250	1,500	1.43E-04	1.62E-04	1.52E-04

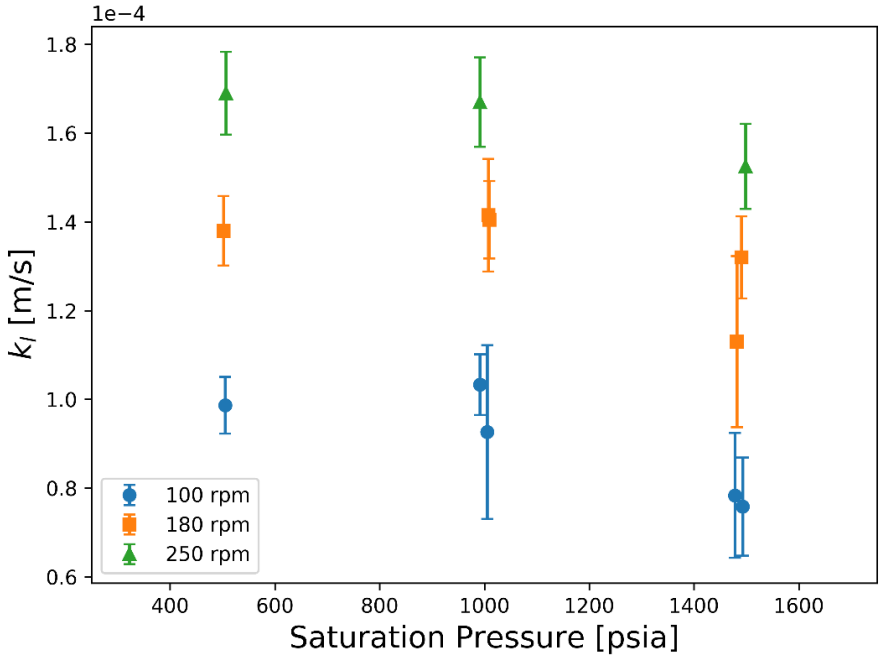

Figure 7.20: Effect of initial saturation pressure on the averaged absorption/desorption mass transfer coefficients

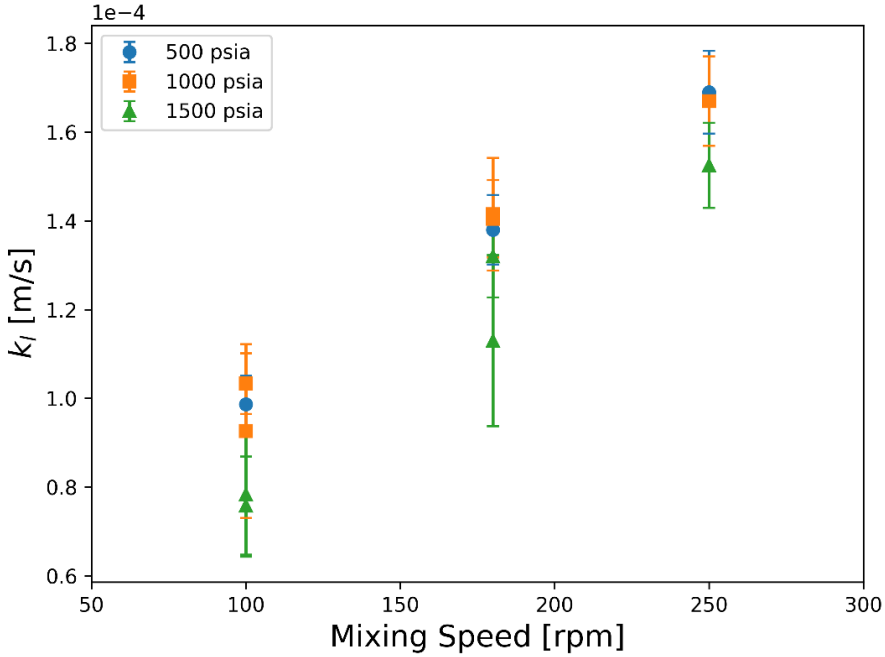

Figure 7.21: Effect of mixing speed on the averaged absorption/desorption mass transfer coefficients

tion/desorption mass transfer coefficients in Figure 7.21, a clear trend is visible. As expected, increasing the impeller mixing speed leads to an increase in the rate of mass transfer for a given pressure. The mixing speed, and by extension the liquid hydrodynamics, is the most significant variable affecting the mass transfer rates for the experiments shown here.

The surface renewal theory in the form of Lamont and Scott's small eddy model was applied to the experimental conditions tested and the applicability of the model was evaluated. Lamont and Scott's solid surface model, Equation 4.15, was first tested. A comparison between the measured mass transfer coefficients and the solid surface model predictions can be found in Table 7.4. The absolute average error between the measured mass transfer coefficients and the solid surface model resulted in a value of 12.3%.

Lamont and Scott's fluid surface model, Equation 4.16, was also tested against the measured values. A comparison between the measured mass transfer coefficients

Table 7.4: Measured mass transfer coefficients compared to the Lamont and Scott solid surface model (Lamont and Scott, 1970)

		Measured	Solid Surface	
ω [rpm]	P [psia]	Mean k_l [m/s]	Predicted k_l [m/s]	Error [%]
100	500	9.86E-05	8.03E-05	-18.5
180	500	1.38E-04	1.20E-04	-12.5
250	500	1.69E-04	1.51E-04	-10.4
100	1000	9.27E-05	8.16E-05	-12.0
100	1000	1.03E-04	8.16E-05	-21.0
180	1000	1.42E-04	1.22E-04	-13.6
180	1000	1.40E-04	1.22E-04	-12.9
250	1000	1.67E-04	1.53E-04	-8.0
100	1500	7.59E-05	8.76E-05	15.5
100	1500	7.83E-05	8.76E-05	11.9
180	1500	1.13E-04	1.31E-04	15.9
180	1500	1.32E-04	1.31E-04	-0.1
250	1500	1.52E-04	1.65E-04	8.2

and the fluid surface model predictions can be found in Table 7.5. The absolute average error between the measured mass transfer coefficients and the fluid surface model resulted in a value of 86.3%.

As previously stated in Section 4.2.5, the difference between the solid and fluid surface models originates from the difference in how the boundary conditions of the liquid interface were defined. All mass transfer coefficients were measured during conditions where a flat gas-liquid interface was maintained. Direct measurement within the experiment as to whether the surface was truly stagnant or if there was some degree of liquid flow tangential to the interface was not possible. If there was some degree of vortexing occurring during mixing, the tangential velocity at the interface would be non-zero. However, since there was no visual deformation of the liquid interface, it is assumed that any force occurring tangential to the interface was not strong enough to overcome the surface tension forces holding the interface in a static state. Thus, it is assumed that the tangential liquid velocity as well as the normal liquid velocity at the interface were both negligible. Several studies

Table 7.5: Measured mass transfer coefficients compared to the Lamont and Scott fluid surface model (Lamont and Scott, 1970)

		Measured	Fluid Surface	
ω [rpm]	P [psia]	Mean k_l [m/s]	Predicted k_l [m/s]	Error [%]
100	500	9.86E-05	1.59E-04	60.9
180	500	1.38E-04	2.38E-04	72.8
250	500	1.69E-04	2.98E-04	76.9
100	1000	9.27E-05	1.60E-04	73.1
100	1000	1.03E-04	1.60E-04	55.5
180	1000	1.42E-04	2.41E-04	69.9
180	1000	1.40E-04	2.41E-04	71.4
250	1000	1.67E-04	3.02E-04	81.0
100	1500	7.59E-05	1.69E-04	122.1
100	1500	7.83E-05	1.69E-04	115.1
180	1500	1.13E-04	2.53E-04	122.8
180	1500	1.32E-04	2.53E-04	92.0
250	1500	1.52E-04	3.17E-04	108.1

investigating the axial flow distribution within stirred tanks using Rushton turbines also indicate that the liquid mixing approaches stagnant conditions at the interface (Wang et al., 2014; Ammar et al., 2011; Wu et al., 1989; Ducci and Yianneskis, 2005). The difference in average error between the solid surface model and the fluid surface model is in agreement with this assumption. The solid surface model, which assumes stagnant conditions at the interface, exhibits a better fit to the experimental data compared to the fluid surface model.

An important feature of the eddy cell model arises from the fact that the energy dissipation from both the viscous and inertial forces are considered within the model derivation. The viscous forces represent the smallest scales of motion at the interface while the inertial forces represent the larger scales of motion within the fluid. Though the viscous forces are assumed to be controlling with respect to the rate of mass transfer, the larger scales of motion within the fluid contain more energy, thus their effect on mass transfer should not be neglected (Fortescue and Pearson, 1967). The model presented by Lamont and Scott is arrived at by integrating the contribution

of a range of different eddy sizes, including the viscous and inertial scales (Lamont and Scott, 1970). If the rate of energy dissipation from only the viscous sublayer is considered, the model will generally overestimate the mass transfer coefficient. For example, the mass transfer model for Newtonian fluids derived by Kawase et al. over predicts the mass transfer coefficients from this experiment by an average of 425% (Kawase and Moo-Young, 1987).

7.9 Conclusion

The liquid phase mass transfer coefficients during absorption and desorption were measured using identical experimental conditions. All measured absorption and desorption mass transfer coefficients were within 17% of one another for the same trial conditions. These results serve as further evidence for the assumption of symmetry between the absorption and desorption rates of mass transfer, even at high pressures. Furthermore, the symmetry in mass transfer coefficients confirms that bubble nucleation is not significantly affecting the desorption (gas evolution) measurement.

The mixing speed was found to be the most significant variable affecting the rate of mass transfer while changing the saturation pressure had minimal effect. Due to the non-linear behavior of the liquid physical properties at variable solute concentrations, it would not be unreasonable to expect that pressures higher than those tested here could have a larger impact on the rate of mass transfer. The surface renewal theory in the form of the small eddy model was found to be a good fit to the data. The solid and fluid surface eddy cell models were applied to the experimental conditions and resulted in a reasonable fit for both cases. The solid surface model with an averaged absolute error of 12.3%, serves as further evidence that the gas-liquid interface more closely resembled stagnant conditions when compared to the fluid surface model.

CHAPTER VIII

HORIZONTAL SEPARATOR MODELING

As discussed in Section 2.4.2, the current degassing guidelines are inadequate for gas-liquid separation in high pressure environments or viscous oils, where there is increased potential for gas evolution to contribute significantly to gas carry-under. With the mass transfer behavior quantified for a reference hydrocarbon system at pressure, a separator degassing model can be constructed that accounts for gas carry-under due to both entrained gas and excess solution gas.

8.1 Model Development

Previous methods of estimating the bubble separation capacity of a separator do not quantify the amount of gas carry-under a given process condition will produce. Instead, these bubble capacity calculations yield a simple binary decision as to whether the liquid residence time within the separator is sufficient or not. In terms of actually quantifying gas carry-under, Slettebø made significant progress on modeling the degassing process within a separator (Slettebø, 2009). The degassing model for a horizontal separator was constructed by subdividing the initial liquid height into various horizontal sections then calculating the bubble velocity required per section in order for a bubble to reach the bulk gas-liquid interface before a given liquid residence time is reached. A bubble distribution is then assigned to each horizontal subsection and individual bubble velocities for the entire distribution are calculated. For each section, any bubbles with a velocity larger than the bubble velocity required for separation in that section are assumed to be separated. Bubbles with velocities smaller

than the required bubble velocity for separation are assumed to remain in solution and therefore carried into the exiting liquid stream as gas carry-under. The remaining bubble distribution can then be compared to the initial bubble distribution and the percent of entrained bubbles separated can be calculated. The model does not, however, maintain a liquid mass balance throughout the separator. Also, gas evolution from a supersaturated solution cannot be accounted for within this framework.

In this chapter, the basic algorithm presented by Slettebø will be extended to account for bubbles at different horizontal subsections of a separator as well as their progression through time as they travel through the separator. This will allow the degassing model to account for the changing liquid height as bubbles exit the solution as well as the total interfacial area available for mass transfer over time. Using this estimate for the total interfacial area, the total rate of mass transfer within the separator can be calculated along with the resulting solution gas concentration for a supersaturated solution. The proposed algorithm will enable gas carry-under due to solution gas along with gas carry-under due to entrained bubbles to both be calculated. Sensitivity analyses are then utilized to investigate the effect of different process conditions and physical properties on both forms of gas carry-under. Since laminar conditions are expected within the separator, bubble breakup will not be particularly relevant and will not be considered here. Likewise, bubble coalescence is not considered either. Bubble coalescence would increase the average size of the bubbles within the liquid, leading to larger bubble velocities and faster separation times. By not including coalescence, the calculated percentage of gas removal will err on the side of being conservative. While bubble nucleation, as seen in Section 3.1, does have the potential to occur in slightly supersaturated solutions, the bubble nucleation rate depends on a variety of different phenomena including the radius of curvature of the pre-existing nuclei, surface roughness of the solid surface, and the stability of active nucleating sites over time. As such, the inclusion of bubble

nucleation is considered outside the scope of the degassing model presented here.

8.1.1 Model Assumptions

The general model assumptions are listed as follows:

1. The degassing model only accounts for how bubbles move through the liquid phase. The bubbles are assumed to move in only two directions: forward (with the liquid flow) and upward (towards the bulk gas-liquid interface).

2. The model assumes the liquid and entrained gas have a plug flow velocity profile.

3. The bubbles are assumed to be solid spheres within the liquid.

4. The bubble volume within the liquid directly displaces an equal volume of liquid.

5. Both the temperature and pressure are assumed to be constant, along with the physical properties of the phases.

6. No bubble coalescence, bubble break up, or bubble nucleation is accounted for in this framework.

7. Once a bubble is calculated as having risen above the height of the bulk gas-liquid interface, the bubble is assumed to be separated.

8. Any bubbles remaining in the liquid once the liquid residence time has elapsed are assumed to be carried under in the exiting liquid stream.

In order to maintain the conservation of the liquid mass within the separator as bubbles are separated from the bulk liquid, the liquid level is allowed to vary within the separator. If the liquid level is held constant at its initial height, the liquid volume would artificially grow to maintain the initial liquid level as bubbles are separated from the bulk liquid. A steady state model that allows the liquid level to rise and fall throughout length of the separator is, however, unrealistic from the perspective

of a real system: a real separator would maintain a roughly constant liquid height throughout. In order to dynamically model the liquid height in a flowing system as bubble are exiting the bulk liquid, the model must account for the bubble rise and hydraulic force as well as the liquid displacement force exerted by the bubble as it rises through the liquid. Without the horizontal liquid displacement force, a model of the gas-liquid system will not be able to self-correct towards a constant liquid level.

Instead of explicitly modeling the hydraulic force of the liquid along with the displacement force of the bubbles in a flowing liquid system, a flat gas-liquid interface will be assumed within the current modeling framework. The problem with assuming a flat interface, as previously pointed out, is in maintaining a mass balance within the liquid. For a given inlet flow rate, as the bubble rise out of solution, artificial liquid volume must be generated in order to maintain that constant liquid level. However, if the total effective liquid volume of the system post-separation is known (the liquid volume along with the volume of gas yet to be separated from the liquid) and the liquid level is assumed to be flat throughout, then this liquid level can be easily calculated. By employing an multi-pass modeling approach, the total effective volume of the system is initially guessed and the liquid level is calculated. Using this initial liquid level, the separator model is then solved yielding a new total effective volume. This process is iterated, using the calculated effective liquid volume as the initial guess, until the liquid mass balance converges to the desired specification.

8.1.2 Separation Algorithm

The horizontal separator presented here is modeled as a cylinder on its side without any internals. The fluid flow through the separator is assumed to be uniform (plug flow) with no wall effects. Discretization is performed both vertically through the liquid height and horizontally through the vessel length. Each point where the vertical and horizontal subdivisions intersect becomes a node, where the vertical

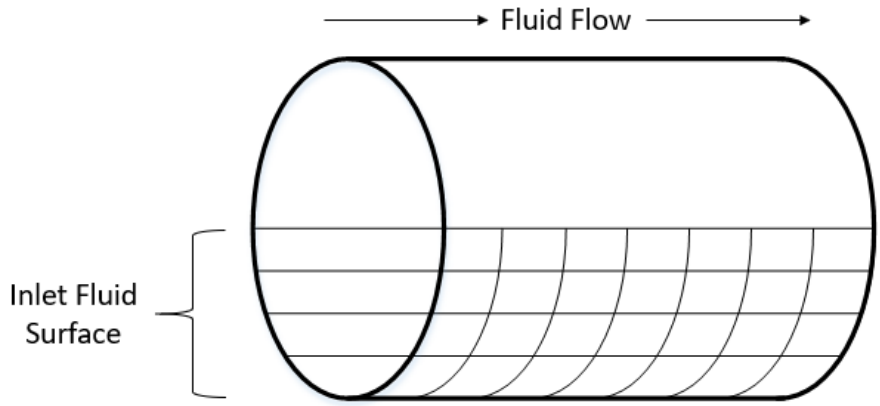

Figure 8.1: Schematic of the horizontal separator model discretization

indexing is represented with i and the horizontal indexing is represented with j. The i index is used as an indicator of the liquid depth, while the j index marks the liquids travel through time. Figure 8.1 depicts the separator discretization through the bulk of the fluid.

Each node within the gas-liquid separator model can then be represented as a set of different variables

$$\text{node}_{ij} = (d_k, N_k, v_k, h_k)_{ij} = d_{ijk}, N_{ijk}, v_{ijk}, h_{ijk} \tag{8.1}$$

where d_k is the bubble size distribution, N_k is the bubble frequency, v_k is the bubble velocity, h_k is the bubble rise distribution, and k is the index variable for each element in the respective distributions. Four nodes form the corners of a cell, with an initially defined cell height, ΔL_l, and time required for the liquid flow to move through the cell horizontally, Δt. An example of this structure can be seen in Figure 8.2.

Assuming the bubble frequency and distribution, d_k and N_k, are given for the initial $j = 0$ time step (see Section 8.1.3 for more details), the bubble velocity can then be calculated for each individual bubble diameter resulting in a corresponding bubble velocity distribution per cell. The percent bubble rise distribution per cell can then be calculated by multiplying each individual bubble velocity by the liquid

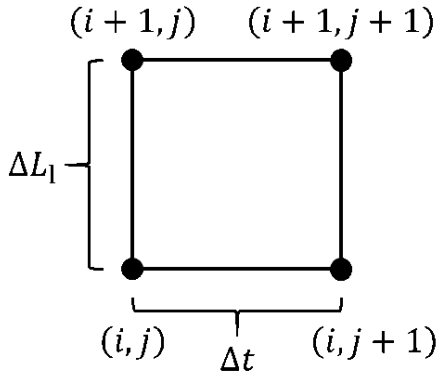

Figure 8.2: Separator cell indexing

residence time per cell, Δt, divided by the height per cell. The percent bubble rise from the previous time step is then added to the current so that the bubble rise accounting is not restarted at each new time step (for the first time step, all bubbles start with a percent bubble rise of 0.0). The resulting percent bubble rise distribution indicates how far the bubbles will rise within the time taken to move from j to $j+1$. The separation algorithm per cell then becomes the following: if the percent bubble rise is larger than 1.0, the bubble is moved from (i,j) to $(i+1,j+1)$, if not the bubble is moved from (i,j) to $(i,j+1)$. If the bubble is moved up in vertical height, 1.0 is subtracted from that bubbles rise distribution. The separation algorithm starts from the bottom of the vessel, $i=1$, and continues upwards until the total number of vertical incrementations, $i=I$, is reached. Any bubbles removed from this final node are then assumed to be completely separated from the liquid phase. The algorithm then calculates the new liquid height from the total amount of bubbles remaining in solution and moves forward in time from j to $j+1$, starting over from the bottom of the vessel. For each new time step, the cell height is calculated based on the new height of the liquid. The resulting discretization mesh adapts to the changing liquid height over time. An example of this adaptive mesh implementation can be seen in Figure 8.3.

The entire separation algorithm per time step is then repeated until the final horizontal incrementation is reached, $j=J$. Any bubbles remaining in the liquid are

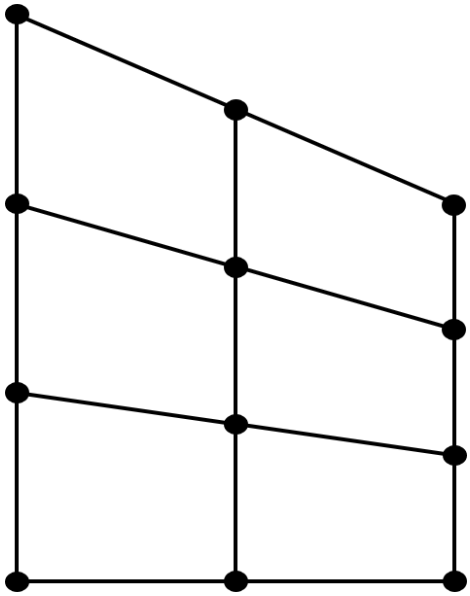

Figure 8.3: Separator adaptive mesh

then assumed to be carried under as entrained gas carry-under. The complete bubble separation algorithm is depicted in Figure 8.4.

If the entering liquid solution is supersaturated with dissolved gas, there will also be mass transfer between the liquid and gas phase associated with the time domain. Mass transfer between the liquid and the gas will result in bubble growth between j to $j+1$. Larger bubble diameters will result in larger bubble velocities and larger bubble rise distributions per cell compared to non-mass transfer conditions. For mass transfer conditions, a bubble growth term will be added prior to the bubble velocity calculation (this growth term equals zero if the solution is only saturated). Once the algorithm proceeds through all the time steps, the total gas-liquid interfacial area is calculated by summing the interfacial area provided by bubbles remaining in solution with the total bulk interfacial area. The total change in solute concentration can then be calculated. If the solution is still supersaturated once the residence time has elapsed, the remaining solution gas is assumed to carry into the exit liquid stream.

In order to set up the multi-pass approach required to correct for the changing liquid height throughout the separator length, the entire separator model is solved

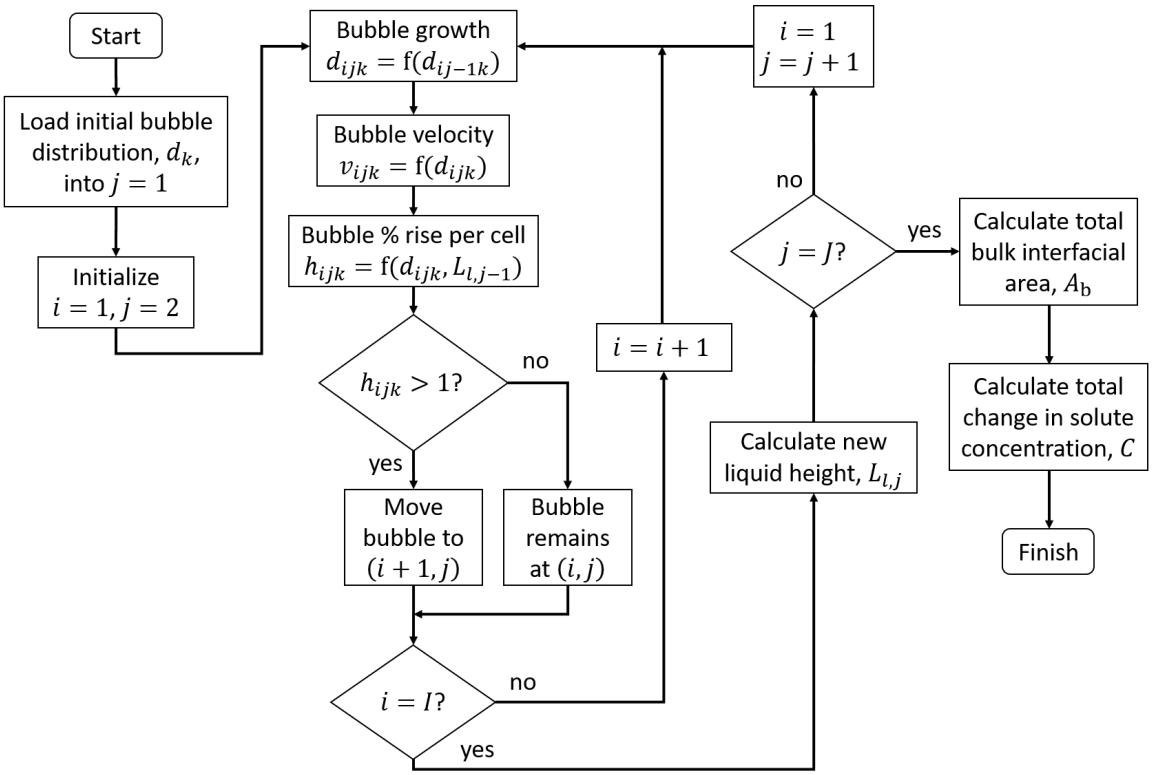

Figure 8.4: Bubble separation algorithm

iteratively. By first guessing the total effective liquid volume, the model can then calculate the constant liquid level and solve through the separator residence time using a fixed liquid level. Once finished, the total bubble volume within the separator can be calculated by summing the entrained bubble volume through the various time steps. Then using the total bubble volume along with the initial effective liquid volume guess, the liquid volume within the separator can be calculated. This calculated liquid volume can then be compared to the known liquid volume calculated from the volumetric flow rate and the liquid residence time in the model input conditions (seen in Table 8.1). The error between the calculated and actual liquid volume can then be evaluated. Using this error, a new effective volume guess can be calculated and the process is repeated until the absolute mass balance error in the liquid volume is under 0.01 % (the liquid mass can be directly calculated from the liquid volume since the liquid density is assumed to be constant). While the effective density will vary

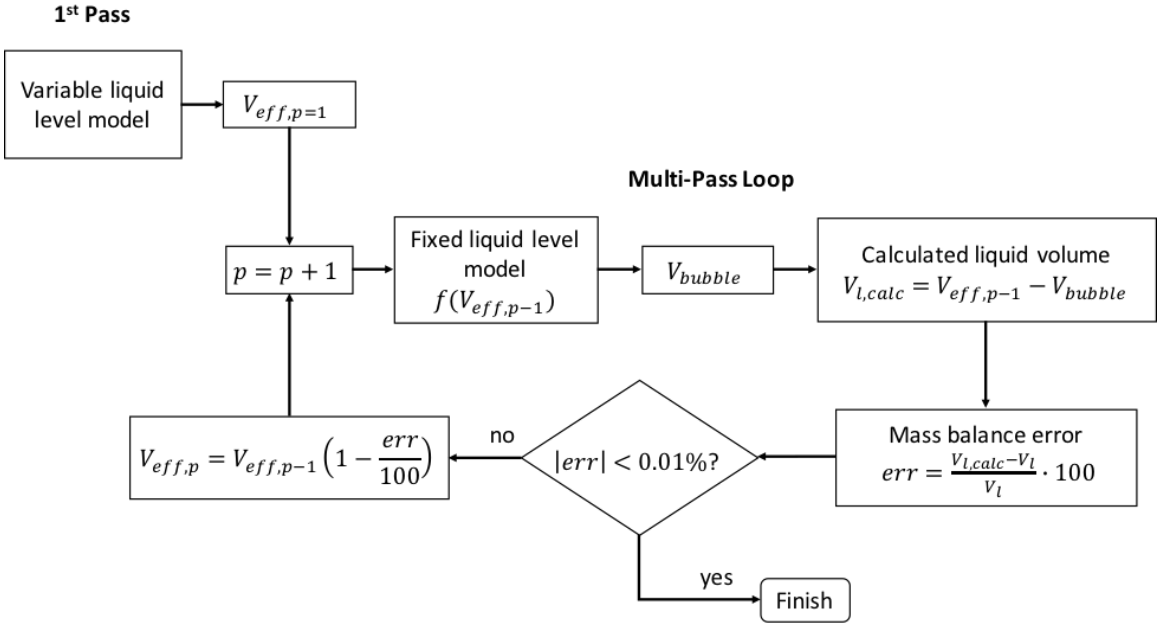

Figure 8.5: Multi-pass separator algorithm

axially within the separator, the liquid level itself will be held constant.

In order to jump start the process, the variable liquid interface model is run and the calculated total effective volume is then taken as the initial guess. The algorithm needs to be iterative because changing the effective volume will change the liquid height. A change in the liquid height will then change the total bubble volume separation and subsequent total liquid volume calculation. A graphical representation of the multi-pass algorithm can be seen in Figure 8.5.

The new effective liquid volume is calculated at each pass by taking the negative of the error in the liquid volume mass balance. If the calculate liquid volume is larger than the required liquid volume, the resulting error would be positive. In order to correct for this at each loop, the effective liquid volume must be lowered. Thus, each loop will correct the effective volume guess from the negative of the error in the liquid mass balance.

The error tolerance of 0.01 % was selected to ensure that the mass balance close enough to approximate real conditions while avoiding excessively long compute. For the majority of the input conditions, the model results would reach the desired

error tolerance within 3 iterations (the largest observed amount of iterations required to converge the model was 8).

8.1.3 Geometric Specifications

First, the volumetric flow rate of entrained gas is calculated using a given entrained gas fraction, x_{eg}, and total liquid volumetric flow rate, Q_{l}

$$Q_{\mathrm{g}} = Q_{\mathrm{l}} \frac{x_{\mathrm{eg}}}{1 - x_{\mathrm{eg}}} \tag{8.2}$$

From a given liquid residence time, t_{r}, and vessel length, L_{ves}, the total vertical cross-sectional area of the liquid flow can be found using

$$A_{\mathrm{l}} = \frac{(Q_{\mathrm{l}} + Q_{\mathrm{g}}) t_{\mathrm{r}}}{L_{\mathrm{ves}}} \tag{8.3}$$

The liquid surface area can also be expressed in terms of the angle formed between the bulk gas-liquid interface and the center of the vessel, θ

$$A_{\mathrm{l}} = \theta r^2 - \frac{r^2 \sin(2\theta)}{2} \tag{8.4}$$

where r is the vessel radius. Using Equation 8.3 in conjunction with Equation 8.4, the are angle θ can be determined. The length of the liquid interface is then found using

$$L_{\mathrm{int}} = 2r \cos\left(\frac{\theta}{2}\right) \tag{8.5}$$

The liquid height within the vessel can also be found using

$$L_{\mathrm{l}} = r\left(1 - \cos(\theta)\right) \tag{8.6}$$

The liquid height along with the length of the liquid interface is represented in Figure

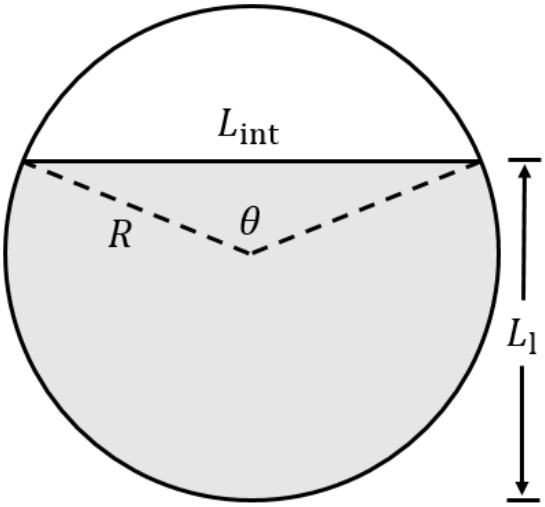

Figure 8.6: Length of bulk gas-liquid interface within the separator

8.6.

As bubbles exit the liquid over time, the total amount of entrained gas decreases. At each time step, after the total bubble separation is determined, the liquid height and liquid interface length are re-calculated using Equation 8.3 – 8.6. The bulk gas-liquid interfacial area is then determined by summing the product of each liquid interface length with the corresponding vessel length increment with each time step.

In order to complete the inlet specification of the separator model, a bubble distribution must be specified. For the model results presented here, a Rayleigh distribution was selected. The Rayleigh distribution has been successfully used to approximate bubble distributions in bubble columns (Lau et al., 2013), fluidized bed reactors (Liu and Clark, 1995; Lim and Agarwal, 1990; Rüdisüli et al., 2012; Clark et al., 1996), and multiphase flows (Liu et al., 1996; Zheng et al., 1983; Holland et al., 2011). Assuming the inlet bubble distribution within the liquid obeys a Rayleigh-type distribution, the probability density function can be computed using

$$P_{\text{d},k}(d_k|d_{\text{m}}) = \frac{d_k}{d_{\text{m}}^2} \exp^{\left(\frac{-{d_k}^2}{2d_{\text{m}}^2}\right)} \tag{8.7}$$

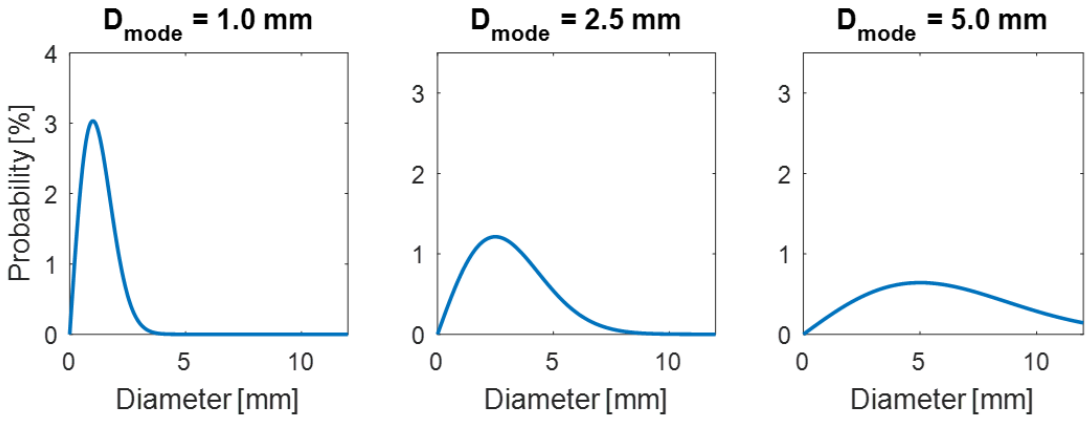

Figure 8.7: Rayleigh distribution of varying bubble modes

where P_{d} is the probability density function and d_{m} is the mode bubble diameter. To ensure consistency across all trials the bubble size distribution used here will range from 0.0 mm to 12.0 mm with a diameter increments of 0.05 mm, in keeping with the modeling done by Slettebø (Slettebø, 2009). The standard diameter mode used will be 2.5 mm, however this value will be varied to show separator performance across a range of different bubble size distributions. Bubble sizes below 0.05 mm are not usually considered in gas-liquid separator designs (GPSA, 2016). Rayleigh distributions with different diameter modes can be seen in Figure 8.7. The bubble density within the liquid surface area is assumed to be constant unless otherwise noted. The individual diameter probability is then found by

$$p_k = \frac{P_{\mathrm{d},k}}{\sum_{k=1}^{K} P_{\mathrm{d},k}(d_k|d_{\mathrm{m}})} \tag{8.8}$$

where p_{k} is the individual diameter probability. The bubble density per vertical section is kept constant for the inlet conditions.

8.1.4 Bubble Velocity Calculation

The method of calculating bubble velocities was adapted from Slettebø's work on modeling bubble rise in viscous fluids as mentioned in Section 3.3 (Slettebø, 2009).

Using the Equations 3.10 – 3.15, an iterative process for the bubble velocity calculation is set up where the bubble diameter along with an initial bubble velocity guess are required. Using the bubble diameter and the bubble velocity guess, a new bubble velocity can be calculated and the iterative process repeated. Within the modeling framework presented in this work, the threshold error value on bubble velocity calculation was set to 10^{-5} m/s. When the difference between the guesses and calculated bubble velocity is less than this threshold value, the iterative calculation is terminated.

8.1.5 Mass Transfer Properties

The challenge in formulating a generalized horizontal gas-liquid separator model is that mass transfer characteristics can vary between different gas-liquid combinations. For the degassing model presented here, the mass transfer properties will be taken from the methane-dodecane reference hydrocarbon system tested in Chapter 7. If the inlet solution is supersaturated, determining the driving force for mass transfer along with the rate at which the mass transfer occurs, the solutes solubility with respect to the liquid solvent and the diffusivity of solute in the solvent are needed. The solubility of methane in dodecane is calculated using the simplified Henrys law shown in Equation 3.4. The Henrys constant of $H = 25.7$ MPa, as seen in Section 7.5, was used. For a binary system, the equilibrium solute concentration is calculated using

$$C^* = \frac{x_{\mathrm{g}}\rho_{\mathrm{l}}}{x_{\mathrm{g}}MW_{\mathrm{g}} + x_{\mathrm{l}}MW_{\mathrm{l}}} \tag{8.9}$$

Assuming the supersaturation ratio is specified for the inlet conditions, the supersaturated solute concentration can be found using

$$C_{\mathrm{b}} = C^*(\xi + 1) \tag{8.10}$$

where the solution is considered supersaturated if $\xi > 0$.

The diffusion coefficient of gases in liquids at a given temperature and pressure is primarily a function of the liquid phase viscosity. Jamialahmadi et al. found that changes in the diffusion coefficient of methane in dodecane is well accounted for by the liquid phase viscosity using (Jamialahmadi et al., 2006)

$$D = a_0 \mu_{\mathrm{l}}^{a_1} \tag{8.11}$$

where $a_0 = 2.4719 \cdot 10^{-9}$ and $a_0 = -1.0006$ for methane in dodecane at 45 °C. The viscosity term in Equation 8.11 is in units of mPa $\cdot$ s while the calculated diffusivity coefficient is in m^2/s. For the purposes of this model, it is assumed that the above correlation works for methane in dodecane at 50 °C as well.

Using the solid surface small eddy model verified for this hydrocarbon system in Section 7.8, the mass transfer coefficient can be calculated using Equation 4.15. The energy dissipation rate can be approximated using (Kawase et al., 1987)

$$\epsilon = \frac{g Q_{\mathrm{g}}}{A_{\mathrm{l}}} \tag{8.12}$$

where g is the gravity acceleration constant and A_{l} is the cross-sectional area of the liquid flow. The change in the solute concentration due to gas-liquid mass transfer can then be calculated using (reformulated from Equation 4.8)

$$\frac{dC_{\mathrm{b}}}{dt} = \frac{k_{\mathrm{l}} A}{V_{\mathrm{l}}} (C_{\mathrm{b}} - C^*) \tag{8.13}$$

The rate of bubble growth due to mass transfer can be calculated using (Liger-Belair et al., 2005)

$$k_{\mathrm{b}} = \frac{dd}{dt} = \frac{6RT}{P} k_{\mathrm{l}} (C_{\mathrm{b}} - C^*) \tag{8.14}$$

where k_{b} is the bubble growth constant. Integration yields

$$d_{j+1} = k_{\mathrm{b}j}\Delta t + d_j \tag{8.15}$$

In this manner, bubble growth can be calculated between time steps j and $j+1$ from gas coming out of solution. As gas evolves out of solution, this also changes the bulk concentration as time progresses. From Equation 8.13, the bubble area available for mass transfer can be calculated at each time step

$$A_j = \sum_{i=1}^{I}\sum_{k=1}^{K} N_{ijk}(\pi d_{ijk}^2) \tag{8.16}$$

summing the surface area of bubbles within each vertical segment. Note that as the entrained gas fraction, x_{eg}, approaches zero, the bubble area available for mass transfer also approaches zero. The bubble volume and bubble count per time step can be calculated in a similar manner

$$V_j = \sum_{i=1}^{I}\sum_{k=1}^{K} N_{ijk}\left(\frac{\pi}{6}d_{ijk}^3\right) \tag{8.17}$$

$$N_j = \sum_{i=1}^{I}\sum_{k=1}^{K} N_{ijk} \tag{8.18}$$

By taking the cross-sectional area of the bubble in liquid, the entrained gas flow per time step can also be calculated

$$Q_{\mathrm{eg},j} = v_l \sum_{i=1}^{I}\sum_{k=1}^{K} N_{ijk}\left(\frac{\pi}{4}d_{ijk}^2\right) \tag{8.19}$$

Using the bubble surface area and bubble volume, in conjunction with the bubble count per time step, the average bubble surface and average bubble volume per time step can be calculated

$$A_{\text{ave},j} = \frac{A_j}{N_j} \tag{8.20}$$

$$V_{\text{ave},j} = \frac{V_j}{N_j} \tag{8.21}$$

With the average bubble volume per time step, the bubble frequency is then calculated

$$f_j = \frac{Q_{\text{eg},j}}{V_{\text{ave},j}} \tag{8.22}$$

Finally, the change in volumetric interfacial overtime within the separator can be calculated using

$$a_j = \frac{f_j A_j t_{\text{res}} + A_{\text{b}}}{V_{\text{l}}} \tag{8.23}$$

where A_{b} is the bulk gas-liquid interfacial area. Note that as the entrained gas fraction approaches zero, the volumetric interfacial area will approach the bulk gas-liquid interfacial area. Equation 8.23 allows the volumetric interfacial area to be quantified from both the bubble surface area within the liquid as well as the bulk gas-liquid interfacial area.

Partially solving Equation 4.8 from $t = 0$ to some time in the future $t = t_{j=x}$ yields

$$\ln\left(\frac{C_{j=x} - C^*}{C_0 - C^*}\right) = -k_{\text{l}} \int_0^{t_{j=x}} a dt \tag{8.24}$$

There is no explicit mathematical form for the change in the interfacial volumetric area, a, with respect to time since this value is determined both by the rate at which bubbles grow per time step as well as the rate at which bubbles exit the solution. The right-hand side of the above equation can, however, be approximated numerically using the trapezoidal rule where

$$\int_0^{t_{j=x}} a dt \approx \sum_{j=1}^{j=x} \frac{a_{j-1} + a_j}{2} \Delta t \tag{8.25}$$

As the time domain is more finely subdivided, the error associated with the numerical integration will decrease. Using Equation 8.24 in conjunction with Equation 8.25, the new bulk concentration at each time step, C_j, after the interfacial area is accounted for, can be found. For each new bulk concentration, an associated supersaturation ratio, ξ_j, can also be calculated using Equation 8.10. The degree of supersaturation, once the separator residence time is reached, is assumed to carry into the exiting liquid stream further contributing to gas carry-under down the line.

8.2 Standard Model Conditions

In order to effectively explore the functionality of the developed degassing model, standard model conditions must be first established. These standard model conditions, listed in Table 8.1 will be used to form the base case for separator performance. From the base case, sensitivity analysis can be run to explore the impact of a single variable on the separation performance. The standard model conditions are based on a hypothetical fluid and not necessarily reflective of an actual crude oil. Typically, horizontal gas-liquid separators have a diameter to length ratio from 3 to 5 (Stewart and Arnold, 2008). For the purposes of this model, that ratio is maintained at 4 with a vessel radius of 1 m and the vessel length of 8 m. The total liquid volume within the separator is also maintained at 50 % of the total vessel volume. If the liquid residence time is varied, the liquid flow rate is adjusted in order to keep the total liquid volume, $V_\mathrm{l} = Q_\mathrm{l} \cdot t_\mathrm{r}$, at half of the total vessel volume. Bubbles larger than 12 mm have such a high initial velocity that they rise to the bulk interface almost instantaneously, hence their effect on the liquid dynamics over time can be considered negligible. The gas and liquid molecular weights are taken from the methane and dodecane system tested in the previous chapter.

Table 8.1: Standard model conditions

Model Input	**Value**
Bubble distribution increment	0.05 mm
Bubble distribution maximum	12 mm
Bubble distribution minimum	0.0 mm
Bubble distribution mode	2.5 mm
Entrained gas fraction	0.105
Gas density	66.6 kg/m^3
Gas molecular weight	16.0 g/mol
Liquid density	925 kg/m^3
Liquid volume fill	50%
Liquid molecular weight	170.3 g/mol
Liquid residence time	60 s
Liquid viscosity	100 cP
Pressure	10 MPa
Supersaturation ratio (if applicable)	0 (0.3)
Surface tension	20 dyne/cm
Temperature	50 °C
Vessel length	8 m
Vessel radius	1 m

The entrained gas fraction is estimated by assuming the inlet gas-liquid stream is entering the separator as a jet plunging into the bulk liquid within the separator, similar to the procedure outlined by Bothamley (Bothamley, 2013*b*). The entrained gas to liquid ratio can then be estimated using the correlation developed by Biń (Biń, 1993)

$$\frac{Q_{\mathrm{eg}}}{Q_{\mathrm{l}}} = 0.04 Fr_{\mathrm{j}}^{0.28} \left(\frac{L_{\mathrm{j}}}{d_{\mathrm{n}}} \right)^{0.4} \tag{8.26}$$

where Q_{eg} is the entrained gas volumetric flow rate, Q_{l} is the liquid flow rate, Fr_{j} is the jet Froude number, L_{j} is the length of the jet, and d_{n} is the nozzle diameter. The jet Froude number can be calculated using

$$Fr_{\mathrm{j}} = \frac{v_{\mathrm{l}} - v_{\mathrm{l},0}}{\sqrt{g d_{\mathrm{j}}}} \tag{8.27}$$

where v_{l} is the jet velocity, $v_{\mathrm{l},0}$ is the jet velocity at which entrainment commences,

g is the gravity acceleration constant, and d_{j} is the jet diameter. The jet diameter can be approximated as the diameter of the nozzle, d_{n}. The jet velocity at which entrainment commences usually varies from 0.8 to 1.0 m/s (Smit, 2007).

From the vessel geometry and liquid residence time specified in Table 8.1, the liquid volumetric flow rate can be calculated as $Q_{\mathrm{l}} = 0.209$ m^3/s. Assuming the inlet feed enters through a 6 in pipe diameter (0.15 m), the liquid velocity is calculated as $v_{\mathrm{l}} = 11.5$ m/s. Taking $v_{\mathrm{l}} = 1.0$ m/s, the jet Froude number is calculated to be $Fr_{\mathrm{j}} = 8.57$. Finally, the jet length, L_{j}, is assumed to be half of the vessel radius, 0.5 m. The entrained gas ratio, $Q_{\mathrm{eg}}/Q_{\mathrm{l}}$ is calculated to be 0.117. Converting from ratios to fractions, the entrained gas faction is calculated to be 0.105. Larger inlet feed pipe diameters would further decrease the calculated entrained gas fraction.

8.2.1 Saturated Base Case

With the rate of supersaturation set to $\xi = 0$, the results of the base case separation can be seen in Table 8.2. For the above model conditions, 88.44 % of the total number of bubbles were removed, however 99.75 % of the bubble volume was removed since larger bubbles, which occupy a disproportionate amount of the total bubble volume, rise much faster than the smaller ones. Since the inlet supersaturation ratio is set to zero, there is no excess solution gas to be removed. This base case converged within two multi-pass model iterations, resulting in a mass balance error of 0.002 %.

The percent gas volume remaining (in the liquid) is calculated by summing the total remaining entrained gas at the outlet and dividing by the total liquid flow plus the total remaining entrained gas flow. If the exiting liquid is supersaturated, the volume of gas that will eventually evolve out of solution (until $\xi = 0$) can also be calculated. This volume equivalent of excess solution gas still in the liquid is added to the percent gas volume remaining calculation as additional entrained gas.

For the standard model conditions without supersaturation, the percent gas volume remaining is low at 0.03 %. This is an intuitive result given that the majority of the entrained gas volume has been removed at these process conditions.

Table 8.2: Base case model outputs with $\xi = 0$

Model Output	Value
Percent bubbles removed	88.44 %
Percent bubble volume removed	99.75 %
Percent solution gas removed	NaN
Percent gas volume remaining	0.03 %

Figure 8.8 shows the bubble number density within the liquid over time at the standard model conditions without supersaturation. Initially the bubble density is constant at $t = 0$ throughout the entire liquid height, however, as time progresses and the fluid moves through the length of the separator, the bubble density at the bottom of the liquid (bottom of the separator) decreases as those bubbles rise in the liquid. The bubble density in the middle and top of the liquid takes longer to decrease in magnitude since the bubbles that rise out of those sections are being continually replaced by bubbles from the sections below. Once the liquid residence time within the separator is reached, the remaining entrained bubbles are assumed to carry-under in the exiting liquid stream.

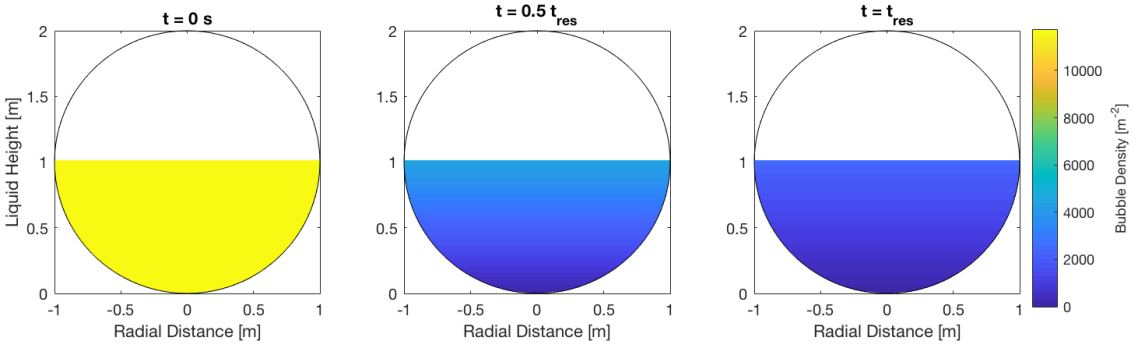

Figure 8.8: Bubble density plot of base case separation with $\xi = 0$

The change in the volumetric interfacial area available for mass transfer at the standard model conditions can be seen in Figure 8.9. This volumetric interfacial area

available for mass transfer is a product of both the interfacial area of the entrained bubbles as well as the bulk gas-liquid interfacial area, calculated from Equation 8.16. As the bubbles leave the bulk liquid, the total volumetric interfacial area approaches the bulk gas-liquid volumetric interfacial area.

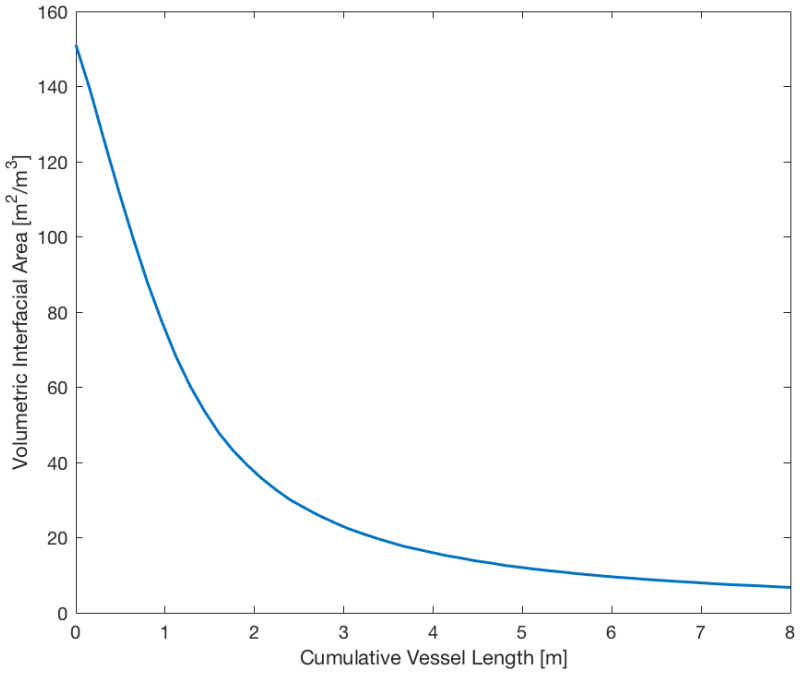

Figure 8.9: Change in the volumetric interfacial area available for mass transfer at base case conditions with $\xi = 0$

8.2.2 Supersaturated Base Case

With the rate of supersaturation set to $\xi = 0.3$, the results of the base case separation can be seen in Table 8.3. The additional supersaturation improved percent bubbles removed when compared to the non-supersaturated base case seen in Table 8.2 due to bubble growth experienced within the supersaturated medium. While the total number of bubbles separated increased, the total bubble volume separated decreased by 0.10 %. Though not a significant decrease, this is due to the fact that the method of calculating the percent bubble volume removed compares the total bubble volume at the inlet and outlet of the separator model. Even though there are

fewer bubbles present at the outlet compared to the saturated base case, the bubbles remaining at that point had the chance grow within the supersaturated solution and expand in volume resulting in essentially the same rate of bubble volume removed.

The rate of solution gas removal for the supersaturated base case was, however, low. Only 2.33 % of the excess solution gas was predicted to be removed from the supersaturated solution within the separator liquid residence time. While the volumetric interfacial area in the separator model is initially similar in magnitude to that of a bubble column (the averaged value over the length of the separator was $a = 33.1$ m^2/m^3), the 60 s residence time limited the total amount of excess solution gas removal (Stegeman et al., 1996). Furthermore, as the liquid progresses through the separator, the area available for mass transfer decreases as bubbles rise out of solution. The total area available for mass transfer approaches the bulk gas-liquid interfacial area quicker in a supersaturated solution since all bubbles present will have an increased bubble velocity due to their growth within the liquid. The resulting percent gas volume remaining was calculated to be 19.22 %. Since most of the entrained gas volume is separated at these conditions, this gas volume remaining is almost entirely from the excess solution gas yet to be separated.

Table 8.3: Base case model outputs with $\xi = 0.3$

Model Output	Value
Percent bubbles removed	95.78 %
Percent bubble volume removed	99.60 %
Percent solution gas removed	2.33 %
Percent gas volume remaining	19.22 %

Figure 8.10 shows the bubble number density within the liquid over time at the standard model conditions with supersaturation. The bubble density at $t = 0$ is identical to the initial condition shown in Figure 8.8. As time progresses, the bubble density within the fluid drops off quicker in the supersaturated base case compared to the saturated base case. These results are consistent with the model outputs listed

in Tables 8.2 – 8.3.

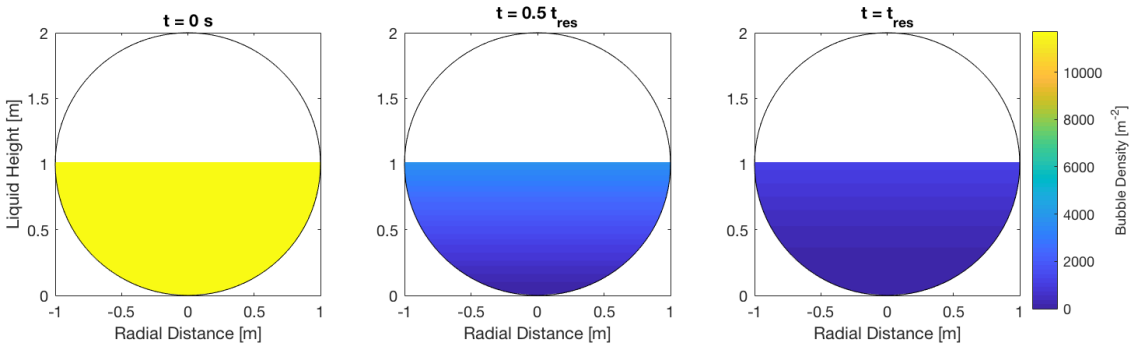

Figure 8.10: Bubble density plot of base case separation with $\xi = 0.3$

8.2.3 Numerical Stability

The model stability was investigated across a variable number of height steps (vertical incrementations I) and time steps (horizontal incrementation J). Using a variable total number of height and time steps, the stability of the percent bubbles removed model output is shown in Figure 8.11.

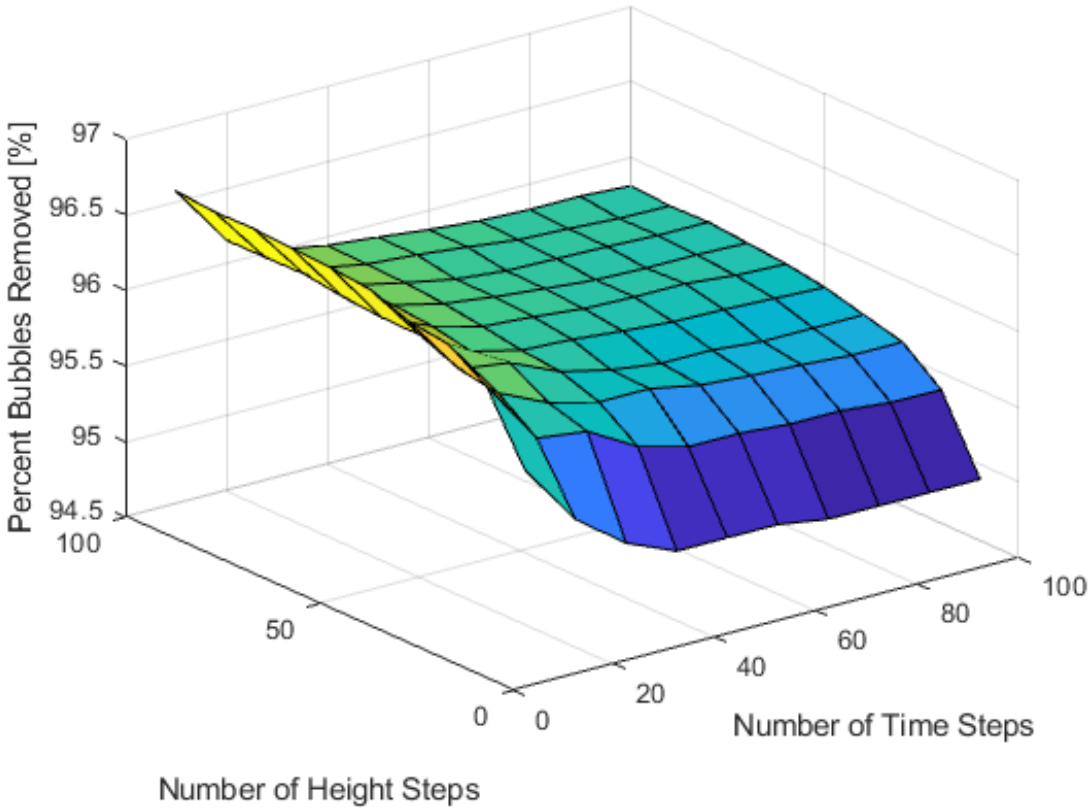

Figure 8.11: Percent bubbles removed as a function of variable height and time steps

The stability of the percent bubble volume removed model output using a variable total number of height and time steps is shown in Figure 8.12.

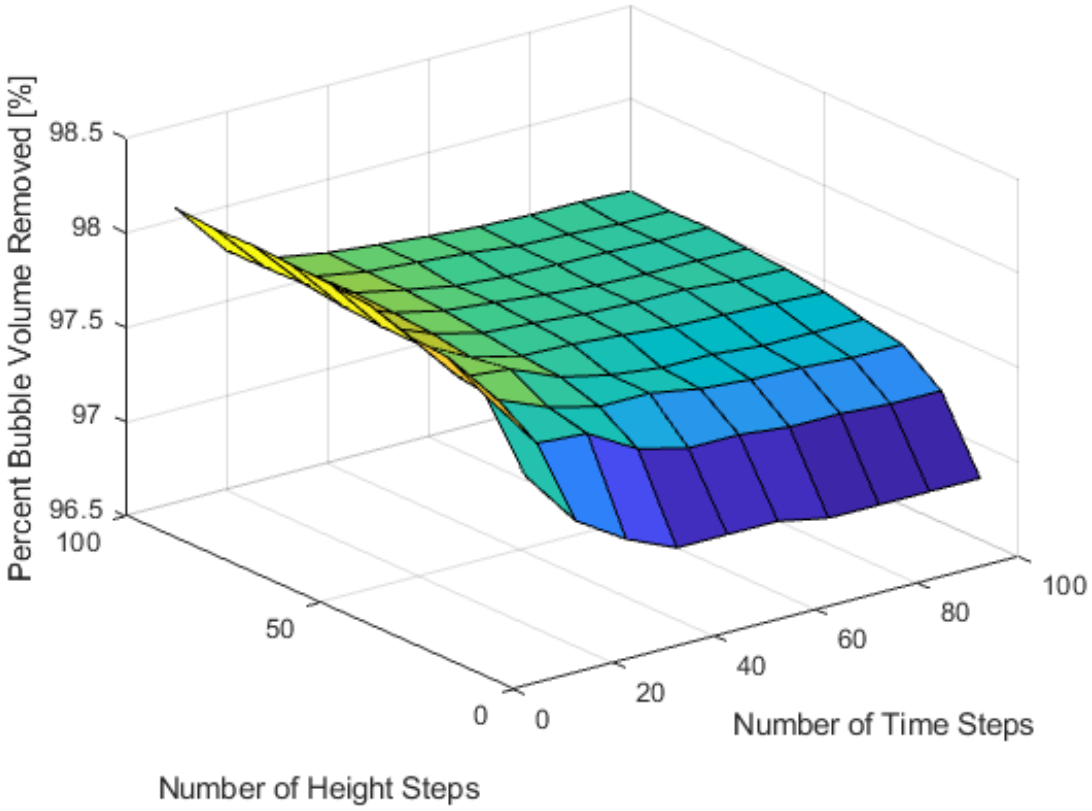

Figure 8.12: Percent bubble volume removed as a function of variable height and time steps

Finally, the stability of the percent solution gas removed model output using a variable total number of height and time steps is shown in Figure 8.13.

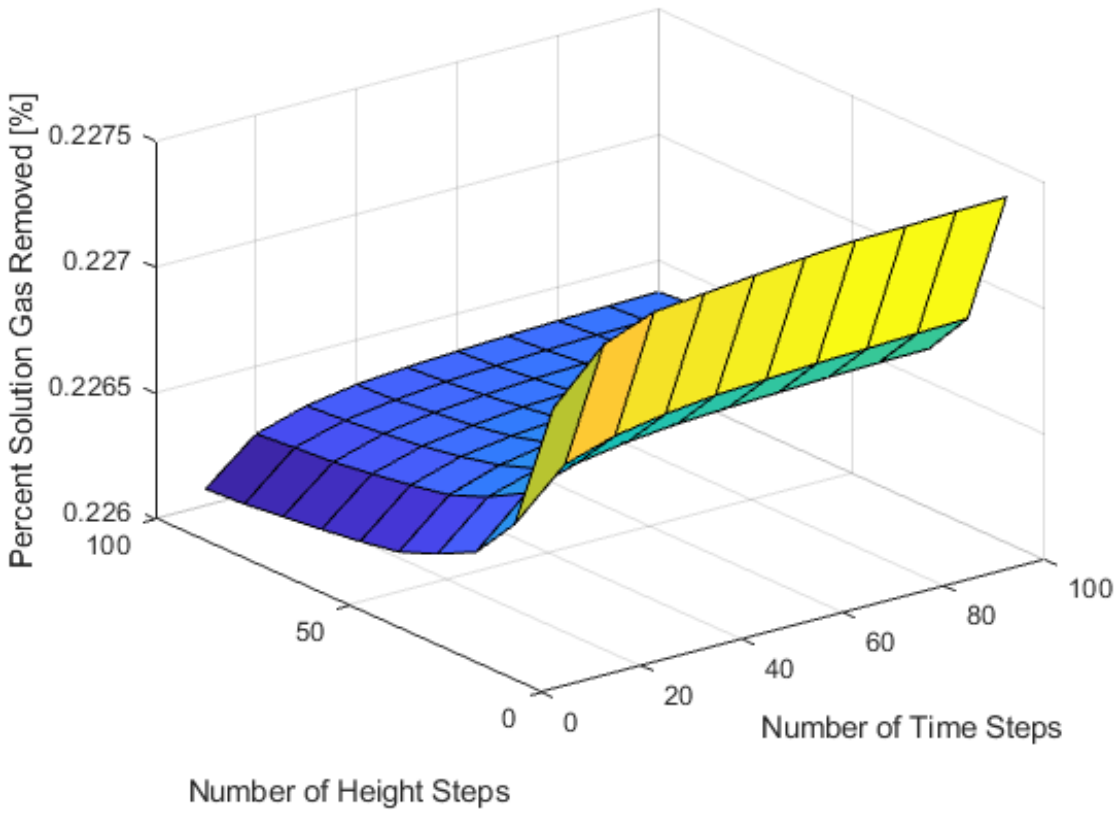

Figure 8.13: Percent solution gas removed as a function of variable height and time steps

As seen in Figures 8.11 – 8.13, an increase in both the total number of time and height steps leads to a convergence of the model's outputs. This behavior is characteristic of a numerically stable model. As such, all modeling trials presented in this work are performed using a total number of heights steps set to $I = 100$ and a total number of time steps set to $J = 100$. The change in the absolute output of the model at these conditions was less than 0.01 %. This numerical stability was maintained for different model inputs.

8.3 Saturated Fluid Analysis

8.3.1 Density Sensitivity Analysis

For the first part of the analysis, only saturated liquid solutions ($\xi = 0$) will be considered. Sensitivity analyses can be performed by varying individual model

parameters and mapping the response. Unless explicitly stated, the standard model conditions listed in Table 8.1 are used for all model inputs. According to the API degassing guidelines seen in Table 1.1, the separator performance is expected to be a strong function of liquid density. The liquid density is varied from 850kg/m^3 to 1000kg/m^3 in increments of 25kg/m^3 (35 °API $\approx$ 840kg/m^3, 10 °API $\approx$ 990kgm^3). While it is difficult to predict exactly what bubble distribution mode, D_{m}, will exist for a given separator's inlet stream, a robust gas-liquid separator design should be able to handle a variety of bubble distributions while still maintaining good separation performance. The bubble distribution mode is varied along with the liquid density in sensitivity analysis presented in Figures 8.14 – 8.16.

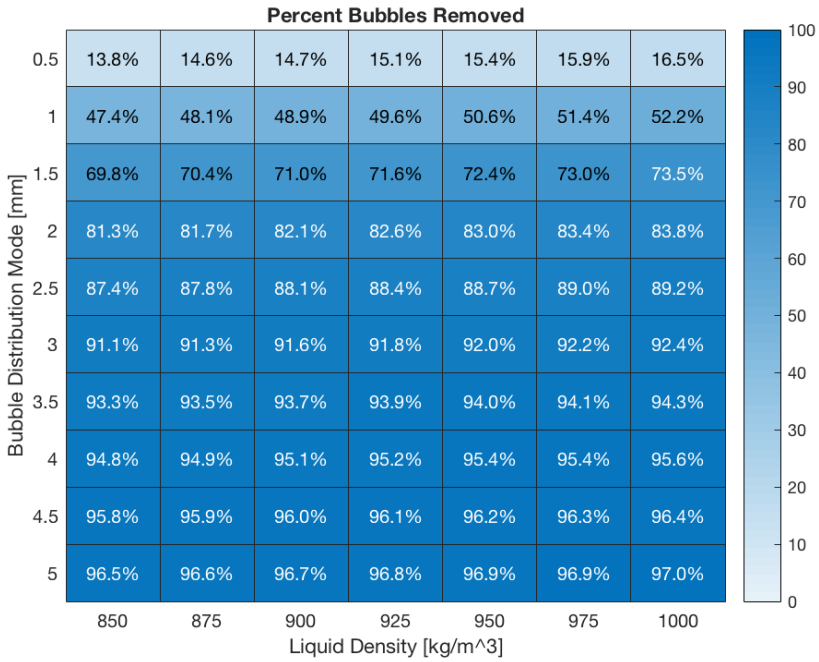

Figure 8.14: Sensitivity analysis of the effect of liquid density and bubble distribution mode with no supersaturation on percent bubbles removed

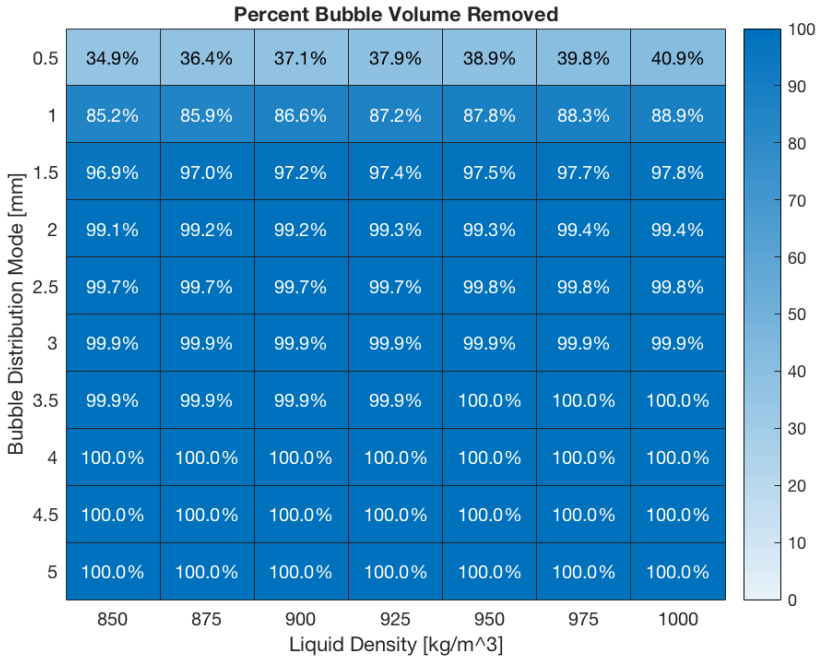

Figure 8.15: Sensitivity analysis of the effect of liquid density and bubble distribution mode with no supersaturation on percent bubble volume removed

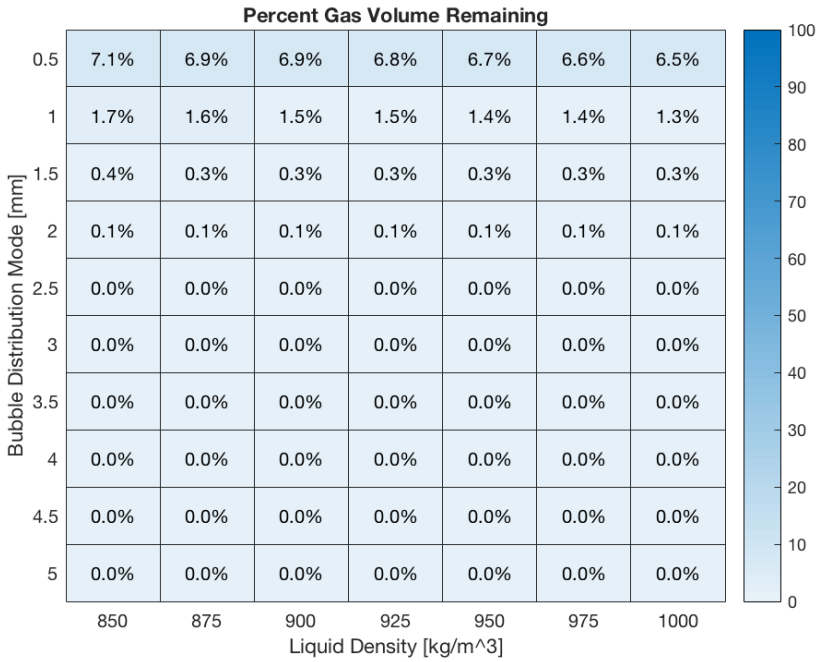

Figure 8.16: Sensitivity analysis of the effect of liquid density and bubble distribution mode with no supersaturation on percent gas volume remaining

The liquid density is seen to have a relatively weak effect on the separation

performance; variations in the bubble distribution mode have much more pronounced effects on the separation performance. Higher liquid densities lead to slightly better separation due to the increased density differential between the gas and liquid phases, increasing the separation driving force exerted by buoyancy. This finding is consistent with the reasoning presented in Section 2.4.2.

8.3.2 Viscosity Sensitivity Analysis

While oil densities can vary roughly from 5 to 45 °API, oil viscosities can range several orders of magnitude. Figures 8.17 – 8.19 present the sensitivity analysis varying the bubble distribution mode along with the liquid viscosity. The liquid viscosity is varied from 1 to 1000 cP to illustrate a broad range of liquid viscosities.

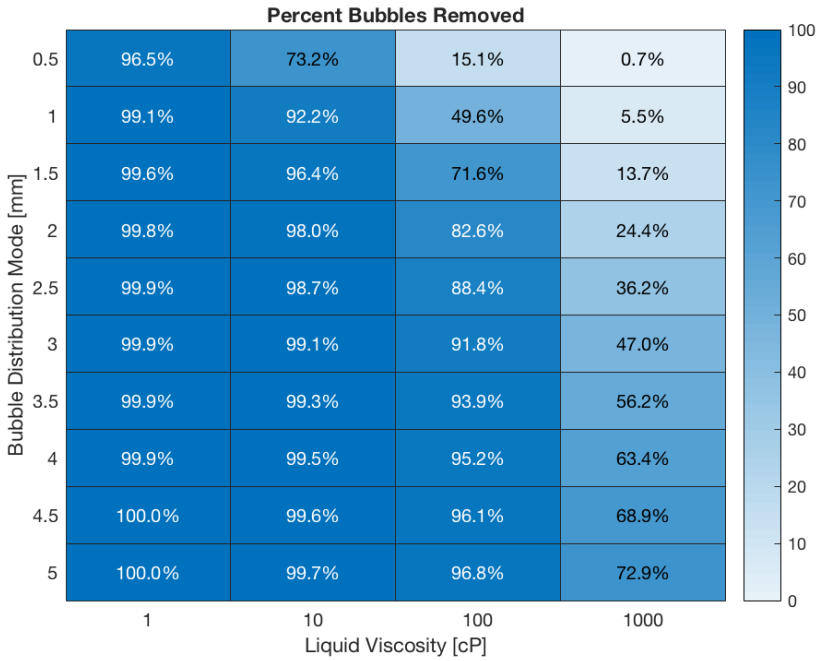

Figure 8.17: Sensitivity analysis of the effect of liquid viscosity and bubble distribution mode with no supersaturation on percent bubbles removed

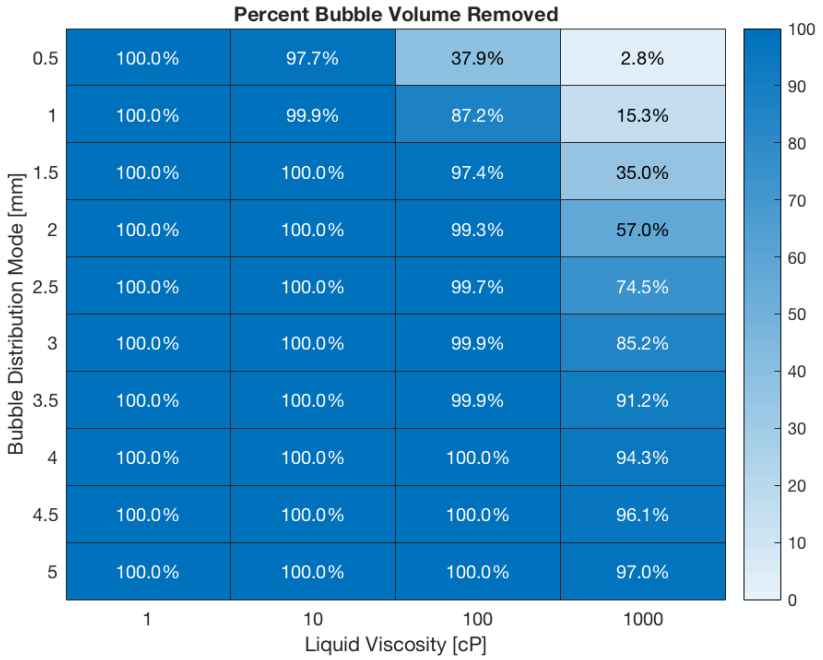

Figure 8.18: Sensitivity analysis of the effect of liquid viscosity and bubble distribution mode with no supersaturation on percent bubble volume removed

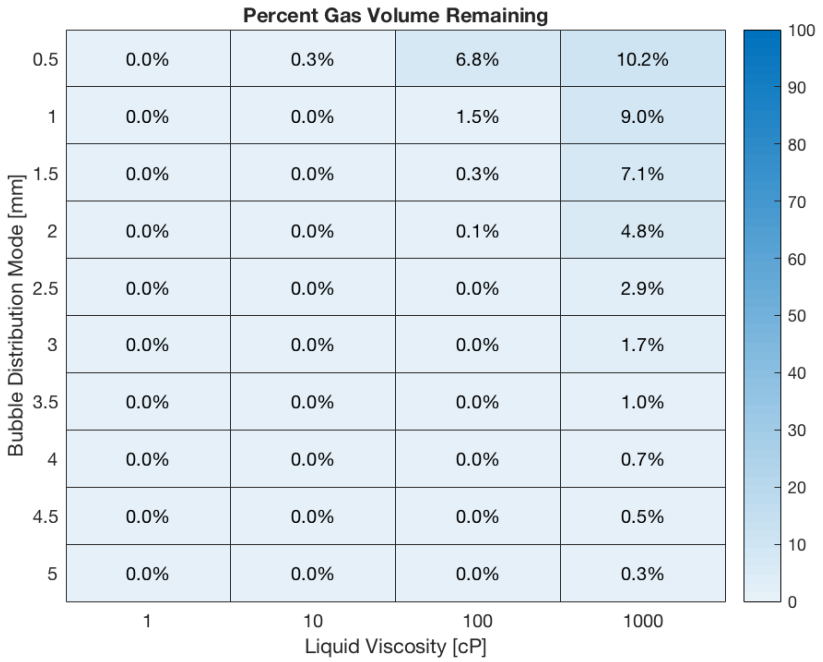

Figure 8.19: Sensitivity analysis of the effect of liquid viscosity and bubble distribution mode with no supersaturation on percent gas volume remaining

As expected, separation performance deteriorates with an increasing liquid

viscosity and decreasing bubble distribution mode, with a drastic decrease in performance observed at $\mu_l = 1000$ cP. The effects of the liquid phase viscosity on separation performance are much larger than those observed with changes in the liquid density. Of the physical properties, liquid viscosity was found to have the largest impact on separation performance. This strong dependence on the liquid viscosity with minor effects from variations in the liquid density is in contradiction to what should be expected according to the API 12J guidelines. The source of this discrepancy could be largely attributed to the fact that as crude oils become denser, they often become more viscous as well, as seen in Figure 2.11.

8.3.3 Inlet Bubble Density Variation

Apart from the physical properties and bubble size distribution, the inlet bubble density can also be varied within the horizontal separator model. The bubble density specifies how the bubble distribution is spread vertically through the initial liquid surface entering the separator. For the standard model conditions, the bubble density is constant across the inlet liquid surface. Variations in the bubble density will have a definitive effect on the separation performance. For example, if the bubble density is highest at the top of the inlet stream, more bubbles will be separated compared to the case of equal bubble density throughout the liquid. The inverse is also true: when bubble density is highest at the bottom of the inlet stream, separation will always be worse compared the equal bubble density case. Figure 8.20 depicts three different inlet bubble density scenarios, all containing the same total number of bubbles in the inlet stream. The worst-case bubble density has peak bubble density at the bottom of the liquid height, the base-case bubble density has a constant equally distributed bubble density throughout the inlet surface, while the best-case bubble density has the highest bubble concentration at the very top of the liquid. For the worse-case and best-case scenarios, the bubble density is varied linearly throughout

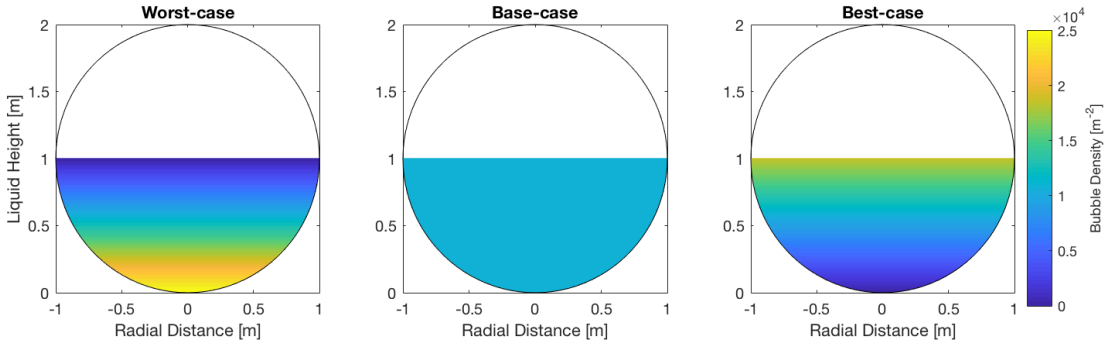

Figure 8.20: Horizontal separator inlet depicting the worst-case, base-case and best-case bubble density variations

the liquid height. By compiling all three scenarios, a separator's performance can be evaluated across the total theoretical range of potential inlet bubble densities.

Figures 8.21 – 8.23 show the effect of residence time and bubble distribution mode on the percent gas volume remaining at the liquid outlet for different liquid viscosities.

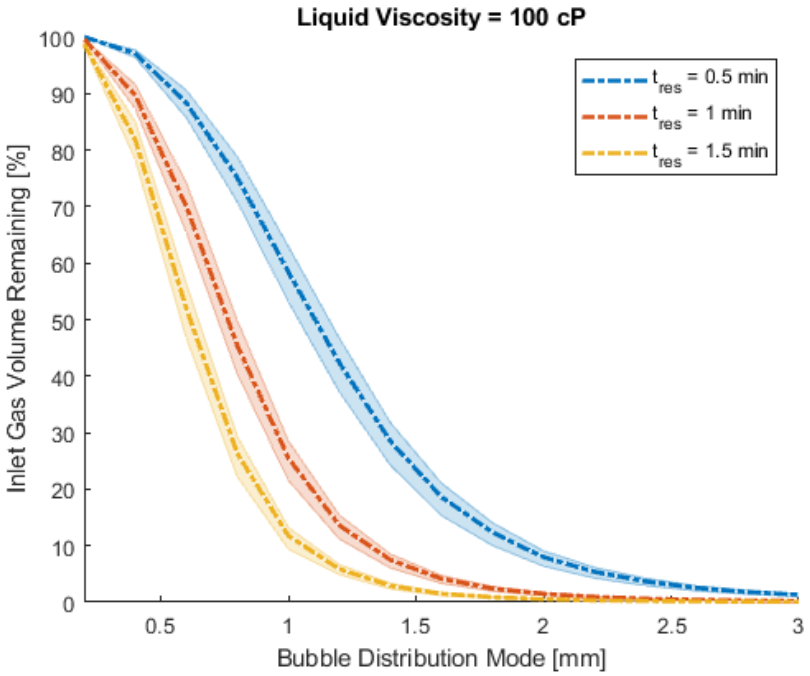

Figure 8.21: Effect of separator residence times on inlet gas volume remaining on liquid viscosity of 100 cP

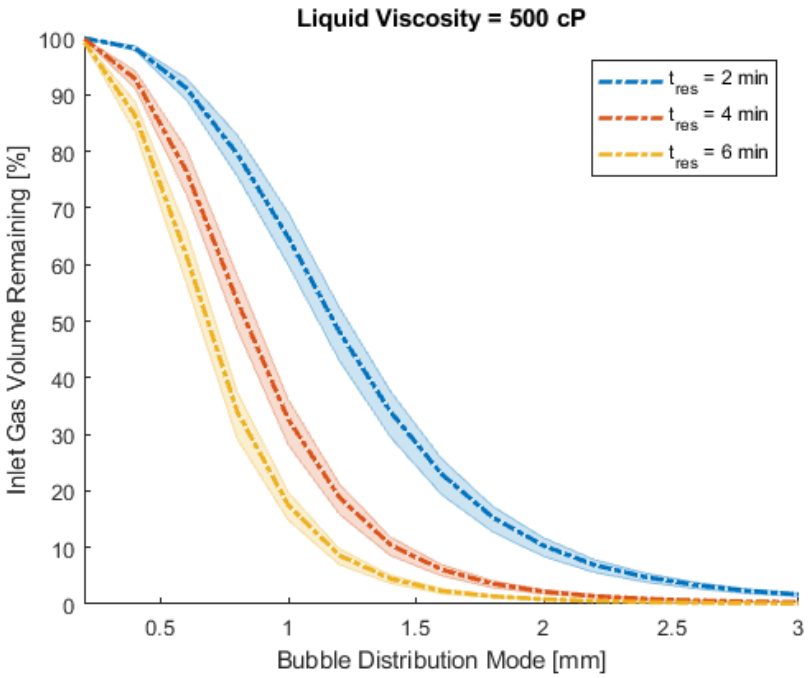

Figure 8.22: Effect of separator residence times on inlet gas volume remaining on liquid viscosity of 500 cP

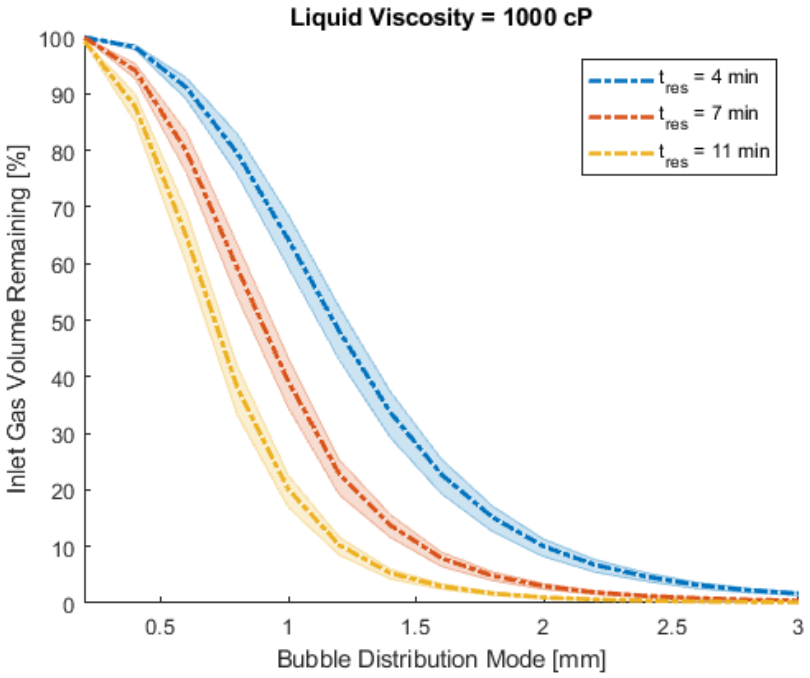

Figure 8.23: Effect of separator residence times on inlet gas volume remaining on liquid viscosity of 1000 cP

The bands around each residence time curve are generated by using the best

and worst-case inlet bubble densities show in Figure 8.20, where the best-case bubble density represents the lower range of the band and the worst-case bubble density the upper range. The center line is drawn using the base-case inlet bubble density. Arranging the data in this format, it becomes clear how increased liquid viscosities require much greater residence times to maintain equivalent separation performance. For example, to achieve separation performance similar to 100 cP liquid with a 60 s residence time would require a 7 min residence time at a liquid viscosity of 1,000 cP. The importance of good bubble size management is also highlighted. Relatively small changes in the bubble distribution mode, especially around the curve's inflection point, can have very large effects of the separation performance.

8.3.4 Proposed Saturated Fluid Degassing Guidelines

If the remaining gas volume is held constant at 1% for the separator model, the required liquid residence times can be solved for using different bubble distribution modes and different liquid viscosities. The results of this exercise are shown in Table 8.4. The required liquid residence time increases linearly with increased liquid viscosities for a given bubble distribution mode. As the bubble distribution gets larger, the required liquid residence times to achieve 1% gas volume remaining become less demanding.

Table 8.4: Required liquid residence time to reach 1% remaining gas volume at different bubble distribution modes

Liquid Viscosity [cP]	Bubble Distribution Mode		
	1 mm	2 mm	3 mm
	Liquid Residence Time [min]		
1	0.13	0.1	0.09
10	0.35	0.15	0.1
50	1.31	0.38	0.2
100	2.51	0.67	0.33
250	6.2	1.59	0.73
500	12.3	3.11	1.42
750	18.4	4.65	2.09
1000	24.6	6.18	2.77

8.4 Supersaturated Fluid Analysis

8.4.1 Viscosity Sensitivity Analysis

The same set of sensitivity analyses can be run using supersaturated fluids as was done for saturated fluids in Section 8.3. The effect of liquid viscosity and the bubble distribution mode is varied for a supersaturated solution of $\xi = 0.3$. The results of this analysis can be seen in Figures 8.24 – 8.27.

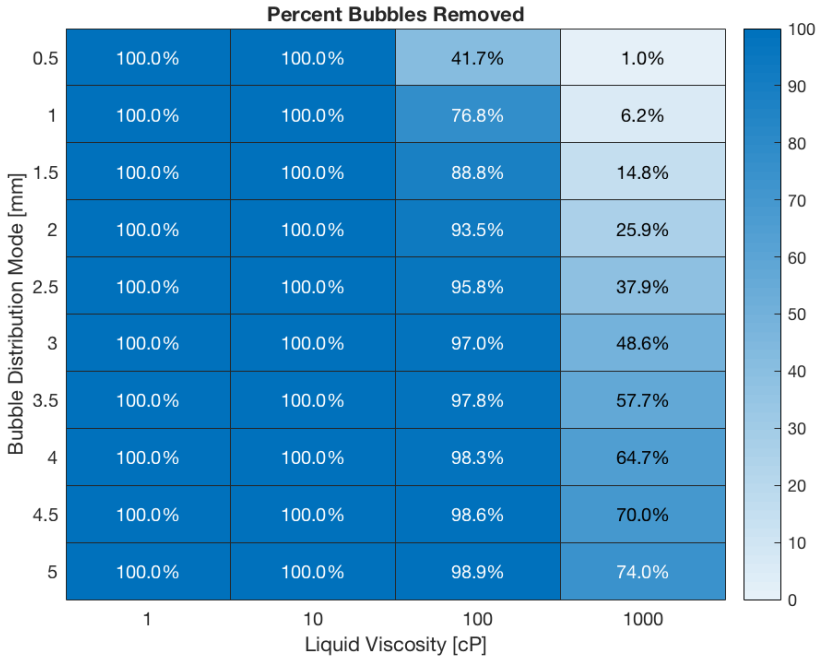

Figure 8.24: Sensitivity analysis of the effect of liquid viscosity and bubble distribution mode with supersaturation on percent bubbles removed

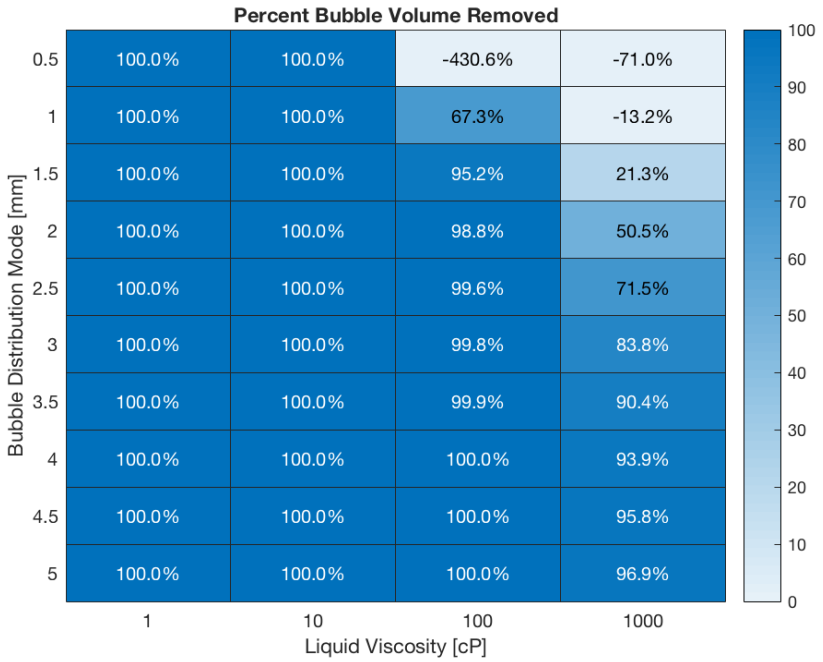

Figure 8.25: Sensitivity analysis of the effect of liquid viscosity and bubble distribution mode with supersaturation on percent bubble volume removed

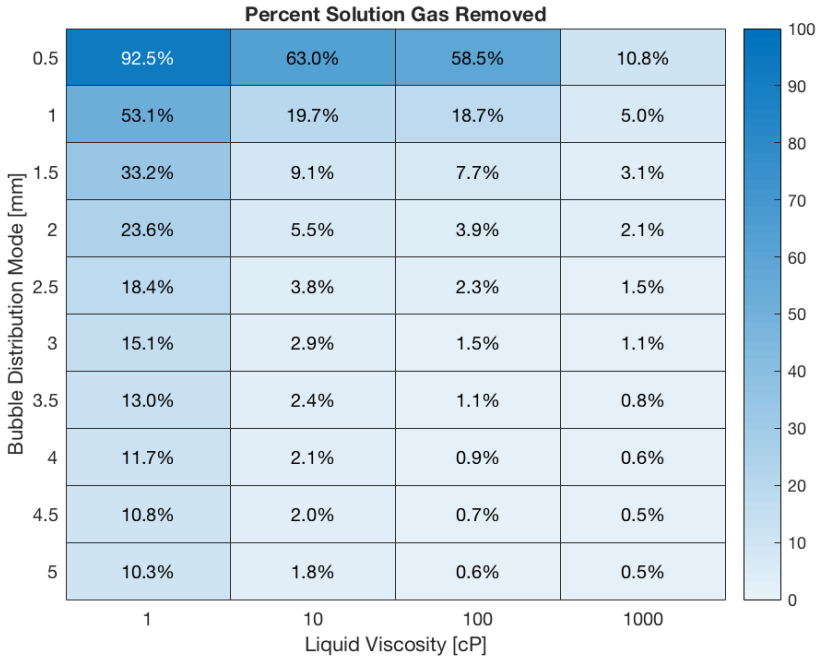

Figure 8.26: Sensitivity analysis of the effect of liquid viscosity and bubble distribution mode with supersaturation on percent solution gas removed

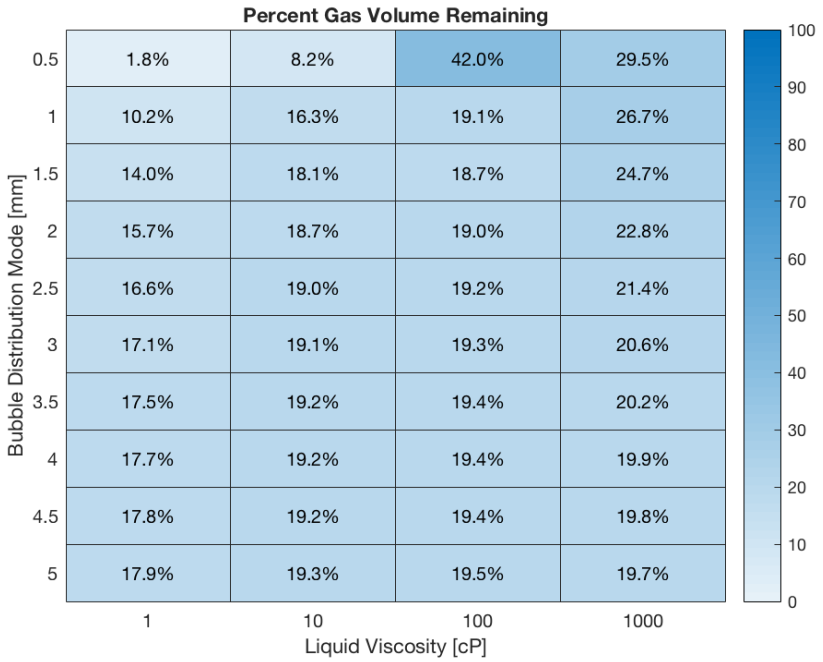

Figure 8.27: Sensitivity analysis of the effect of liquid viscosity and bubble distribution mode with supersaturation on percent gas volume remaining

While the degassing performance decreases with increased liquid viscosities,

similar to the trends seen in the saturated fluid analysis, there are some key differences in the supersaturated solution results. At small bubble distribution modes and high liquid viscosities, the percent bubble volume removed is negative in the most extreme cases, as seen in Figure 8.25. For these conditions, the bubble separation was so poor that more volume was generated within the liquid (due to bubble growth) than was separated. This poor entrained gas separation is confirmed by the percent bubbles removed results at the same conditions, as seen in Figure 8.24. Interestingly, the worst conditions from the perspective of bubble volume removed was the second most viscous setting (100 cP) and the small bubble distribution mode tested. While the bubble volume performance at the most viscous level (1,000 cP) is obviously bad, the performance deteriorates further at the next lowest viscosity since the bubble growth is faster at these conditions while the entrained gas separation still remains poor. Stepping down further in the viscosity to 10 cP, the liquid is now inviscid enough to allow all entrained gas bubbles to be separated, increasing the bubble volume removed to 100 %.

The optimal conditions for solution gas removal are small bubble distribution modes (resulting in a larger volumetric interfacial area) and low liquid viscosities (resulting in larger mass transfer coefficients). Small bubble sizes promote increased solution gas removal while simultaneously decreasing the potential for entrained gas removal. These figures also illustrate the need for for bubbles to remove any significant amount of solution gas. For test conditions with larges bubble distribution modes, the entrained gas bubbles rise out of the liquid very quickly, leaving only the bulk gas-liquid interfacial area providing the majority of the area available for mass transfer. Clearly, conditions where the bulk gas-liquid interfacial area provides the majority of the area available for mass transfer are insufficient for any significant amount of solution gas removal.

8.4.2 Liquid Swelling

By varying the supersaturation ratio, the effect of liquid swelling can also be explored by comparing the change in the effective liquid volume. As the supersaturation ratio increases, the growth rate of the bubbles still in solution increases, though the bubble velocities also increase. As seen in Figure 8.28, the change in the effective liquid volume is minimal over a range of different supersaturation ratios. Comparing the saturated condition results ($\xi = 0$) to the model results at $\xi = 1.0$, the effective liquid volume only increases by roughly 0.2 %. At these conditions, the effect of liquid swelling is minimal in the separator model.

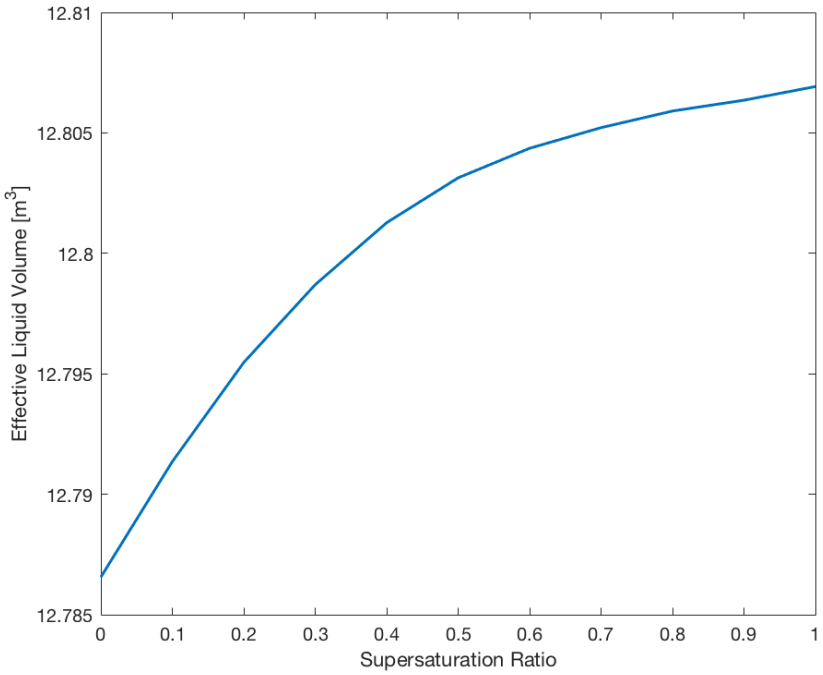

Figure 8.28: Change in the effective liquid volume with changing supersaturation ratio

8.4.3 Challenges in Removing Excess Solution Gas

Removing a majority of the excess solution gas from a supersaturated fluid within a horizontal separator was found to be challenging. From the supersaturated

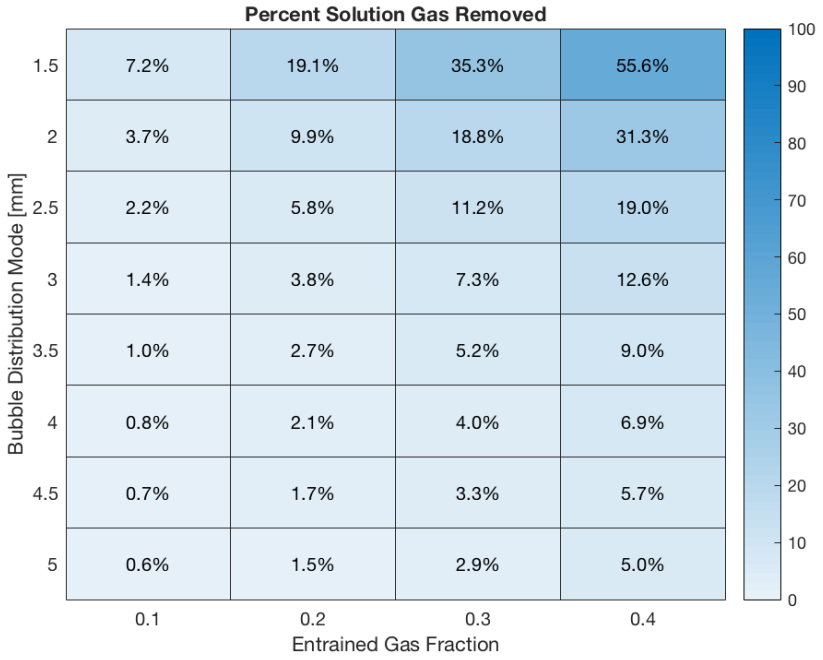

Figure 8.29: Sensitivity analysis of the effect of the entrained gas fraction and bubble distribution mode with supersaturation on percent solution gas removed

base case, the entrained gas fraction was varied along with the bubble distribution mode. The results of this analysis can be seen in Figure 8.29.

An increase in the entrained gas fraction increased the percent solution gas removal, though only the largest entrained gas fraction tested in combination with the smallest bubble distribution mode yielded a percent solution gas removal over 50 %. Increasing the entrained gas fraction and decreasing the overall size of the bubbles is, however, in opposition to the conditions desired for proper entrained gas separation. The effect of the liquid fill percent on the solution gas removal was also explored. These results can be seen in Figure 8.30.

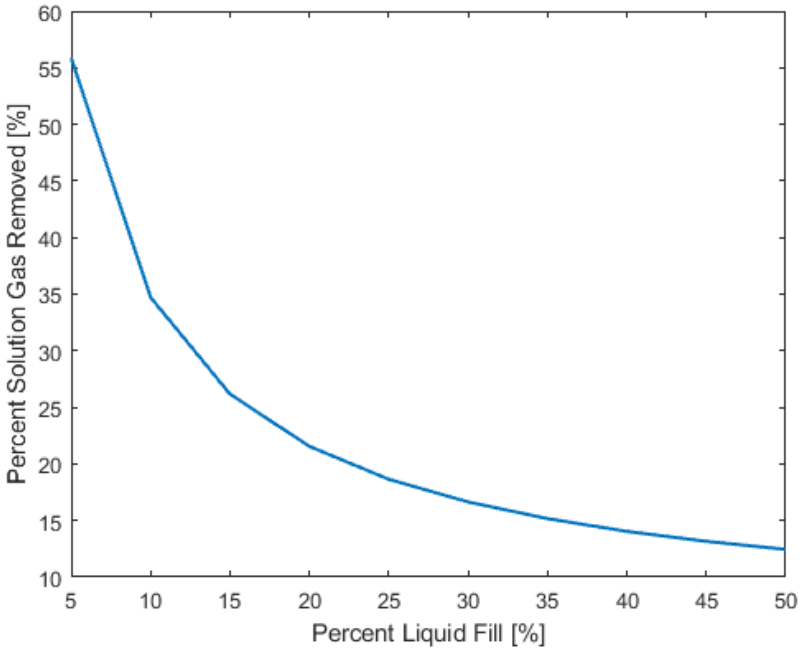

Figure 8.30: Effect of the percent liquid fill with supersaturation on percent solution gas removed

As the percent liquid fill is decreased, the volumetric interfacial area between the gas and the liquid increases, as seen in Equation 4.9, leading to increased rates of solution gas removal. At the standard model conditions, only a liquid fill of less than 10 % yielded a percent solution gas removal above 50 %. Increasing the percent solution gas removed significantly beyond 50 % at the standard model conditions was only accomplished by increasing the liquid residence time within the separator. The result of this exercise is seen in Figure 8.31.

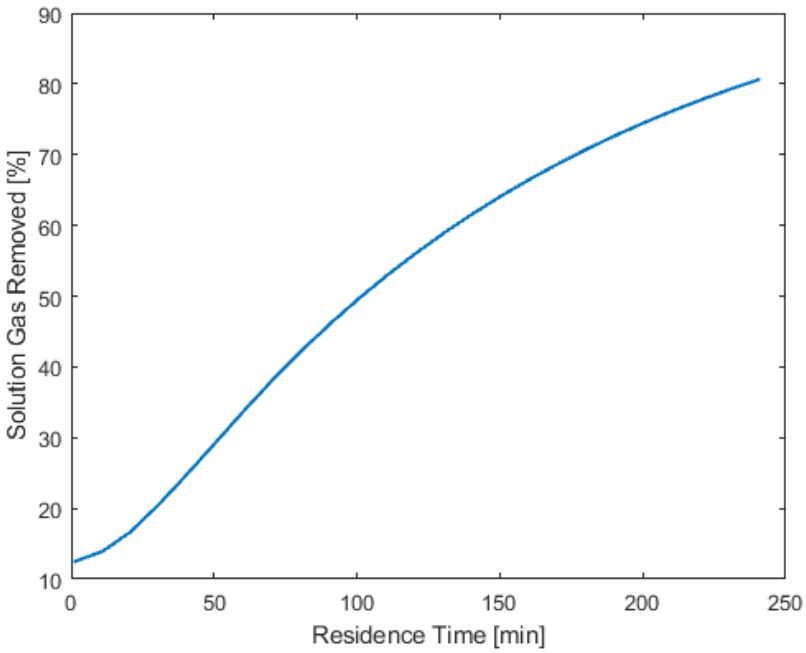

Figure 8.31: Effect of the liquid residence time with supersaturation on the percent solution gas removed

The liquid residence time was varied by maintaining a constant liquid flow rate but increasing the vessel length to achieve the desired residence time. As the liquid residence time was increased, the rate of solution gas removal also increased. With a liquid residence time of 4 hours, the percent solution gas removal exceeded 80 %. While increasing the liquid residence time increases the separator's ability to remove both entrained gas and excess solution gas, increasing the liquid residence time beyond a couple of minutes is often infeasible. The liquid residence times required to remove a majority of the excess solution gas soon approach levels associated with storage tanks, not gas-liquid separators.

8.5 Model Validation

8.5.1 Saturated Conditions

The current degassing model using saturated conditions can be compared to the degassing model originally designed by Slettebø, though Slettebø's model did not account for the entrained gas fraction (Slettebø, 2009). In the Slettebø model, the liquid cross-sectional area is divided horizontally and the bubble cutoff velocity required for separation at each liquid depth is determined. Since each bubble size has a corresponding bubble volume, the percent bubble volume remaining per section can be determined once the cutoff bubble size per section is found. Bubbles larger than the calculated cutoff size are assumed to be separated and removed from the section. The percent bubble volume remaining per section is then multiplied by the volume fraction of each segment. Summing the resulting values yields the total percent gas volume removed. This value can then be compared to the current model using a variable entrained gas fraction at different liquid residence times. Other than the entrained gas fraction, all input conditions are kept constant between the two models.

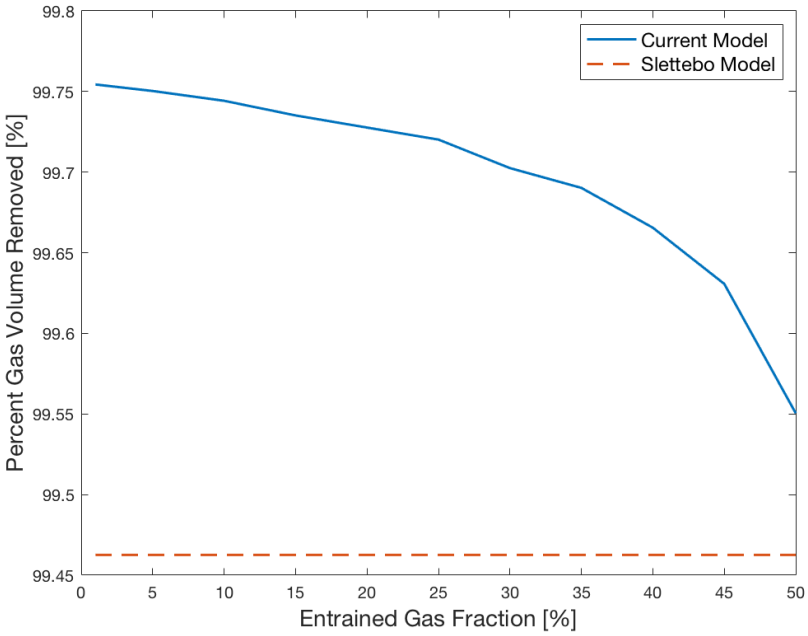

Figure 8.32: Comparison of the Slettebø model to the current model at $t_r = 60$ s

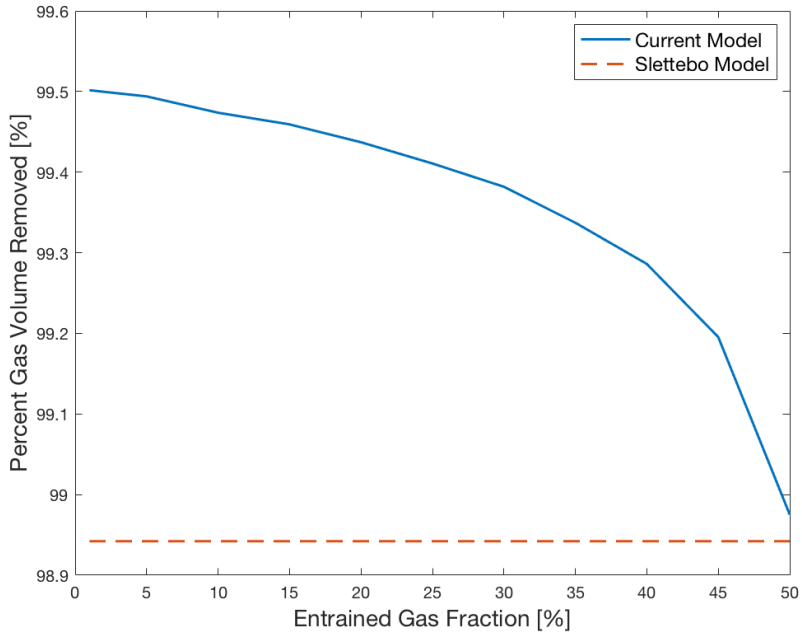

Figure 8.33: Comparison of the Slettebø model to the current model at $t_r = 45$ s

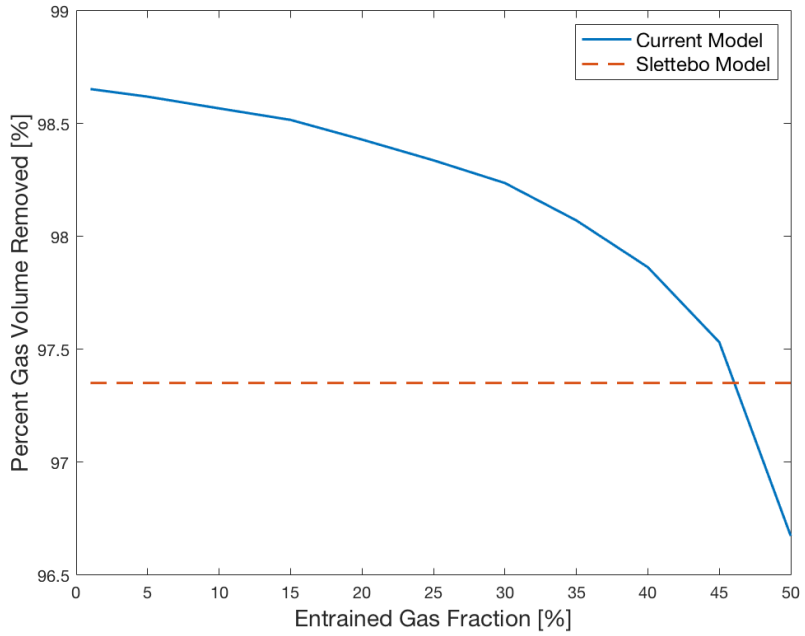

Figure 8.34: Comparison of the Slettebø model to the current model at $t_r = 30$ s

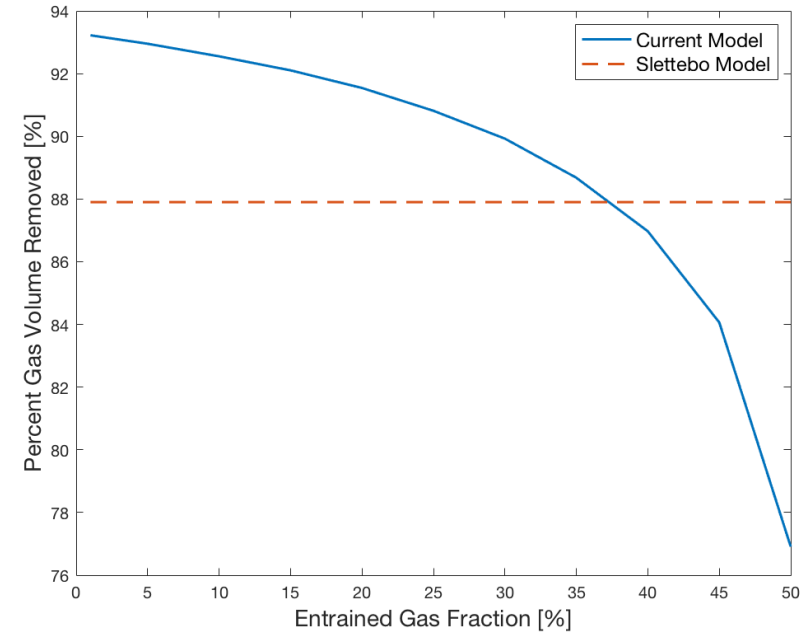

Figure 8.35: Comparison of the Slettebø model to the current model at $t_r = 15$ s

For the trial test conditions shown in Figures 8.32 – 8.35, the current model always bounded the the Slettebø model result. As the entrained gas fraction increases

in the current model, the total liquid height required for the bubbles to overcome also increases, leading to a decrease in the separator performance. Using an entrained gas fraction set to $x_{\text{eg}} = 0.01$, the current degassing model can also be compared to Slettebø's model. Other than the entrained gas fraction, all process conditions are otherwise the same while the liquid residence time is varied for both models. The results of this exercise are shown Figure 8.36.

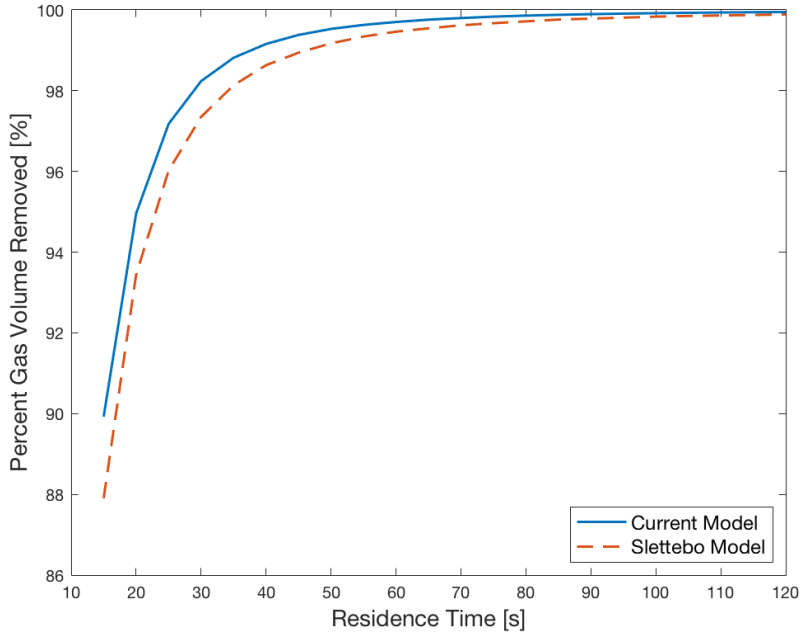

Figure 8.36: Comparison of the Slettebø model to the current model across of a range of liquid residence times

The current degassing model predicts higher rates of gas volume removal compared to the Slettebø model. The average error between the two models is 0.5 % for the above range, though at the lowest residence time the error between the two models in 2.1 %. As the liquid residence time is increased, both model results converge towards 100 % bubble volume removed. The discrepancy in the model results comes from how the non-linear bubble velocity calculation is solved in each model. Within the current model, the non-linear bubble velocity calculation is solved using the error reduction approach described in Section 8.1.4. In the Slettebø model, the

bubble velocity at each section is solved by initially starting with a small bubble diameter then incrementing the bubble diameter upward until the calculated bubble velocity slightly passes the bubble velocity required for separation in that section. At that point, the bubble velocity calculation is stopped and the final bubble diameter is used as the separation cutoff for that section of the liquid height. This bubble velocity calculation is graphically represented in Figure 8.37.

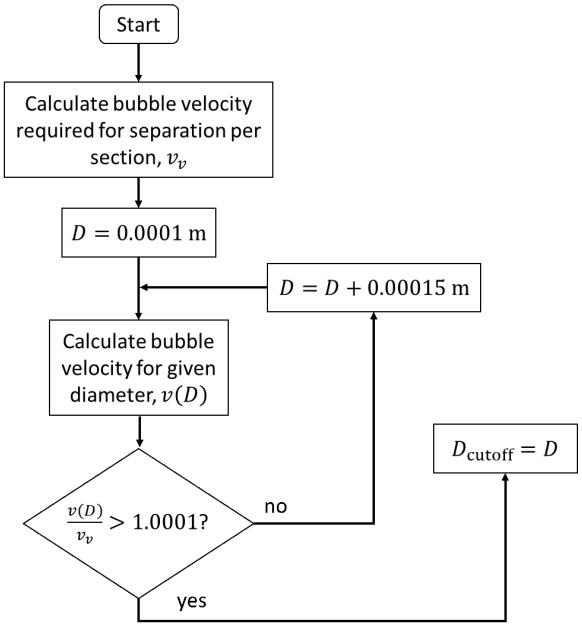

Figure 8.37: Algorithm used in Slettebø's model bubble velocity calculation

The bubble velocity calculation performed in Slettebø's model results in a consistent overestimation of the bubble diameter required for separation. A larger bubble diameter cutoff means that more bubbles are assumed to remain in the liquid, resulting in lower estimates of the total gas volume removed. The larger bubbles also account for a disproportionate amount of the entrained gas volume. At larger liquid residence times, only small bubbles remain in the liquid and the discrepancy between the two models is minimized. As the liquid residence time is decreased, larger bubbles remain in the liquid and the difference in the percent gas volume removed between the two models increasingly diverges.

8.5.2 Supersaturated Conditions

In order to ensure that the modeling framework is calculating the total rate of mass transfer correctly, the model input parameters can be modified to approximate conditions that are easy to check with simple calculations. As the entrained gas fraction approaches 0 and the liquid fill is maintained at 50%, the total interfacial area available for mass transfer approaches $A = 2r_{\text{ves}}L_{ves}$. The liquid volume is calculated simply from $V_{\text{l}} = 0.5\pi r_{\text{ves}}^2 L_{\text{ves}}$. The volumetric interfacial area then becomes a simple function of the vessel radius

$$a = \frac{4}{\pi r_{\text{ves}}} \tag{8.28}$$

Taking 50% solution gas removal as the target, the mass transfer coefficient can then be calculated from the liquid residence time and the vessel radius

$$k_{\text{l}} = \frac{-\pi r_{\text{ves}} \ln(0.5)}{4t_{\text{r}}} \tag{8.29}$$

Using a residence time of $t_{\text{r}} = 1000$ s and a vessel radius of $r_{\text{ves}} = 1/\pi$ m, the mass transfer coefficient can be calculated as $k_{\text{l}} = 1.7329 \cdot 10^{-4}$. By using a entrained gas fraction of $x_{\text{eg}} = 0.0001$, along with the aforementioned liquid residence time, vessel radius, and mass transfer coefficient, the degassing model correctly calculates percent solution gas removal of 50.00%. This validates the method of calculating the total interfacial area seen in Equation 8.16 and Equation 8.25, as well as the mass transfer calculation seen in Equation 8.24.

8.5.3 Cocurrent Bubble Flow Prediction

The separator model's ability to handle mass transfer can be compared to the experimental results presented by Lamont and Scott for their cocurrent bubbly flow experiment under the no-slip condition (equal gas and liquid velocities) (Lamont and

Scott, 1966). The mass transfer experiment performed by Lamont and Scott was absorption of CO_2 in water at 30 psig and 20 °C under turbulent flow conditions. While not an ideal point of reference, the experimental data can compared to the horizontal separator model using a few modifications. The section of pipe used in the experiment had a diameter of 5/16 in and 8 ft in length. The initial and equilibrium CO_2 concentrations used were 0.1134 mol/L and 123.5 mol/L, respectively. The bubbles generated in the experiment ranged from 3 to 6 mm, with a median bubble diameter of 4.5 mm. Since the flow in the experiment was fast enough keep the bubbles from separating, the vertical bubble velocity within the model was turned off. The liquid Reynolds number was varied using a fixed pipe geometry and the resulting mass transfer from the bubbles into the bulk liquid was measured. A comparison between the experimental data and the modified separator model can be seen in Figure 8.38.

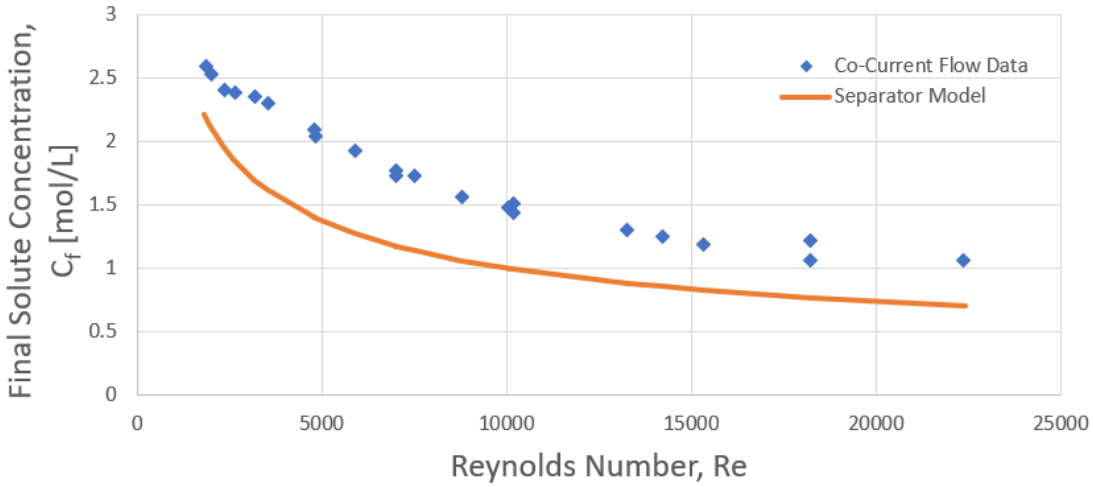

Figure 8.38: Final solute concentration vs liquid Reynolds number: Comparison between experimental data and separator model results

As the flow rate is increased, the mass transfer coefficient increases, but the total residence time decreases. The net result of the increased Reynolds number is a decrease in the final solute concentration in the liquid. This net decrease in the final concentration is reflected in both the data and the model. The separator model, though, consistently underpredicts the final solute concentration. This is likely due

to bubble breakup occurring during the turbulent liquid flow, increasing the total interfacial surface area and thus increasing the net mass transfer. The average error between the model and the data was 30.1 %. The separator model was not developed for turbulent flow conditions so the comparison with the experimental results should only be viewed as qualitative in nature.

8.5.4 Bubble Velocity Calculation

The method of calculating the bubble velocities can also be validated using both the Stokes bubble velocity calculation and the Davies and Taylor bubble velocity correlation (Davies and Taylor, 1950). The Stokes bubble velocity can be calculated using Equation 3.8. In the Stokes equation, the bubbles are assumed to be perfectly spherical. The Stokes equation provides a good approximation of the bubble velocities at small bubble diameters. The bubble velocity can be calculated according to the Davies and Taylor correlation using (Talaia, 2007)

$$v = 0.707\sqrt{gd} \tag{8.30}$$

The Davies and Taylor correlation was formulated for very large spherical cap bubbles, where the viscous and surface tension effects are negligible. The Davies and Taylor correlation represents the maximum allowable bubble velocity for a given bubble diameter. The method of calculating bubble velocities in the current model should yield results lower than the Davies and Taylor limit, while maintaining agreement with the Stokes bubble velocity calculation at small bubble sizes. The results of this comparison can be seen in Figure 8.39.

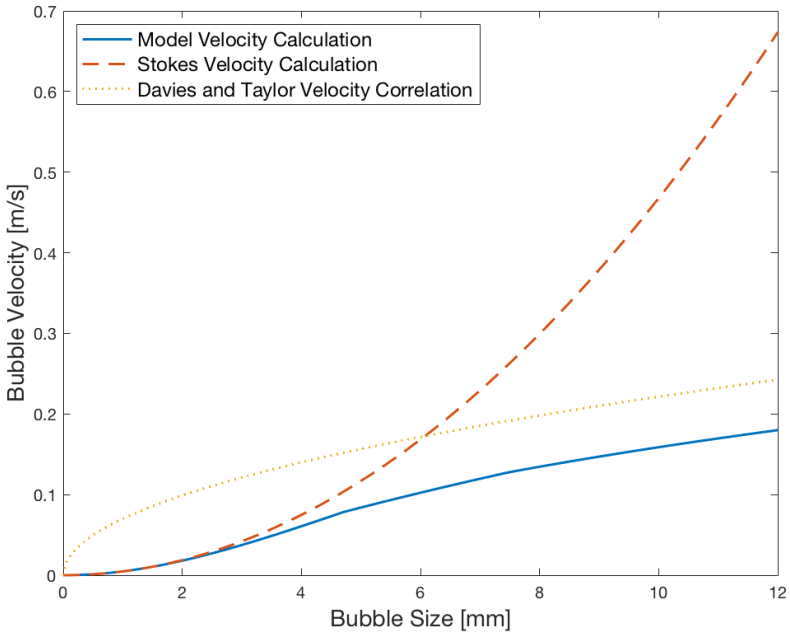

Figure 8.39: Comparison of the separator model bubble velocity calculation to the Stokes equation and Davies and Taylor velocity correlation

As seen in the above figure, the current method of calculating the bubble velocities is in agreement with the Stokes velocity equation up to bubble sizes of roughly 3 mm. After that point, the larger bubbles begin to deform, and the bubble drag coefficient is increasing affected by the bubble shape. The bubble velocity calculated within the model also never surpasses the maximum bubble velocity predicted by the Davies and Taylor correlation.

8.6 Conclusion

As shown in the above case studies, the liquid viscosity along with the size of the bubble distribution are key parameters in predicting degassing within this modeling framework. As the liquid phase viscosity increases, good bubble size management becomes increasingly important in reducing what would otherwise be unavoidably long separator residence times required for good separation. For non-supersaturated solutions, increasing the bubble diameter mode by even a few millimeters could make

the difference between adequate and poor separation. Inlet conditioning devices that increase the total size of the inlet bubble distribution have the potential to significantly improve separation performance. Inlet conditioning devices that serve primarily to increase the inlet bubble density closer to the bulk gas-liquid interface, on the other hand, are unlikely to improve separation performance by a significant amount. Other than the overall size of the bubble distribution, the sensitivity analysis results indicate that the liquid viscosity, not the liquid density, is the main driver for separation performance.

Traditional horizontal gas-liquid separators were found to be ill-suited for separating excess solution gas in supersaturated solutions. The driving force for mass transfer will increase the rate of entrained gas separation, however, removing the excess solution gas is more challenging. Liquid residence times of several hours are required to remove the majority of excess solution gas for the base case condition. To remove more than 50 % of the excess solution gas from a liquid with a supersaturation ratio of $\xi = 0.3$, the entrained gas fraction has to approach 50 % of the liquid volume and the bubble distribution mode must be less than 1.5 mm. The liquid swelling due to bubble growth during supersaturated conditions was, however, not found to be significant for a range of different supersaturation ratios. The result also highlight the need for bubbles in solution to provide additional interfacial area required for adequate excess solution gas separation. For conditions where the starting bubble sizes are large, the total volumetric interfacial area drops off quickly, ensuring the rate of gas-liquid mass transfer similarly decreases. If solution gas is present in an incoming gas-liquid stream, it could be advantageous to divert the stream to a gas-liquid contactor and removed as much of the solution gas as possible prior to entering a gas-liquid separator.

CHAPTER IX

CONCLUSION

The goal of this study was to explore gas evolution in the context of gas-liquid separation. An new experiment was developed to measure gas evolution in hydrocarbon systems at high pressure. The effect of mixing and liquid viscosity was explored using methane and air in model oils. Additionally, the rates of absorption and desorption (gas evolution) were measured and compared to one another using a reference methane-dodecane system. Once mass transfer was quantified for this reference system, the experimental results were used to construct a horizontal separator degassing model that calculates gas carry-under due to both entrained bubbles and excess solution gas.

9.1 Experimental

Developing a new experiment capable of measuring gas evolution at pressure was the primary objective of this study. The initial experimental design utilized a rapid depressurization step to generate excess solution gas within the liquid. This method was soon abandoned due to the inability of the experiment to generate an approximate step change in the pressure as the total experimental pressure was increased. The experiment was then modified in favor of a gradual depressurization technique. Using a dual-cylinder syringe pump, a saturated liquid was instead gradually depressurized, supersaturating the liquid in the process. From the supersaturated solution, gas evolution was initiated by turning on the pressure vessel mixer and measuring the resulting increase in pressure.

Using the developed gas-liquid mass transfer experiment, rates of gas evolution were measured in a reference methane-dodecane hydrocarbon system. The saturation pressure of the experiment was varied from 500 to 1,500 psia (3.45 to 10.3 MPa), while the mixing speed was varied from 100 to 250 rpm. The maximum mixing speed was limited to values that maintained a flat gas-liquid interfacial area, allowing the area available for mass transfer to be quantified for all trial conditions.

In order to ensure that the measured gas evolution rates were not significantly effected by bubble nucleation, both the rates of absorption and desorption were measured for each trial condition. Within the measurement error, the absorption and desorption mass transfer coefficients were found to be symmetric. The symmetry between the two mass transfer coefficients confirms that bubble nucleation was not significantly affecting the measured gas evolution rates. All measured absorption and desorption mass transfer coefficients were within 17% of one another for the same trial conditions. The mixing speed was found to be the most significant variable affecting the rate of mass transfer while the saturation pressure within the range tested here had minimal effect.

In an attempt to generalize the mass transfer results beyond the stirred tank experimental setup, theoretically derived mass transfer expressions were evaluated for their ability to quantify the data. The surface renewal theory in the form of the small eddy model was found to be a good fit to the experimentally measured data. The solid and fluid surface eddy cell models were applied to the experimental conditions and resulted in a reasonable fit for both cases. The solid surface model was found to better fit the experimental results, yielding an averaged absolute error of 12.3%.

9.2 Modeling

A degassing model was constructed for horizontal gas-liquid separators, expanding on the work originally presented by Slettebø (Slettebø, 2009). The developed

degassing model allows both the gas and liquid phases to be conserved. Using the solid surface mass transfer model validated for the reference hydrocarbon system at pressure, the degassing model was able to calculate gas carry-under due to entrained gas bubbles as well as excess solution gas in the liquid.

A horizontal separator's ability to remove entrained gas was found to be driven primarily by the liquid viscosity as well as the overall size of the initial bubble distribution. The liquid density, as well as the bubble density, within the liquid surface area were found to have little effect on the rate of entrained gas removal. From these results, new guidelines were developed in Table 8.4 based on the liquid residence times required to reach 1% gas volume remaining for a given bubble distribution mode and liquid viscosity. For gas-liquid separation involving supersaturated solutions, the results highlight the need for large numbers of small bubbles required for adequate excess solution separation. These conditions are, however, in direct opposition to the conditions desired for good entrained gas separation. If an inlet stream contains a large amount of excess solution gas, it may be desirable to divert the stream to a gas-liquid contactor to remove the excess solution gas prior to sending the stream into a traditional gas-liquid separator.

CHAPTER X

RECOMMENDATIONS

10.1 Mass Transfer Experiment

The focus of the experimental work presented here was largely centered around validating the developed mass transfer experiment using a simple hydrocarbon systems. Gas evolution should be further studied using gases and liquids that more closely approach real production systems. The saturation pressures investigated here did not have a strong effect on the rate of mass transfer. As the total pressure increases, the solute concentration within the solvent would begin to increase to the point were the physical properties of the system are significantly effected. Future gas evolution experiments should be conducted at higher saturation pressures to investigate if this trends continues to hold true.

The small eddy mass transfer model should also be tested against different combinations of gases and liquids. The model validation, however, requires knowledge of the solute diffusivity, liquid density, and liquid viscosity at the experimental pressure and solute concentration. The advantage of using a simple reference system is the availability of physical properties in the open literature. As different gas-liquid systems are tested, experimental capabilities should also be upgraded to measure the required physical properties at the conditions of interest. Once this mass transfer model is more thoroughly validated with well quantified systems, different crude oils can be explored where correlations are used to estimate the required physical properties.

For the horizontal separator modeling, it is assumed that the rate of mass

transfer holds equally for the bulk gas-liquid interface as well as mass transfer occurring at the bubble interface within the liquid. Future studies should attempt to confirm whether the small eddy model holds true equally at the bulk and bubble interface. One of the drawbacks of the small eddy model framework is that interfacial forces are not considered. The presence of surface active components such as asphaltenes could impact the rate of gas-liquid mass transfer. The effect of surfactants on gas evolution should also be studied going forward.

10.2 Separator Modeling

While degassing is usually only a concern in horizontal gas-liquid separators, the degassing framework presented here could also be applied to vertical gas-liquid separators. The model would have to account for the changing liquid height as entrained gas flows in the same axis as the liquid flow. By tracking bubbles over time, their growth and velocities relative to the liquid flow could be calculated. Using this information, the rate of gas carry-under due to both entrained gas and excess solution gas could be calculated in a similar manner. The vertical separator model could also be used to model degassing in liquid boots attached to cyclone separators.

The horizontal separator model presented here is simplistic from a geometric perspective. Modern horizontal separators will usually have an inlet conditioning device as well as internals that improve the stratification of the phases being separated. How these additional separator internals change the ability of a separator to degas liquids is still unexplored in the open literature, though it is unlikely they would deteriorate the separation performance. As such, the modeling framework presented here could serve as a worst-case analysis should the separator internals not perform at all.

This work demonstrates that removing significant amounts of excess solution gas from the liquid was challenging once it entered the horizontal separator. There is

the potential to avoid this challenge in the first place if the inlet multiphase stream is properly treated to ensure that the majority of the excess solution gas is removed prior to entering the separator. Multiphase flow conditions that promote gas evolution within a pipe should be investigated as an alternative method of dealing with excess solution gas. Finally, the effects of gas evolution during gas-liquid-liquid separation should be considered. There is the potential for gas coming out of solution to promote increased coalescence between a water-in-oil or oil-in-water emulsion. Bubble nucleation on the separator wall could also be accounted for in future versions of the degassing model.

REFERENCES

Abou-El-Hassan, M. (1983), 'A generalized bubble rise velocity correlation', *Chemical Engineering Communications* **22**(3-4), 243–250.

Ammar, M., Driss, Z., Chtourou, W. and Abid, M. (2011), 'Effects of baffle length on turbulent flows generated in stirred vessels', *Open Engineering* **1**(4), 401–412.

Angelino, H. (1966), 'Hydrodynamique des grosses bulles dans les liquides visqueux', *Chemical Engineering Science* **21**(6-7), 541–550.

API (2009), *Specification for Oil and Gas Separators*, API Specification 12J, 8th edn.

Arefmanesh, A., Advani, S. G. and Michaelides, E. E. (1992), 'An accurate numerical solution for mass diffusion-induced bubble growth in viscous liquids containing limited dissolved gas', *International Journal of Heat and Mass Transfer* **35**(7), 1711–1722.

Arnold, K. and Stewart, M. (1998), *Surface Production Operations-Design of Oil Handling Systems and Facilities, Volume 1*, Gulf Publishing Company.

Astarita, G. and Apuzzo, G. (1965), 'Motion of gas bubbles in non-newtonian liquids', *AIChE Journal* **11**(5), 815–820.

ASTM (2017), *D341-17 Standard Practice for Viscosity-Temperature Charts for Liquid Petroleum Products*, American Society for Testing and Materials, International.

Austrheim, T. (2006), 'Experimental characterization of high-pressure natural gas scrubbers'.

Bahadori, A. (2014), *Natural Gas Processing: Technology and Engineering Design*, Gulf Professional Publishing.

Baker, A., Lucas-Clements, D. et al. (1990), Application of subsea separation and pumping to marginal and deepwater field developments, *in* 'SPE Annual Technical Conference and Exhibition', Society of Petroleum Engineers.

Barker, G., Jefferson, B. and Judd, S. (2002), 'The control of bubble size in carbonated beverages', *Chemical Engineering Science* **57**(4), 565–573.

Barlow, E. J. and Langlois, W. E. (1962), 'Diffusion of gas from a liquid into an expanding bubble', *IBM Journal of Research and Development* **6**(3), 329–337.

Barnett, S. M., Humphrey, A. E. and Litt, M. (1966), 'Bubble motion and mass transfer in non-newtonian fluids', *AIChE Journal* **12**(2), 253–259.

Bauget, F., Lenormand, R. et al. (2002), Mechanisms of bubble formation by pressure decline in porous media: a critical review, *in* 'SPE Annual Technical Conference and Exhibition', Society of Petroleum Engineers.

Becker, R. and Döring, W. (1935), 'Kinetische behandlung der keimbildung in übersättigten dämpfen', *Annalen der Physik* **416**(8), 719–752.

Biń, A. K. (1984), 'Mass transfer to the free interface in stirred vessels', *Chemical engineering communications* **31**(1-6), 155–183.

Biń, A. K. (1993), 'Gas entrainment by plunging liquid jets', *Chemical Engineering Science* **48**(21), 3585–3630.

Bird, R. B., Stewart, W. E. and Lightfoot, E. N. (2004), 'Transport phenomena. 2002', *JohnWiley & Sons, New York* .

Bisperink, C. G. and Prins, A. (1994), 'Bubble growth in carbonated liquids', *Colloids and Surfaces A: Physicochemical and Engineering Aspects* **85**(2-3), 237–253.

Bothamley, M. (2013*a*), 'Gas/liquid separators: Quantifying separation performance-part 1', *Oil and Gas Facilities* **2**(04), 21–29.

Bothamley, M. (2013*b*), 'Gas/liquids separators: Quantifying separation performance-part 2', *Oil and Gas Facilities* **2**(05), 35–47.

Bothamley, M. (2013*c*), 'Gas/liquids separators: Quantifying separation performance-part 3', *Oil and Gas Facilities* **2**(06), 34–47.

Brennen, C. E. (2013), *Cavitation and bubble dynamics*, Cambridge University Press.

Buehl, W. and Westwater, J. (1966), 'Bubble growth by dissolution: influence of contact angle', *AIChE Journal* **12**(3), 571–576.

Buffo, A., Vanni, M. and Marchisio, D. (2012), 'Multidimensional population balance model for the simulation of turbulent gas–liquid systems in stirred tank reactors', *Chemical Engineering Science* **70**, 31–44.

Bymaster, A., Olson, M., Grave, E., Svedeman, S. J., Viana, F., Akdim, M. R., Mikkelsen, R. et al. (2011), High pressure gas-liquid separation: An experimental study on separator performance of natural gas streams at elevated pressures, *in* 'Offshore Technology Conference', Offshore Technology Conference.

Carey, V. P. (1992), *Liquid–Vapor Phase-Change Phenomena: An Introduction to the Thermodynamics of Vaporization and Condensation Processes in Heat Transfer Equipments*, Hemisphere Publishing Corporation, USA.

Chen, C.-C., Hung, L.-C. and Hsu, H.-K. (1993), 'Heterogeneous nucleation of water vapor on particles of sio2, al2o3, tio2, and carbon black', *Journal of colloid and interface science* **157**(2), 465–477.

Chirinos, W., Gomez, L., Wang, S., Mohan, R., Shoham, O. and Kouba, G. (n.d.), Liquid carry-over in gas-liquid cylindrical cyclone compact separators, *in* 'SPE Annual Technical Conference and Exhibition', Society of Petroleum Engineers.

Clark, H., Strenge, P. and Westwater, J. (1959), 'Active sites for nucleate boiling', *Chem. Eng. Progr.* **55**.

Clark, N. N., Liu, W. and Turton, R. (1996), 'Data interpretation techniques for inferring bubble size distribution from probe signals in fluidized systems', *Powder technology* **88**(2), 179–188.

Clift, R., Grace, J. R. and Weber, M. E. (2005), *Bubbles, drops, and particles*, Courier Corporation.

Cole, R. (1974), Boiling nucleation, *in* 'Advances in heat transfer', Vol. 10, Elsevier, pp. 85–166.

Crum, L. A. (1982), 'Nucleation and stabilization of microbubbles in liquids', *Applied Scientific Research* **38**(1), 101–115.

Danckwerts, P. (1951), 'Significance of liquid-film coefficients in gas absorption', *Industrial & Engineering Chemistry* **43**(6), 1460–1467.

Daniel, A. B., Mohammad, S., Whiteley, J. R., Kouba, G. E., Lavenson, D. M., Kelkar, A., Subramani, H. J., Aichele, C. P. et al. (2015), Gas evolution rates in crude oil for subsea separator applications, *in* 'SPE Annual Technical Conference and Exhibition', Society of Petroleum Engineers.

Davies, R. and Taylor, G. I. (1950), 'The mechanics of large bubbles rising through extended liquids and through liquids in tubes', *Proc. R. Soc. Lond. A* **200**(1062), 375–390.

de Lamotte, A., Delafosse, A., Calvo, S., Delvigne, F. and Toye, D. (2017), 'Investigating the effects of hydrodynamics and mixing on mass transfer through the free-surface in stirred tank bioreactors', *Chemical Engineering Science* **172**, 125–142.

Di Silvestro, R., Abrand, S., Shaiek, S., Butin, N., Riou, X., Kathleen, D. M. et al. (2011), A novel gas/liquid separator to enhance production of deepwater marginal, *in* 'Offshore Technology Conference', Offshore Technology Conference.

Divinis, N., Karapantsios, T. D., De Bruijn, R., Kostoglou, M., Bontozoglou, V. and Legros, J.-C. (2006), 'Bubble dynamics during degassing of liquids at microgravity conditions', *AIChE journal* **52**(9), 3029–3040.

Dominguez, A. (1997), Formation dune Phase Gazeuse par Decompression dune Solution Binaire (Liquid-Gaz) en milieu Poreux, Phd thesis.

Ducci, A. and Yianneskis, M. (2005), 'Direct determination of energy dissipation in stirred vessels with two-point lda', *AIChE journal* **51**(8), 2133–2149.

El-Yousfi, A. (1992), Contribution l'tude des mcanismes de formation d'une phase gazeuse par dtente d'une solution binaire (liquide-gaz) en milieu poreux, Phd thesis.

El Yousfi, A., Zarcone, C., Bories, S., Lenormand, R. et al. (1997), Physical mechanisms for bubble growth during solution gas drive, *in* 'SPE Annual Technical Conference and Exhibition', Society of Petroleum Engineers.

Enríquez, O. R., Hummelink, C., Bruggert, G.-W., Lohse, D., Prosperetti, A., van der Meer, D. and Sun, C. (2013), 'Growing bubbles in a slightly supersaturated liquid solution', *Review of scientific instruments* **84**(6), 065111.

Enríquez, O. R., Sun, C., Lohse, D., Prosperetti, A. and van der Meer, D. (2014), 'The quasi-static growth of co 2 bubbles', *Journal of fluid mechanics* **741**.

Erdal, F. M., Shirazi, S. A., Shoham, O., Kouba, G. E. et al. (1997), 'Cfd simulation of single-phase and two-phase flow in gas-liquid cylindrical cyclone separators', *SPE Journal* **2**(04), 436–446.

Fantoft, R., Hendriks, T., Chin, R. et al. (2004), Compact subsea separation system with integrated sand handling, *in* 'Offshore Technology Conference', Offshore Technology Conference.

Farkas, L. (1927), 'The velocity of nucleus formation in supersaturated vapors', *J. Physik Chem* **125**, 236.

Fernández, Y. B., Cartmell, E., Soares, A., McAdam, E., Vale, P., Darche-Dugaret, C. and Jefferson, B. (2015), 'Gas to liquid mass transfer in rheologically complex fluids', *Chemical Engineering Journal* **273**, 656–667.

Forster, H. K. and Zuber, N. (1954), 'Growth of a vapor bubble in a superheated liquid', *Journal of Applied Physics* **25**(4), 474–478.

Fortescue, G. and Pearson, J. (1967), 'On gas absorption into a turbulent liquid', *Chemical Engineering Science* **22**(9), 1163–1176.

Frenkel, J. (1946), 'Kinetic theory of liquids' clarendon press'.

Garcia-Ochoa, F. and Gomez, E. (2009), 'Bioreactor scale-up and oxygen transfer rate in microbial processes: an overview', *Biotechnology advances* **27**(2), 153–176.

Gardenier, G. H., Gui, F. and Demas, J. N. (2011), 'Error propagation made easy or at least easier', *Journal of Chemical Education* **88**(7), 916–920.

Ghiaasiaan, S. M. (2007), *Two-phase flow, boiling, and condensation: in conventional and miniature systems*, Cambridge University Press.

Gilliland, E. R. and Sherwood, T. K. (1934), 'Diffusion of vapors into air streams', *Industrial & Engineering Chemistry* **26**(5), 516–523.

Glas, J. and Westwater, J. (1964), 'Measurements of the growth of electrolytic bubbles', *International Journal of Heat and Mass Transfer* **7**(12), 1427–1443.

Gomez, L. E., Mohan, R. S., Shoham, O., Marrelli, J. D., Kouba, G. E. et al. (1999), State-of-the-art simulator for field applications of gas-liquid cylindrical cyclone separators, *in* 'SPE Annual Technical Conference and Exhibition', Society of Petroleum Engineers.

GPSA (2004), *Engineering Data Book, SI Version*, 12th edn, Gas Processors Suppliers Association, Tulsa, OK.

GPSA (2016), *Engineering Data Book, SI Version*, 14th edn, Gas Processors Suppliers Association, Tulsa, OK.

Grace, J. (1973), 'Shapes and velocities of bubbles rising in infinite liquid', *Transactions of the Institution of Chemical Engineers* **51**, 116–120.

Haberman, W. L. (1954), An experimental study of bubbles moving in liquids., *in* 'Proceedings American Society of Civil Engineers', Vol. 80, pp. 1–25.

Hamborg, E. S., Kersten, S. R. A. and Versteeg, G. F. (2010), 'Absorption and desorption mass transfer rates in non-reactive systems', *Chemical Engineering Journal* **161**(12), 191–195.

Haque, M., Nigam, K., Viswanathan, K. and Joshi, J. (1988), 'Studies on bubble rise velocity in bubble columns employing non-newtonian solutions', *Chemical Engineering Communications* **73**(1), 31–42.

Harmathy, T. Z. (1960), 'Velocity of large drops and bubbles in media of infinite or restricted extent', *AIChE Journal* **6**(2), 281–288.

Harvey, E. N. (1945), 'Decompression sickness and bubble formation in blood and tissues', *Bulletin of the New York Academy of Medicine* **21**(10), 505.

Harvey, E. N., McElroy, W. D. and Whiteley, A. (1947), 'On cavity formation in water', *Journal of Applied Physics* **18**(2), 162–172.

Hemmingsen, E. A. (1975), 'Cavitation in gas- supersaturated solutions', *Journal of Applied Physics* **46**(1), 213–218.

Higbie, R. (1935), 'The rate of absorption of a pure gas into a still liquid during short periods of exposure', *Trans. AIChE* **31**, 365–389.

Hirasaki, G., O'Meara Jr, D., Rohan, J. et al. (1988), Centrifuge measurements of capillary pressure: Part 2-cavitation, *in* 'SPE Annual Technical Conference and Exhibition', Society of Petroleum Engineers.

Holland, D., Blake, A., Tayler, A., Sederman, A. and Gladden, L. (2011), 'A bayesian approach to characterising multi-phase flows using magnetic resonance: Application to bubble flows', *Journal of Magnetic Resonance* **209**(1), 83–87.

Holtappels, K., Schröder, V., Pekalski, A. and Schildberg, H. (2011), Limiting oxygen concentrations-process safety by oxygen monitoring, *in* 'ICDERS'.

Horn, T., Bakke, W., Eriksen, G. et al. (2003), Experience in operating world's first subsea separation and water injection station at troll oil field in the north sea, *in* 'Offshore Technology Conference', Offshore Technology Conference.

Hunt, L. M. (1995), Gas Dissolution Phenomena in Crude Oil Production, Thesis.

Jamialahmadi, M., Emadi, M. and Müller-Steinhagen, H. (2006), 'Diffusion coefficients of methane in liquid hydrocarbons at high pressure and temperature', *Journal of Petroleum Science and Engineering* **53**(1-2), 47–60.

Jones, S., Evans, G. and Galvin, K. (1999), 'Bubble nucleation from gas cavitiesa review', *Advances in colloid and interface science* **80**(1), 27–50.

Karamanev, D. (1996), 'Equations for calculation of the terminal velocity and drag coefficient of solid spheres and gas bubbles', *Chemical engineering communications* **147**(1), 75–84.

Karamanev, D. G. (1994), 'Rise of gas bubbles in quiescent liquids', *AIChE journal* **40**(8), 1418–1421.

Kawase, Y., Halard, B. and Moo-Young, M. (1987), 'Theoretical prediction of volumetric mass transfer coefficients in bubble columns for newtonian and non-newtonian fluids', *chemical Engineering science* **42**(7), 1609–1617.

Kawase, Y. and Moo-Young, M. (1987), 'Solidturbulent fluid heat and mass transfer: a unified model based on the energy dissipation rate concept', *The Chemical Engineering Journal* **36**(1), 31–40.

Kostoglou, M. and Karapantsios, T. (2005), 'Approximate solution for a nonisothermal gas bubble growth over a spherical heating element', *Industrial & engineering chemistry research* **44**(21), 8127–8135.

Kouba, G. and Shoham, O. (1996), A review of gas-liquid cylindrical cyclone (glcc) technology, *in* 'Production Separation Systems International Conference, Aberdeen, England, April', pp. 23–24.

Kristiansen, O., Sørensen, Ø., Nilssen, O. et al. (2016), Compactsep-compact subsea gas-liquid separator for high-pressure wellstream boosting, *in* 'Offshore Technology Conference', Offshore Technology Conference.

Kulkarni, A. A. and Joshi, J. B. (2005), 'Bubble formation and bubble rise velocity in gas- liquid systems: a review', *Industrial & Engineering Chemistry Research* **44**(16), 5873–5931.

Lake, L. W. and Arnold, K. E. (2007), *Petroleum Engineering Handbook: Facilities and Construction Engineering*, Vol. 3, Society of Petroleum Engineers.

Lamont, J. C. and Scott, D. (1970), 'An eddy cell model of mass transfer into the surface of a turbulent liquid', *AIChE Journal* **16**(4), 513–519.

Lamont, J. and Scott, D. (1966), 'Mass transfer from bubbles in cocurrent flow', *The Canadian Journal of Chemical Engineering* **44**(4), 201–208.

Lau, Y., Deen, N. and Kuipers, J. (2013), 'Development of an image measurement technique for size distribution in dense bubbly flows', *Chemical Engineering Science* **94**, 20–29.

Lavenson, D. M., Kelkar, A. V., Daniel, A. B., Mohammad, S. A., Kouba, G. and Aichele, C. P. (2016), 'Gas evolution rates–a critical uncertainty in challenged gas-liquid separations', *Journal of Petroleum Science and Engineering* **147**, 816–828.

Lavenson, D. M., Kelkar, A. V., Joshi, N., Portman, L. et al. (2017), Kinetics of fluid phase behavior changes: A critical uncertainty for offshore field development, *in* 'Offshore Technology Conference', Offshore Technology Conference.

Lemmon, E. W., Jacobsen, R. T., Penoncello, S. G. and Friend, D. G. (2000), 'Thermodynamic properties of air and mixtures of nitrogen, argon, and oxygen from 60 to 2000 k at pressures to 2000 mpa', *Journal of physical and chemical reference data* **29**(3), 331–385.

Lewis, W. and Whitman, W. (1924), 'Principles of gas absorption.', *Industrial & Engineering Chemistry* **16**(12), 1215–1220.

Liao, Y. and Lucas, D. (2010), 'A literature review on mechanisms and models for the coalescence process of fluid particles', *Chemical Engineering Science* **65**(10), 2851–2864.

Liger-Belair, G., Vignes-Adler, M., Voisin, C., Robillard, B. and Jeandet, P. (2002), 'Kinetics of gas discharging in a glass of champagne: the role of nucleation sites', *Langmuir* **18**(4), 1294–1301.

Liger-Belair, G., Voisin, C. and Jeandet, P. (2005), 'Modeling nonclassical heterogeneous bubble nucleation from cellulose fibers: application to bubbling in carbonated beverages', *The Journal of Physical Chemistry B* **109**(30), 14573–14580.

Lim, K. and Agarwal, P. K. (1990), 'Conversion of pierced lengths measured at a probe to bubble size measures: an assessment of the geometrical probability approach and bubble shape models', *Powder technology* **63**(3), 205–219.

Linek, V., Kordač, M., Fujasova, M. and Moucha, T. (2004), 'Gas–liquid mass transfer coefficient in stirred tanks interpreted through models of idealized eddy structure of turbulence in the bubble vicinity', *Chemical Engineering and Processing: Process Intensification* **43**(12), 1511–1517.

Linek, V., Kordač, M. and Moucha, T. (2005), 'Mechanism of mass transfer from bubbles in dispersions: part ii mass transfer coefficients in stirred gas–liquid reactor and bubble column', *Chemical Engineering and Processing: Process Intensification* **44**(1), 121–130.

Liu, W. and Clark, N. (1995), 'Relationships between distributions of chord lengths and distributions of bubble sizes including their statistical parameters', *International Journal of Multiphase Flow* **21**(6), 1073–1089.

Liu, W., Clark, N. N. and Karamavruc, A. I. (1996), 'General method for the transformation of chord-length data to a local bubble-size distribution', *AIChE journal* **42**(10), 2713–2720.

Lockemann, C. and Schilünder, E.-U. (1995), 'Liquid-phase mass transfer in high-pressure systems with a supercritical and a liquid phase', *International journal of thermophysics* **16**(3), 611–618.

Lubetkin, S. (1995), 'The fundamentals of bubble evolution', *Chemical Society Reviews* **24**(4), 243–250.

Lubetkin, S. and Blackwell, M. (1988), 'The nucleation of bubbles in supersaturated solutions', *Journal of colloid and interface science* **126**(2), 610–615.

Lyons, W. (2009), *Working Guide to Petroleum and Natural Gas Production Engineering*, Gulf Professional Publishing.

Ma, Z. (2014), Impeller Power Draw Across the Full Reynolds Number Spectrum, PhD thesis, University of Dayton.

Mantilla, I. (2008), Mechanistic Modeling of Liquid Entrainment in Gas in Horizontal Pipes, Thesis.

Margaritis, A., te Bokkel, D. W. and Karamanev, D. G. (1999), 'Bubble rise velocities and drag coefficients in non-newtonian polysaccharide solutions', *Biotechnology and bioengineering* **64**(3), 257–266.

Martín, M., Montes, F. J. and Galán, M. A. (2009), 'Theoretical modelling of the effect of surface active species on the mass transfer rates in bubble column reactors', *Chemical engineering journal* **155**(1-2), 272–284.

McCabe, W. L., Smith, J. C. and Harriott, P. (1993), *Unit operations of chemical engineering*, Vol. 5, McGraw-Hill New York.

McClimans, O., Fantoft, R. et al. (2006), Status and new developments in subsea processing, *in* 'Offshore Technology Conference', Offshore Technology Conference.

Mendelson, H. D. (1967), 'The prediction of bubble terminal velocities from wave theory', *AIChE Journal* **13**(2), 250–253.

Paras, S. and Karabelas, A. (1991), 'Droplet entrainment and deposition in horizontal annular flow', *International Journal of Multiphase Flow* **17**(4), 455–468.

Patel, R. D. (1980), 'Bubble growth in a viscous newtonian liquid', *Chemical Engineering Science* **35**(11), 2352–2356.

Payvar, P. (1987), 'Mass transfer-controlled bubble growth during rapid decompression of a liquid', *International journal of heat and mass transfer* **30**(4), 699–706.

Peebles, F. N. (1953), 'Studies on the motion of gas bubbles in liquid', *Chem. Eng. Prog.* **49**(2), 88–97.

Plesset, M. S. and Zwick, S. A. (1954), 'The growth of vapor bubbles in superheated liquids', *Journal of applied physics* **25**(4), 493–500.

Putnam, A. (1961), 'Integratable form of droplet drag coefficient'.

Riazi, M. (2005), *Characterization and properties of petroleum fractions*, Vol. 50, ASTM international.

Rosa, E., França, F. and Ribeiro, G. (2001), 'The cyclone gas-liquid separator: Operation and mechanistic modeling', *Journal of Petroleum Science and Engineering* **32**(2-4), 87–101.

Rosner, D. E. and Epstein, M. (1972), 'Effects of interface kinetics, capillarity and solute diffusion on bubble growth rates in highly supersaturated liquids', *Chemical Engineering Science* **27**(1), 69–88.

Ruckenstein, E. (1964), 'On mass transfer in the continuous phase from spherical bubbles or drops', *Chemical Engineering Science* **19**(2), 131–146.

Rüdisüli, M., Schildhauer, T. J., Biollaz, S. M. and van Ommen, J. R. (2012), 'Monte carlo simulation of the bubble size distribution in a fluidized bed with intrusive probes', *International Journal of Multiphase Flow* **44**, 1–14.

Sambath, K. (2013), Dynamics of drop disintegration and coalescence with and without electric fields, PhD thesis, Purdue University.

Scargiali, F., Busciglio, A., Grisafi, F. and Brucato, A. (2013), 'Influence of viscosity on mass transfer performance of unbaffled stirred vessels', *Chem Eng* **32**, 1483–1488.

Schweitzer, P. H. and Szebehely, V. G. (1950), 'Gas evolution in liquids and cavitation', *Journal of Applied Physics* **21**(12), 1218–1224.

Scriven, L. (1959), 'On the dynamics of phase growth', *Chemical engineering science* **10**(1-2), 1–13.

Seader, J. D., Henley, E. J. and Roper, D. K. (1998), 'Separation process principles'.

Setzmann, U. and Wagner, W. (1991), 'A new equation of state and tables of thermodynamic properties for methane covering the range from the melting line to 625 k at pressures up to 100 mpa', *Journal of Physical and Chemical reference data* **20**(6), 1061–1155.

Shafer, N. E. and Zare, R. N. (1991), 'Through a beer glass darkly', *Physics Today* **44**(10), 48–52.

Sherwood, T. K., Pigford, R. L. and Wilke, C. R. (1975), *Mass transfer*, McGraw-Hill.

Sides, P. J. (1986), Phenomena and effects of electrolytic gas evolution, *in* 'Modern aspects of electrochemistry', Springer, pp. 303–354.

Slettebø, E. S. (2009), Separation of gas from liquids in viscous systems, M.a.sc. thesis.

Smit, A. (2007), Air entrainment with plunging jets: experimental study about air entrainment with free overfall jets from circular channels and air bubble intake with submersible pumps in sewer sumps, Thesis.

Sobieszuk, P., Ilnicki, F. and Pohorecki, R. (2014), 'Contribution of liquid-and gas-side mass transfer coefficients to overall mass transfer coefficient in taylor flow in a microreactor', *Chemical and Process Engineering* **35**(1), 35–45.

Song, D., Seibert, A. F. and Rochelle, G. T. (2014), 'Effect of liquid viscosity on the liquid phase mass transfer coefficient of packing', *Energy Procedia* **63**, 1268–1286.

Srivastan, S., Darwish, N. A., Gasem, K. A. and Robinson Jr, R. L. (1992), 'Solubility of methane in hexane, decane, and dodecane at temperatures from 311 to 423 k and pressures to 10.4 mpa', *Journal of Chemical and Engineering Data* **37**(4), 516–520.

Stegeman, D., Knop, P., Wijnands, A. and Westerterp, K. (1996), 'Interfacial area and gas holdup in a bubble column reactor at elevated pressures', *Industrial & engineering chemistry research* **35**(11), 3842–3847.

Stewart, M. and Arnold, K. (2008), *Gas-liquid and Liquid-liquid Separators*, Gulf Professional Publishing.

Stokes, G. G. (1851), *On the effect of the internal friction of fluids on the motion of pendulums*, Vol. 9, Pitt Press Cambridge.

Strasberg, M. (1959), 'Onset of ultrasonic cavitation in tap water', *The Journal of the Acoustical Society of America* **31**(2), 163–176.

Street, J. R., Fricke, A. L. and Reiss, L. P. (1971), 'Dynamics of phase growth in viscous, non-newtonian liquids. initial stages of growth', *Industrial & Engineering Chemistry Fundamentals* **10**(1), 54–64.

Szekely, J. and Martins, G. (1971), 'Non-equilibrium effects in the growth of spherical gas bubbles due to solute diffusion', *Chemical Engineering Science* **26**(1), 147–159.

Tadaki, T. (1961), 'On the shape and velocity of single air bubbles rising in various liquids', *Kagaku Kogaku* **25**, 254–264.

Talaia, M. A. (2007), 'Terminal velocity of a bubble rise in a liquid column', *World Academy of Science, Engineering and Technology* **28**, 264–268.

Valiorgue, P. (2012), Mass transfer in intermittent horizontal gas-liquid flow and application to photobioreactors, PhD thesis, Lyon 1.

Versteeg, G., Blauwhoff, P. and van Swaaij, W. P. M. (1987), 'The effect of diffusivity on gas-liquid mass transfer in stirred vessels. experiments at atmospheric and elevated pressures', *Chemical Engineering Science* **42**(5), 1103–1119.

Viles, J. (1993), 'Predicting liquid re-entrainment in horizontal separators', *Journal of Petroleum Technology* **45**(05), 405–409.

Vinogradova, O., Bunkin, N., Churaev, N., Kiseleva, O., Lobeyev, A. and Ninham, B. (1995), 'Submicrocavity structure of water between hydrophobic and hydrophilic walls as revealed by optical cavitation', *Journal of colloid and interface science* **173**(2), 443–447.

Volmer, M. (1926), 'Nucleus formation in supersaturated systems', *Z. phys. Chem.* **119**, 277–301.

Wang, C. and Dhir, V. (1993), 'Effect of surface wettability on active nucleation site density during pool boiling of water on a vertical surface', *Journal of Heat Transfer* **115**(3), 659–669.

Wang, T. and Wang, J. (2007), 'Numerical simulations of gas–liquid mass transfer in bubble columns with a cfd–pbm coupled model', *Chemical engineering science* **62**(24), 7107–7118.

Wang, X., Feng, X., Yang, C. and Mao, Z.-S. (2014), 'Energy dissipation rates of newtonian and non-newtonian fluids in a stirred vessel', *Chemical Engineering & Technology* **37**(9), 1575–1582.

Welty, J. R., Wicks, C. E., Rorrer, G. and Wilson, R. E. (2009), *Fundamentals of momentum, heat, and mass transfer*, John Wiley & Sons.

Westerheide, D. E. and Westwater, J. (1961), 'Isothermal growth of hydrogen bubbles during electrolysis', *AIChE Journal* **7**(3), 357–362.

Winn, E. B. (1950), 'The temperature dependence of the self-diffusion coefficients of argon, neon, nitrogen, oxygen, carbon dioxide, and methane', *Physical review* **80**(6), 1024.

Winters, W. S., Evans, G. H., Rice, S. F. and Greif, R. (2012), 'An experimental and theoretical study of heat and mass transfer during the venting of gas from pressure vessels', *International Journal of Heat and Mass Transfer* **55**(1-3), 8–18.

Winterton, R. (1977), 'Nucleation of boiling and cavitation', *Journal of Physics D: Applied Physics* **10**(15), 2041.

Wu, H., Patterson, G. and Van Doorn, M. (1989), 'Distribution of turbulence energy dissipation rates in a rushton turbine stirred mixer', *Experiments in Fluids* **8**(3-4), 153–160.

Yang, S. and Kim, R. (1988), 'A mathematical model of the pool boiling nucleation site density in terms of the surface characteristics', *International journal of heat and mass transfer* **31**(6), 1127–1135.

Zaba, J., Doherty, W. T. and Lyons, W. (1988), *Practical Petroleum Engineer's Handbook*, 5th edn, Gulf Publishing Company, Houston, TX.

Zheng, Q., Klemas, V. and Hsu, Y.-H. (1983), 'Laboratory measurement of water surface bubble life time', *Journal of Geophysical Research: Oceans* **88**(C1), 701–706.

Zhou, J., Vacca, A. and Casoli, P. (2014), 'A novel approach for predicting the operation of external gear pumps under cavitating conditions', *Simulation Modelling Practice and Theory* **45**, 35–49.

Zlochower, I. A. and Green, G. M. (2009), 'The limiting oxygen concentration and flammability limits of gases and gas mixtures', *Journal of loss prevention in the process industries* **22**(4), 499–505.

APPENDICES

APPENDIX A

ABSORPTION-DESORPTION STANDARD OPERATING PROCEDURE

Table A.1: Operators

Alden Daniel
Michael Miranda

Table A.2: Emergency Contacts

Alden Daniel	(XXX) XXX-XXXX
Michael Miranda	(XXX) XXX-XXXX
Clint Aichele	(XXX) XXX-XXXX
Rob Whiteley	(XXX) XXX-XXXX

Table A.3: Standard Operating Procedure Version

Revision no.	12
Revision date	1-25-2018

A.1 Introductory Information

A.1.1 Overview

The objective of this experiment is to measure rates of mass transfer occurring during absorption and desorption. The experiment itself is segmented into four different operations: initial equilibrium, absorption, secondary equilibrium and desorption. The pressure vessel is initially filled with some amount of sample liquid and pressurized up the desired initial saturation pressure. Once at the desired pressure, the system is allowed to come to equilibrium while the gas phase dissolves into the liquid. The absorption step is initiated by pressurizing the overhead gas phase using the pump and the mixing is turned on. After absorption is complete, the pump is then used to depressurize the overhead gas phase and the mixing is turned on to return the experiment to the initial saturation pressure. The second pump cylinder is then used to further depressurize the system and the desorption portion of the experiment is initiated by turning on the mixer again.

The experiment is designed to handle operating conditions up to 150 °C and 6,000 psia (Autoclave MagneDrive mixer is the limiting factor). The dual-cylinder Teledyne Isco pump, HIP tubing, HIP valves, and HIP pressure vessel are all rated to 10,000 psia. The entire setup is to be operated remotely from the lab room, avoiding any risk of entering the blast cell while the contents are under pressure.

Two different Honeywell pressure transducers are used as PT-1. One is rated to 2,000 psi while the second is rated to 10,000 psi. The 2,000 psi rated pressure transducer offers better resolution at lower pressure and should be used for experiment below 2,000 psi. If experiments are to be run above 2,000 psi, the 10,000 psi rated pressure transducer should be used.

A.1.2 Emergency Shutdown

This procedure may be interrupted at any time.

In the event of fire, power failure, hazardous weather or other emergency:

- Stop conducting the experiment.
- TURN OFF the equipment power strip PS.
- CLOSE all gas cylinder regulators: R-1, R-2, R-3, R-4 and R-5.
- CLOSE V-4.

A.1.3 Emergency Medical Response

All operators are required to read SDSs for all chemicals present in the lab. If an operator is exposed to a chemical in a manner that requires immediate attention, it is his/her responsibility to know what to do. There is an eye wash station and overhead shower located in the adjacent lab: room 106D. The shower located outside the lab is non-functional and should not be used. Call 911 in case of an emergency.

A.1.4 Hazardous Weather Protocol (Shelter in Place)

In case of server weather warning (audible siren or otherwise), occupants must take refuge in the HRL 106 shower room (attached to the hallway leading into the lab) until the threat has passed. Ensure any designated operator is signed up for OSUs Cowboy Alert system.

A.1.5 Personal Protective Equipment

All operators, visitors or lab members inside the HRL must:

- Wear close-toed shoes and pants.

Operators must:

- Wear a flame resistant lab coat when handling flammable liquids or could be potentially exposed to flammable gases.
- Wear safety goggles while entering the blast cell and handling sample fluids.
- Wear gloves while handling sample fluids.
- Operator must ensure that the gloves are compatible with all fluids being handled.

A.1.6 Stop Work Authority

All operators, visitors, or lab members have the right to enforce Stop Work Authority (SWA). At any point, if an observer/operator feels that there is an unsafe condition, they can notify the operator of this experiment and enforce SWA, requiring a full system shutdown.

A.1.7 Hydrocarbon Sensor Calibration

The hydrocarbon sensors should be calibrated every 3 months while in use. Refer to the hydrocarbon sensor manual for details on calibration procedures. Refer to the hydrocarbon sensor log sheet next to the charging station for the date of the last calibration.

A.1.8 Chemical Disposal

- - Mineral oils (Tech 80 and Tech 500): Mineral oils should be disposed of into the 5 gal flammable waste container designated for mineral oils. Record the amount disposed on the flammable container disposal log.
- Dodecane: Light hydrocarbons should be disposed of into the 5 gal flammable water container designated for light hydrocarbons. Record the amount disposed on the flammable container disposal log.
- Crude oil: Crude oils should be disposed of into the 5 gal flammable waste container designated for crude oils. Record the amount disposed on the flammable container disposal log.

A.1.9 Chemical Cleanup

- Mineral oils (Tech 80 and Tech 500): Mineral oils should be cleaned with xylene in sparing amounts. Make sure the cleaning location is well ventilated prior to starting.
- - Dodecane: Dodecane should be cleaned with xylene in sparing amounts. Make sure the cleaning location is well ventilated prior to starting.
- Crude oil: Crude oils should be cleaned with xylene in sparing amounts. Make sure the cleaning location is well ventilated prior to starting. If the xylene is ineffective at removing residue, consult with the original supplier of the crude oil for further cleaning information.

A.1.10 Leak Testing

Leak testing is often a very ad hoc procedure, hence only guidelines and not specific steps are given for this procedure.

Operators are allowed into the blast cell for leak testing while the system is under pressure, however specific criteria must be met:

- Ensure the system is depressurized and purged out if methane was being used prior starting a leak test. Refer to steps 3.5, 3.7-3.9 for guidance on inert gas purging.
- Leak test should only use air as the gas phase at pressures up to, but not exceeding, 500 psig.
- Sound is a critical component of leak tests, hence tests can be done without the blast cell blower on. Since ventilation is assumed to be poor inside the blast cell without the blower fan on, it is critical to use air and not nitrogen as the leak detection gas due to the potential of nitrogen asphyxiation in confined areas.

– Due to the pressure drop associated with gas dissolution into liquid, it is recommended that leak test be performed without any liquids in the pressure vessel.

Often the operator will have a specific area of interest that is thought to be leaking. To simplify leak testing, the area of interest should be sectioned off as best as possible by closing surrounding valves. Monitor the pressure of the associate pressurized region for a steady decline over time. Use the leak detection fluid on fittings/connections of interest and look for bubble generation to confirm a leak. DO NOT attempt to fix a leak while the system is under pressure. Depressurize the entire system, correct the fitting/connection, and pressurize the area of interest again and re-check for leaks.

In order to verify the pressure integrity of the entire system, the whole system should be pressurized up to 500 psig with air and left for 24 hours. To improve temperature stability, the vessel circulator should be left on with a circulating liquid setpoint (P1) of 25 °C. The pressure and temperature should then be converted to a molar value for ultimate confirmation of constant mass within the system.

A.1.11 Hazardous Entry

If the operator MUST enter the blast cell while under pressure and/or operating with hydrocarbons, this hazardous entry procedure can be followed but extreme caution must be employed.

The following criteria must be met prior to a hazardous entry scenario:

– Ensure all sample gas cylinders are closed (R-1, R-4, R-5, and V-4).

– Allow the blower to operate continuously for at least 60 minutes.

– Ensure the operator has on goggles as well as a flame-retardant lab coat.

– Ensure the hydrocarbon sensor unit attached to the operator is operational.

Upon entering, the issue within the blast cell should be addressed quickly and safely. DO NOT attempt to alter any connections while the system is under pressure. If in doubt about the ability to solve the issue, call OSU's EHS Lab and Safety division (405 744 7241) and the contacts listed on the front of the SOP

A.1.12 Unmanned Operation with Hydrocarbon Systems

Due to often long times required for equilibrium to be reached, unmanned pressurized operation is permitted throughout the experiment. Always ensure V-4 is closed prior to leaving the lab.

A.1.13 Incident/Near-Miss Reporting

Report and record:

– All accidents, no matter how small.

- All near misses that might have resulted in injury or property damage.
- All unsafe or hazardous conditions.

In addition to recording here, any incident/near-miss should be reported to the laboratory PI. Refer to OSUs EHS website for more reporting guidelines.

A.1.14 Prior Incidents/Near-Misses

Near-miss - May 9th, 2016

- Description: Three occupants, including the experimental operator, were at the HRL conducting a meeting when one person noticed ominous looking clouds in the sky. A little past 5 pm, tornado warnings were issued via text message to two of the three occupants (including the operator). As soon as the group was alerted to the possibility of a tornado, everyone vacated the premise and drove to their respective houses/safe places. No sirens were heard in the area prior to leaving. At the time, the experimental procedure did not stipulate what to do in the event of an extreme weather occurrence.
- Prevention: New additions to the experimental procedure guide occupants to the designated shelter in place location (hall shower) in the event of an extreme weather occurrence. Any form of severe weather warning (audible siren, text message, etc.) is sufficient to trigger the shelter in place order.

Near-miss - July 21st, 2016

- Description: While the circulator has a working temperature up to 200 °C, the upper temperature limit is limited by the circulating fluid used. In attempt to increase the temperature beyond what was capable with 50-50 ethylene glycol/water, Syltherm XTL (heat transfer fluid made by Dow) was used as the circulating fluid instead. It was soon discovered that Syltherm was itself flammable and meant only for use in closed systems (the current circulator is not closed to the atmosphere). The Syltherm fluid was promptly replace with an ethylene glycol/water mixture again.
- Prevention: When changing the circulating fluid, only use fluids recommended by the circulator user manual.

Near-miss - October 19th, 2016

- Description: The original mixer manufactured by Supercritical Fluid Technologies had been known to wobble to a large degree. After a particularly erratic measurement of power drawn to the mixer was detected during a gas evolution trial, the experiment was ended and mixer inspected. It was discovered that the shaft had broken off from the rest of the mixer. The wobbling appeared to have gotten critically out of control, coming in contact with the bottom of the vessel and breaking off. The vessel, acting as primary containment for the experiment, was not breached and the experiment did not undergo unplanned pressure loss. No individuals were injured or exposed to experiment during this near miss.

– Prevention: A new mixer was purchased from Autoclave with a shorter total shaft length (nullifying the chances of the impeller head coming in contact with the vessels bottom) and stringent runout specifications (less than 0.0005 in/in shaft). For a more detailed summary of the incident, please refer to the near-miss report.

A.2 Operating Procedure

Table A.4: SOP – Inspection and Set-up

Step No.	Step
1.0	**Inspection and Set-up**
1.1	NOTE: Whenever work is being done on the equipment, ALWAYS first make sure the equipment has been depressurized. TURN ON controllers C-1, C-2, C-3 and PC. ENSURE C-1 and C-3 display atmospheric pressure.
1.2	ENSURE gas cylinder GC-1, GC-4 and GC-5 have at least 500 psig of pressure left.
1.3	ENSURE gas cylinder GC-2 has at least 250 psig of pressure left. OPEN gas regulator R-2 to 90 psi.
1.4	ENSURE gas cylinder GC-3 has at least 250 psig of pressure left. OPEN gas regulator R-3 to 90 psi.
1.5	IF methane is being used, ENSURE the hazardous operation safety signage is displayed in accordance with the signage location sheet next to the sign storage.
1.6	ENSURE hydrocarbon sensors are fully charged. ENSURE hydrocarbon sensor calibrations are up to date. MOUNT hydrocarbon sensors on designated location in accordance with the rotation order on the log sheet and RECORD their position.
1.7	ENSURE the pressure rating of the pressure transducer and vessel rupture disc are capable of handling the expect experimental pressures.
1.8	ENSURE all equipment maintenance is up to date by checking the maintenance log.
1.9	IF hydrocarbon sensor alarms are heard at any time throughout the experiment, IMMEDIATELY PERFORM an emergency shutdown.

Table A.5: SOP – Vessel Filling

Step No.	Step
2.0	**Vessel Filling**
2.1	ENSURE the experiment is at atmospheric pressure prior to operation by checking C-3. ENSURE the pump is stopped. ENSURE the operator has on safety glasses prior to entering the blast cell. IF hydrocarbons are being handled, ENSURE the PPE requirements specified on page 3 are fulfilled.
2.2	TURN ON the blast cell blower (labeled switch on wall) to ensure the working atmosphere is well dispersed. ENSURE blower flaps are free floating.
2.3	DISCONNECT the power supply and tachometer cable to the mixer inside the blast cell.
2.4	NOTE: The vessel cover is heavy ($\tilde{3}$0 lbs). Exercise caution while lifting and handling the equipment. INSERT the tony bar into one of the holes on the perimeter of the vessel cover. Using the tony bar as leverage, SCREW open the vessel lid. ENSURE the vessel stand remains in place while unscrewing. REMOVE the lid and mixer M-1 by pulling both up vertically. PLACE mixer and lid onto the designated mixer stand.
2.5	ENSURE the interior of the vessel is clean and ready to receive fluids. MOVE the bulk liquid sample container from its storage to the interior of the blast cell.
2.6	NOTE: DO NOT add more than 1,000 mL of sample liquid into the pressure vessel. ENSURE the operator has on gloves prior to handling sample fluids. TARE a clean beaker on a scale in the blast cell. PIPETTE the desired amount of sample liquid into the beaker. RECORD the mass of the liquid sample.
2.7	POUR the sample liquid into the vessel opening. AVOID splashing on the sides of the vessel.
2.8	ENSURE the vessel lid has anti-seize evenly spread across the threaded portion of the lid. IF NOT, REAPPLY a small amount of anti-seize to the threads.
2.9	ENSURE the O-ring and O-ring seal on the vessel are properly aligned.

Table A.6: SOP – Vessel Filling, continued

Step No.	Step
2.10	GENTLY LOWER the mixer and vessel lid back onto the vessel. ENSURE the mixer is directly vertical and not touching any of the vessel walls. SCREW the vessel lid back on by hand until it is completely sealed. DO NOT OVER TIGHTEN the vessel lid.
2.11	RECONNECT the power supply and tachometer cable to the mixer. MOVE the bulk liquid sample container back to its respective storage.

Table A.7: Pre-Pressurization Preparations

Step No.	Step
3.0	**Pre-Pressurization Preparations**
3.1	SELECT the appropriate temperature setpoint on the circulator. CHECK that there is enough circulating fluid to cover the heating elements inside the circulator. CHECK that the circulator time matches local time. IF NOT, adjust the time on the circulator. START liquid temperature data logging on the circulator. TURN ON the circulator box fan.
3.2	ENSURE both pump pressure transducers are reading atmospheric pressure (0 psig). IF NOT, ZERO each pressure transducer on the pump using C-1
3.3	ENSURE the vessel has come to thermal equilibrium before proceeding to the next step (this step could typically take 3 hours or more).
3.4	NOTE: Refer to the gas cylinder regulator operation guide for specifics on the proper technique for regulator operation. OPEN all required LabVIEW VI windows needed for the trial, but do not start them. START the actuator LabVIEW VI. ENSURE all three actuators are open.
3.5	TURN ON the blue light. OPEN V-4 is open.
3.6	IF hydrocarbons are being used for the gas phase, continue to step 3.7. IF NOT, continue to step 4.0.
3.7	CLOSE V-2. OPEN R-4 to a pressure of 200 psig.

Table A.8: Pre-Pressurization Preparations, continued

Step No.	Step
3.8	Once PT-1 reads 214 psia, CLOSE R-4. WAIT for 5 minutes.
3.9	ENSURE lab door to the outside is closed. OPEN V-2. ALLOW the system to come back to atmospheric pressure.
3.10	CLOSE V-2. OPEN R-5 to a pressure of 200 psig.
3.11	Once PT-1 reads 214 psia, CLOSE R-5. WAIT for 5 minutes.
3.12	ENSURE lab door to the outside is closed. OPEN V-2. ALLOW the system to come back to atmospheric pressure.
3.13	REPEAT steps 3.10-3.12 once again to ensure the vessel starts with a pure methane gas overhead.

Table A.9: SOP – Initial Equilibrium

Step No.	Step
4.0	**Initial Equilibrium**
4.1	ENSURE pump A is filled and has a flow rate = 0.0 mL/min. ENSURE pump B is totally discharged (minus the 1-2 mL water seal) and has a refill rate = 0.0 mL/min.
4.2	START temperature measurements using the gas temperature LabVIEW VI. START pressure measurements using the low frequency LabVIEW VI.
4.3	NOTE: From this step forward, no operators should enter the blast cell until the experiment has been completely shut down. All controls of the pump, actuators and measurements should be done using the PC. If an operator must enter the blast cell while under pressure and/or operating with hydrocarbon gases, refer to the hazardous entry procedure. OPEN the regulator R-1 or R-5 (if methane is being used) to the desired pressure.
4.4	CLOSE R-1 or R-5 (if methane is being used). CLOSE V-4.
4.5	RECORD the vessel pressure and temperature. RECORD each pump cylinder pressure and temperature.

Table A.10: SOP – Initial Equilibrium, continued

Step No.	Step
4.6	TURN ON the mixer to sub-entrainment mixing using C-2.
4.7	ALLOW the vessel to sit until the pressure slope averaging function within the pressure measurement LabVIEW VI reaches a value of 0.
4.8	RECORD the vessel pressure and temperature. RECORD each pump cylinder pressure and temperature.
4.9	TURN OFF the mixer using C-2. ALLOW the vessel to sit until the pressure slope averaging function within the pressure measurement LabVIEW VI reaches a value of 0.
4.10	SET pump A flow rate = 20 mL/min dispensing 100 mL. ENSURE the pump cylinder is moving.
4.11	WAIT until pump cylinder completely dispensed until proceeding with the next step.
4.12	RECORD the vessel pressure and temperature. RECORD each pump cylinder pressure and temperature.

Table A.11: SOP – Absorption

Step No.	Step
5.0	**Absorption**
5.1	ENSURE the correct mixing speed is selected on C-2.
5.2	STOP low frequency pressure measurements using LabVIEW VI. START high frequency pressure measurements using LabVIEW VI.
5.3	WAIT 75 seconds.
5.4	TURN ON the mixer using C-2.
5.5	ALLOW the vessel to sit until the pressure slope averaging function within the pressure measurement LabVIEW VI reaches a value of 0.
5.6	RECORD the vessel pressure and temperature. RECORD each pump cylinder pressure and temperature.
5.7	STOP high frequency pressure measurements using LabVIEW VI. START low frequency pressure measurements using LabVIEW VI.
5.8	TURN OFF the mixer using C-2. WAIT 15 minutes.

Table A.12: SOP – Second Equilibrium

Step No.	Step
6.0	**Second Equilibrium**
6.1	SET pump A refill rate = 20 mL/min.
6.2	ALLOW pump A to stop. SET pump A flow rate = 0.0 mL/min. SET pump B refill rate = 0.0 mL/min.
6.3	RECORD the vessel pressure and temperature. RECORD each pump cylinder pressure and temperature.
6.4	TURN ON the mixer to sub-entrainment mixing using C-2.
6.5	ALLOW the vessel to sit until the pressure slope averaging function within the pressure measurement LabVIEW VI reaches a value of 0.
6.6	RECORD the vessel pressure and temperature. RECORD each pump cylinder pressure and temperature.
6.7	TURN OFF the mixer using C-2. ALLOW the vessel to sit until the pressure slope averaging function within the pressure measurement LabVIEW VI reaches a value of 0.
6.8	SET pump B refill rate = 20 mL/min. ENSURE the pump cylinder is moving.
6.9	WAIT until pump cylinder completely refilled until proceeding with the next step.
6.10	RECORD the vessel pressure and temperature. RECORD each pump cylinder pressure and temperature.

Table A.13: SOP – Desorption

Step No.	Step
7.0	**Desorption**
7.1	ENSURE the correct mixing speed is selected on C-2.
7.2	STOP low frequency pressure measurements using LabVIEW VI. START high frequency pressure measurements using LabVIEW VI.
7.3	WAIT 75 seconds.
7.4	TURN ON the mixer using C-2.
7.5	ALLOW the vessel to sit until the pressure slope averaging function within the pressure measurement LabVIEW VI reaches a value of 0.
7.6	RECORD the vessel pressure and temperature. RECORD each pump cylinder pressure and temperature.
7.7	STOP high frequency pressure measurements using LabVIEW VI. START low frequency pressure measurements using LabVIEW VI.
7.8	TURN OFF the mixer using C-2.

Table A.14: SOP – Shut Down and Clean Up

Step No.	Step
8.0	**Shut Down and Clean Up**
8.1	ENSURE lab door to the outside is closed. OPEN valves V-1, V-2, and V-3. DISCHARGE each pump completely (dispense 100 mL per pump). ALLOW the system to come back to atmospheric pressure.
8.2	TURN ON the mixer to 500 RPM. OBSERVE the pressure spike and return to atmospheric pressure. ALLOW the liquid to mix for an additional 25 minutes. TURN OFF the mixer.
8.3	IF hydrocarbons were being used for the gas phase, continue to step 8.4. IF NOT, continue to step 8.7.
8.4	CLOSE V-2. OPEN V-4. OPEN R-4 to a pressure of 200 psig.
8.5	Once PT-1 reads 214 psia, CLOSE R-4. WAIT for 5 minutes.
8.6	OPEN V-2. ALLOW the system to come back to atmospheric pressure. CLOSE V-4. TURN OFF the blue light.
8.7	ENSURE PT-1 reads atmospheric pressures prior to entering the blast cell. ENSURE R-1 and R-5 are closed. ENSURE the operator has on safety glasses prior to entering the blast cell. IF hydrocarbons are being handled, ENSURE the PPE requirements specified are fulfilled.
8.8	STOP liquid temperature data logging on the circulator. TURN OFF the circulator. TURN OFF the circulator box fan. IF the vessel was heated to above room temperature, WAIT until the vessel cools down.
8.9	DISCONNECT the power supply and tachometer cable to the mixer.
8.10	ENSURE the operator has on gloves prior to handling sample fluids.

Table A.15: SOP – Shut Down and Clean Up, continued

Step No.	Step
8.11	INSERT the tony bar into one of the holes on the perimeter of the vessel cover. Using the tony bar as leverage, SCREW open the vessel lid. ENSURE the vessel stand remains in place while unscrewing. REMOVE the lid and mixer M-1 by pulling both up vertically. PLACE mixer and lid onto the designated mixer stand.
8.12	REMOVE the sample fluid using the pipette and bulb. DISPOSE the sample fluid in accordance with the disposal requirements.
8.13	CLEAN the interior of the vessel using the appropriate cleaning procedure.
8.14	ENSURE the vessel lid has an appropriate amount of anti-seize evenly spread across the threaded portion of the lid. IF NOT, REAPPLY as small amount of anti-seize to the threads.
8.15	ENSURE the O-ring and O-ring seal on the vessel are properly aligned.
8.16	GENTLY LOWER the mixer and vessel lid back onto the vessel. ENSURE the mixer is directly vertical and not touching any of the vessel walls. SCREW the vessel lid back on by hand until it is completely sealed. DO NOT OVER TIGHTEN the vessel lid.
8.17	RECONNECT the power supply to the mixer.
8.18	TURN OFF the blast cell blower.
8.19	RETURN hydrocarbon sensors to charging station. IF methane was being used, TAKE DOWN the hazardous operation safety signage.

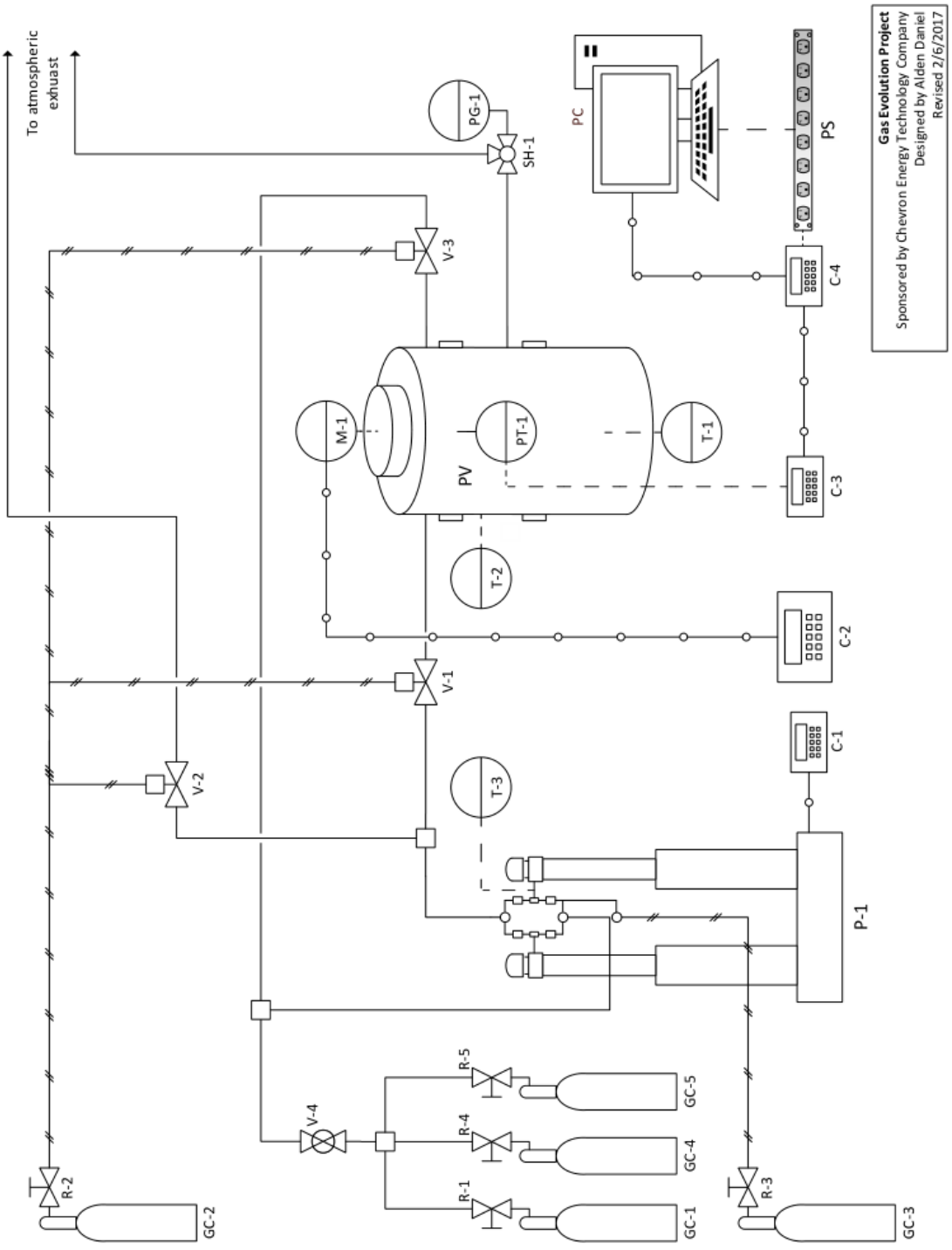

Figure A.1: SOP P&ID

ID	DESCRIPTION	MGF	MODEL
C-1	Pump controller	ISCO	Key Smart
C-2	Mixer controller	Autoclave	URC-II-120
C-3	Pressure indicator	Honeywell	SC500
C-4	NI DAQ	NI	cDAQ-9174
GC-1	Compressed air (UHP) gas cylinder		
GC-2	Compressed air gas cylinder		
GC-3	Compressed air gas cylinder		
GC-4	Compressed nitrogen gas cylinder		
GC-5	Compressed methane gas cylinder		
M-1	MagneDrive mixer	Autoclave	IMAG075
P-1	Continuous flow syringe pump	Teledyne	A100DX
PC	Personal computer	Dell	
PG-1	Pressure gauge		
PS	Power strip w/ battery supply		
PT-1	Pressure transducer	Honeywell	TJE

ID	DESCRIPTION	MGF	MODEL
PV	Pressure vessel	HIP	Series R
R-1	Gas cylinder regulator	VWR	55850-496
R-2	Gas cylinder regulator	VWR	55850-704
R-3	Gas cylinder regulator	VWR	55850-704
R-4	Gas cylinder regulator	VWR	55850-476
R-5	Gas cylinder regulator	VWR	55850-476
SH-1	Tee type safety head w/ rupture disc	HIP	15-63AF2
T-1	Vessel RTD - liquid	Omega	PR-11-2-100-1/8
T-2	Vessel thermocouple - gas	Omega	TJ144-CASS
T-3	Pump thermocouple - gas	Omega	TJ144-CASS
V-1	1/4 turn two-way ball valve	HIP	15-71AF2-TSR8
V-2	1/4 turn two-way ball valve	HIP	15-71AF2-TSR8
V-3	1/4 turn two-way ball valve	HIP	15-71AF2-TSR8
V-4	Ball valve	HIP	15-16AF2

CONNECTION LEGEND

ID	DESCRIPTION	MGF	MODEL
	1/8" OD 316 SS seamless tubing	HIP	15-9A2
	Electric connection	*various*	
	Data connection	*various*	
	Pneumatic connection		

Figure A.2: SOP P&ID Legend

VITA

ALDEN B. DANIEL

Candidate for the Degree of

Doctor of Philosophy

Dissertation: GAS EVOLUTION AND GAS-LIQUID SEPARATOR MODELING

Major Field: Chemical Engineering

Biographical:

Education:
Completed the requirements for the Doctor of Philosophy in Chemical Engineering at Oklahoma State University, Stillwater, Oklahoma in December, 2018.

Completed the requirements for the Bachelor of Science in Chemical Engineering at Florida State University, Tallahassee, Florida in 2013.

Experience:
Graduate Research Assistant, Oklahoma State University, Stillwater, OK: June 2014 – July 2018

Fractionation and Separation Intern, ExxonMobil Upstream Research Company, Spring, TX: May 2017 – August 2017

Laboratory/Teaching Assistant, Florida State University, Tallahassee, FL: August 2013 – December 2013

Accepted a full time position with ExxonMobil Upstream Research Company in Spring, TX beginning August, 2018.